Environmental Dependence of Hα Disks in Nearby Star-Forming Galaxies

Environmental Dependence of Hα Disks in Nearby Star-forming Galaxies

By
Jacqueline N. Wightman,
B.C.D., B.Sc., M.T.

A Thesis Submitted to the School of Graduate Studies in the Partial Fulfillment of the Requirements for the Degree Master of Science

McMaster University

McMaster University
Master of Science (2020)
Hamilton, Ontario (Department of Physics and Astronomy)

TITLE: Environmental Dependence of Hα Disks in Nearby Star-forming Galaxies
AUTHOR: Jacqueline N. Wightman (McMaster University)
SUPERVISOR: Dr. Laura Parker
NUMBER OF PAGES: 107

Abstract

We use Integral Field Unit (IFU) data for a subset of galaxies in the MaNGA (Mapping Nearby Galaxies at Apache Point Observatory) sample to investigate the environmental dependence of Hα properties for nearby star-forming galaxies. We characterize the non-AGN Hα emission for galaxies living in different host environments with radial gradient measurements, half-light radii, as well as measures of concentration and asymmetry. We find that global specific star formation rates (sSFR) are lower in nearby star-forming galaxies in groups and clusters compared to those in the field, and the lowest in high density environments such as group or cluster centres. From the resolved data we find that the overall reduction in Hα emission in star-forming galaxies in denser environments occurs across the face of these galaxies, suggesting starvation as a primary quenching mechanism. We further find that Hα disks are truncated in group galaxies that live nearer the center of the halo compared to those in the outer halo or field, which may be due to ram pressure stripping in these dense environments.

Acknowledgements

Embarking on this MSc at McMaster has been one of the best decisions I have ever made, in no small part because of the people I met and had the pleasure of working with. The Physics and Astronomy department became my home over the past two years, and I am so grateful for the support and encouragement of everyone in the department throughout this entire program.

In particular, I would like to thank my thesis supervisor, Laura Parker. Thank you for guiding me through this project with constant enthusiasm and for all of the wisdom you imparted on me along the way. Thank you also for your empathy during all of the bumps and hurdles, notably the world pandemic that started mid-way through the program. I am so glad that I had you as a mentor to turn to.

James Wadsley and Alison Sills, thank you for being on my committee and for your support and input on this thesis. Thank you as well to all of the members of our research group for their support and advice, and to my office mates. Whenever I got stuck, I could always count on Ryan or Ian to point me in the right direction. I would also like to thank Rachel Brown for providing me with some valuable code to get me started.

Thank you to all of my new friends that made the last two years a joy. Anita, Hector, Dennis, and Sachin, I am glad to have done this program with you all; we had a lot of late nights and a lot of good times together. To the boys' house and my climbing buddies, thanks for making my breaks from work more fun. To all of the current first year astronomy Masters students, it's been great getting to know and work with you. Claude, thank you for your support and friendship.

To all of my old friends and family, thank you for believing in me and supporting me through all of my (many, many) years of post-secondary. Marie, thank you for always being there for me. Laura, Matt and Mitch, I appreciate you and our long-distance friendship, thank you for cheering

me on, always. Thank you to my grandparents for encouraging me and nourishing me.

Thank you especially to my parents, Mom, Paul, and Juliette, and to my sisters, Melanie and Rosalind, for your constant encouragement and confidence in me - here is my 'physics novella.' To my dad, who would have enjoyed reading this thesis, thank you for inspiring me to do science.

In loving memory of my dad, Glen N. Wightman

Contents

List of Figures

Chapter 1

Introduction and Motivation

The study of galaxies accelerated in the early 1990s with the launch of the Hubble Space Telescope (see 1.1); however, it is a centuries-old pursuit. The first person to observe galaxies other than our own Milky Way was a Persian astronomer, Abd al-Rahman al-Sufi, in year 964. He recorded his observations of the Andromeda Galaxy and the Large Magellanic Cloud in his Book of Fixed Stars (Hafez et al., 2011). In the 18th century, French astronomer Charles Messier catalogued galaxies and clusters while searching for comets. Since they looked cloud-like, he called them nebulae (Gingerich, 1953; Messier, 1774).

It was not for 200 years that astronomers were able to identify what the "spiral nebulae" were. With the advent of bigger and better telescopes, astronomers were able to resolve these nebulae - seeing that they were groupings of many stars. In 1925, Edwin Hubble determined the distance to the Andromeda galaxy using the known period of Cepheid variable stars (Leavitt, 1908), confirming that it lay far outside the limits of our own galaxy. His work showed conclusively that other galaxies exist beyond our own (Hubble, 1925).

We know today that beyond the stars in our own Milky Way galaxy lie billions and billions of other galaxies of various shapes, sizes, and colours. The observable Universe is thought to contain roughly 2 trillion galaxies (Conselice et al., 2016). What were once thought to be nebulous clouds, we know now are massive gravitationally-bound systems of gas, dust, stars

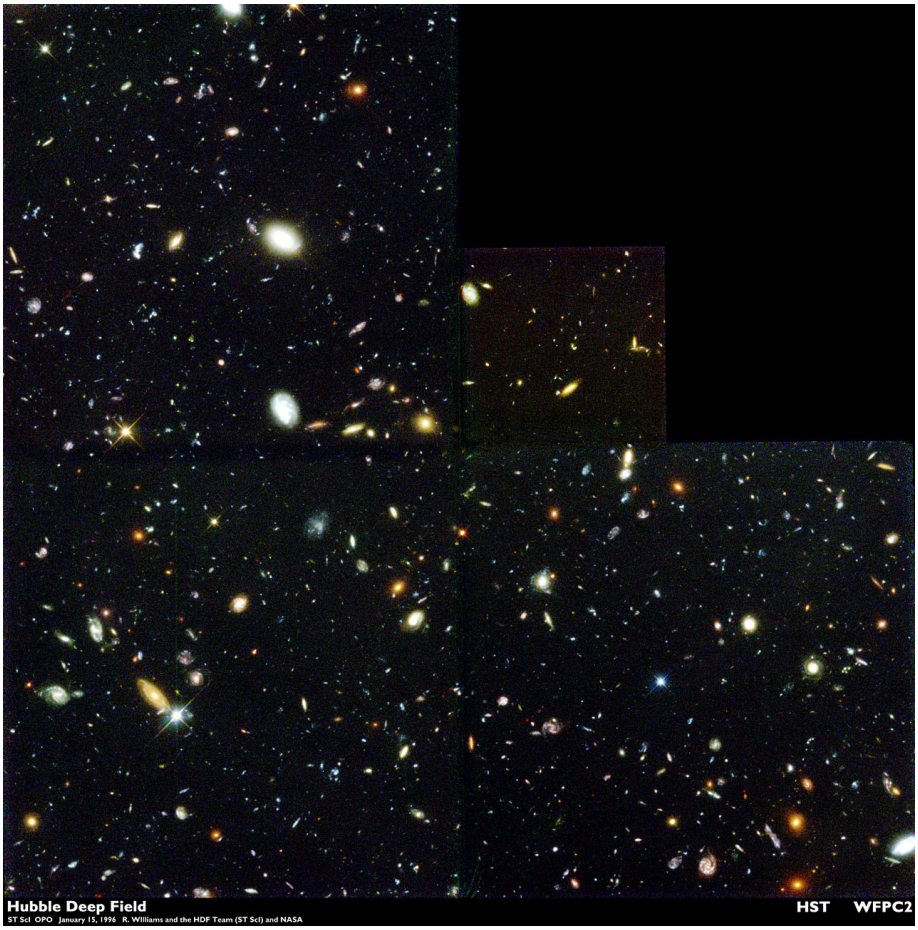

FIGURE 1.1: The Hubble Deep Field Williams et al. (1996): This spec of sky is about the width of a dime 75 feet away and contains at least 1500 galaxies.

and dark matter. Galaxies range in size from dwarfs, which contain a few hundred million (10^8) stars, to giants, which contain a hundred trillion (10^{14}) stars (Uson et al., 1990). There are many dwarf galaxies orbiting the Milky Way on the order of thousands of light years away, but the nearest major galaxy to us is the Andromeda galaxy at 2.5 million light years away (Ribas et al., 2005). There are many candidate redshift[1] $\sim$10 galaxies; one

[1] Cosmological redshift, z, refers to the stretching of the wavelength of light caused by the expansion of the Universe. Redshift, measured from the line of site velocity, is a proxy for distance. z$\sim$10 corresponds to an extremely distant object and the light was emitted when the Universe was <1 billion years old

of the furthest galaxies observed to date has a photometric redshift of z = 10.7+0.6 and was discovered as part of the Cluster Lensing and Supernova survey with Hubble (CLASH) (Coe et al., 2012).

By studying galaxies at different distances we can learn about the evolution of the Universe over time.[2] In recent decades, our understanding of structure in the Universe has grown enormously, due to better telescopes and dedicated efforts to survey millions of galaxies in the night sky. Galaxies are the building blocks of the largest structures in the Universe. We now understand that objects in the Universe grow over cosmic time to make ever larger structures. For example, galaxies collect gravitationally into groups and clusters, which can contain hundreds or thousands of individual galaxies. Despite a growing understanding of structure formation on large scales, many questions about the details of galaxy evolution remain. How did galaxies first form? How did we end up with the large variety of observed properties we see today? What causes star formation to cease in galaxies?

1.1 Galaxy Properties

To classify galaxies, astronomers use observed properties that can be measured directly or determined from other parameters. Some important galaxies properties and how they are obtained are outlined in this section.

1.1.1 Morphology

There are a number of morphological classification systems that astronomers use to group galaxies based on visual appearance. One such system is the Hubble sequence, which was originally created by Edwin

[2]The more distant the object is that we observe, the further back in time we are observing due to the time elapsed between when the light was emitted from the object and when it arrives on Earth.

Hubble (1926) and continues to be used today. The original system consisted of three main morphological types of galaxies, each of which can be subdivided into further categories: spiral, elliptical, and irregular galaxies (see Figure 1.2). Hubble described ellipticals as 'early-type' galaxies, and spirals as 'late-type' galaxies - terms that are also still used today - but noted that the nomenclature "refers to position in the sequence, and temporal connotations are made at one's peril. The entire classification is purely empirical and without prejudice to theories of evolution" (Hubble, 1927). Later, Hubble introduced another category, lenticular galaxies, which are classified between spirals and ellipticals on the Hubble sequence (van den Bergh, 1979). Figure 1.3 shows some examples of the different morphological types, drawn from the sample used in this thesis.

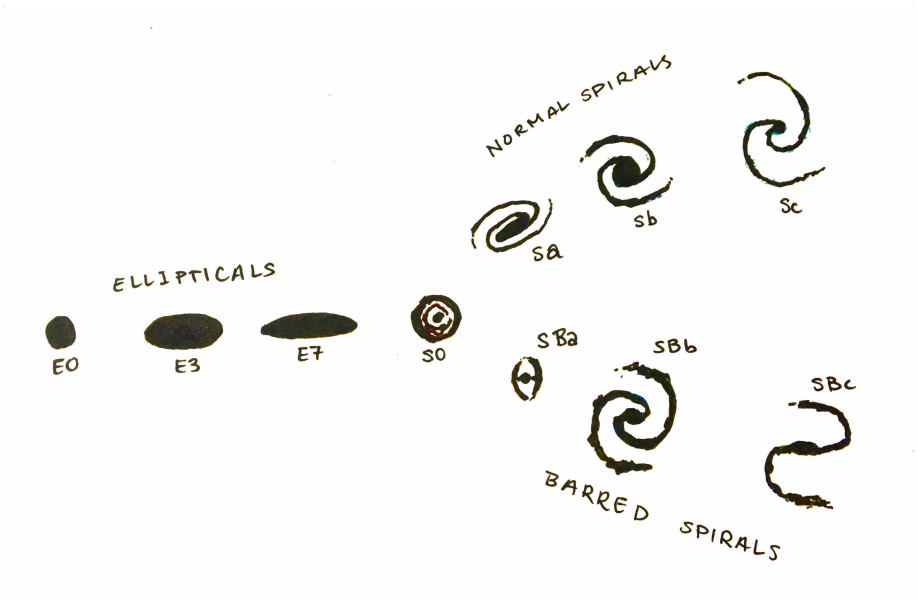

FIGURE 1.2: The Hubble Tuning Fork, adapted from Hubble (1936). Hubble described his classification scheme for galaxies as a tuning fork, with 'elliptical nebulae' forming the stem, and normal and barred spirals lying along the two arms. He noted that irregular galaxies, due to their lack of rotational symmetry, do not have a place on the tuning fork.

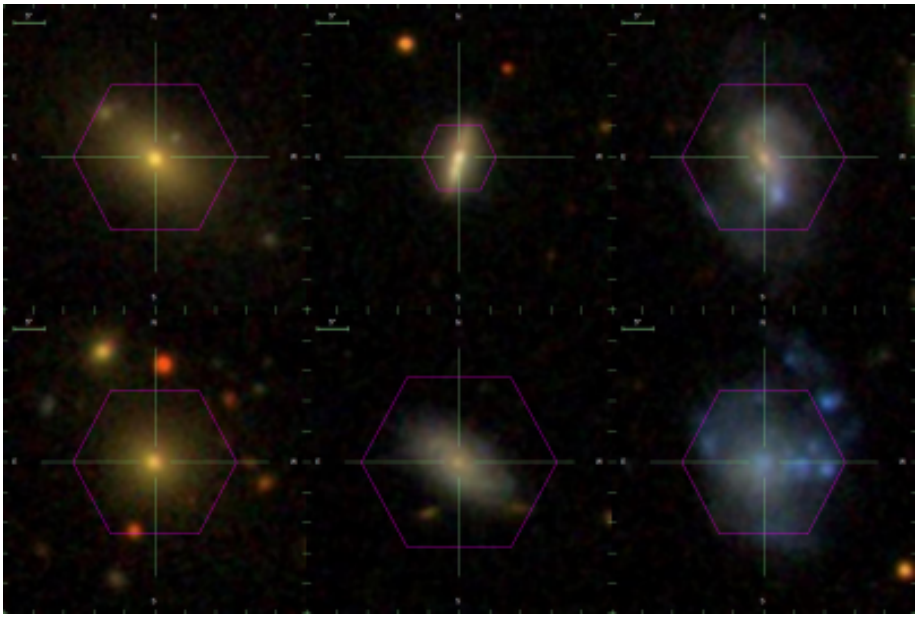

FIGURE 1.3: Galaxies from my sample illustrate the different morphological types based on the Hubble Sequence. In the top row, from left to right: elliptical, lenticular, and barred spiral. In the bottom row, from left to right: elliptical, spiral, and irregular. Images are obtained from the Marvin web interface (Cherinka et al., 2019).

Spiral Galaxies

Spiral galaxies are disk-like and tend to be bluer, with younger stellar populations and higher star formation rates (Schawinski et al., 2014; Blanton and Moustakas, 2009). They have the characteristic spiral arms when seen face-on; when seen edge-on, they tend to bulge in the middle and taper at the edges (de Vaucouleurs, 1959). Most spirals consist of two main features: the spiral disk and the bulge. The flat, rotating disk, with two or more spiral arms, is filled with stars, dust, and gas, and is where active star formation tends to occur. The bulge is a central, reddish, smooth, and spheroidal component (Blanton and Moustakas, 2009), and tends to be comprised of an older population of stars than that of the disk (Moorthy and Holtzman, 2006). Quantitative classification measures of spirals focus on separating the disk from the bulge. For example, in fitting packages such as that of Simard (1998), the luminosity profile of the bulge and disk

components are fit separately. These quantitative morphological measures can then be used to describe morphologies through the bulge to total luminosity ratio (B/T), a continuous parameter. For example, elliptical galaxies have almost all bulge (B/T$\sim$1), whereas late spirals have almost all disk (B/T$\sim$0).

Barred-spiral galaxies are a subset of spiral galaxies that contain a bar structure in their central region. About half of all spiral galaxies have a bar (Masters et al., 2011; Menéndez-Delmestre et al., 2007). The Milky Way is an example of a barred-spiral galaxy. Peters (1975) first created a model of the Milky Way that suggested the existence of a bar; it involved gas flowing along streamlines that could be caused by a bar-like density wave in the inner region of the galaxy. Peters' model was able to reproduce key observed features of our galaxy, such as the 3 kpc arm, and other high-velocity emission observed in the 21-cm line. More recently, the detection of high-velocity bar stars from the Apache Point Observatory Galactic Evolution Experiment (APOGEE) is observational evidence that our Milky Way has a central bar structure (Nidever et al., 2012).

Elliptical Galaxies

Elliptical galaxies are symmetric, smooth, and tend to be redder in colour than spirals (Schawinski et al., 2014). They have low star formation rates, and their stellar populations tends to be older (Blanton and Moustakas, 2009). In general, there are two types of elliptical galaxies: those with and without nuclear cores. Core galaxies, relative to those without cores, are more slowly rotating, more luminous, and less elongated (Kormendy et al., 2009).

Lenticular Galaxies

Lenticular galaxies, like spirals, are disk galaxies; however, they lack spiral structure. Like ellipticals, they are smooth, concentrated, and have low star formation rates per unit of mass (Blanton and Moustakas, 2009). Hubble

(1936) characterized lenticular galaxies as "armless spirals," and placed them between elliptical and spirals on the Hubble Sequence (Figure 1.2).

Irregular Galaxies

Irregular galaxies fit into none of the previous categories – Hubble (1926) defines irregulars as lacking "both dominating nuclei and rotational symmetry." They tend to be smaller, less massive, with high star formation rates (Glazebrook et al., 1999). The example of an irregular galaxy in Figure 1.3 is very blue, which is characteristic of active star formation (Blanton and Moustakas, 2009). Irregular galaxies are thought to be either newly forming galaxies, or the result of galaxy interactions and mergers (Gallagher and Hunter, 1984). While Hubble (1936) original estimated that the irregular population of galaxies is 3%, Gallagher and Hunter (1984) estimates the population of irregulars to be about a third to a half of all galaxies.

1.1.2 Colour

Colour is an observed property of a galaxy that is easily measured and gives insight into its stellar populations. Astronomers have long been classifying stars based on their optical colour and spectrum (Secchi, 1866). It is well known that bright, short-lived, hot stars tend to be bluer, while older, cooler stars are redder (Carroll and Ostlie, 2007). Since the light from galaxies comes from stars, a galaxy's overall colour can tell us about its underlying stellar population, albeit, both redshift (Hubble, 1929) and interstellar dust cause reddening of light (Kim and Lee, 2007; Xiao et al., 2012).

The colour of a galaxy is determined by measuring the difference in flux between two broad-band filters. For example, using the SDSS photometric system, *u', g', r', i', and z'*, with bands centred at 359nm, 481nm, 623nm, 7640nm, 9060nm (Fukugita et al., 1996): a galaxy's flux through the *u'* and *r'* filters are measured, and the difference in magnitude, *u'-r'*, is a measure of its colour. Since lower magnitudes indicate a higher flux, a low *u'-r'* colour value indicates that the galaxy is more blue, while a higher *u'-r'* colour is more red.

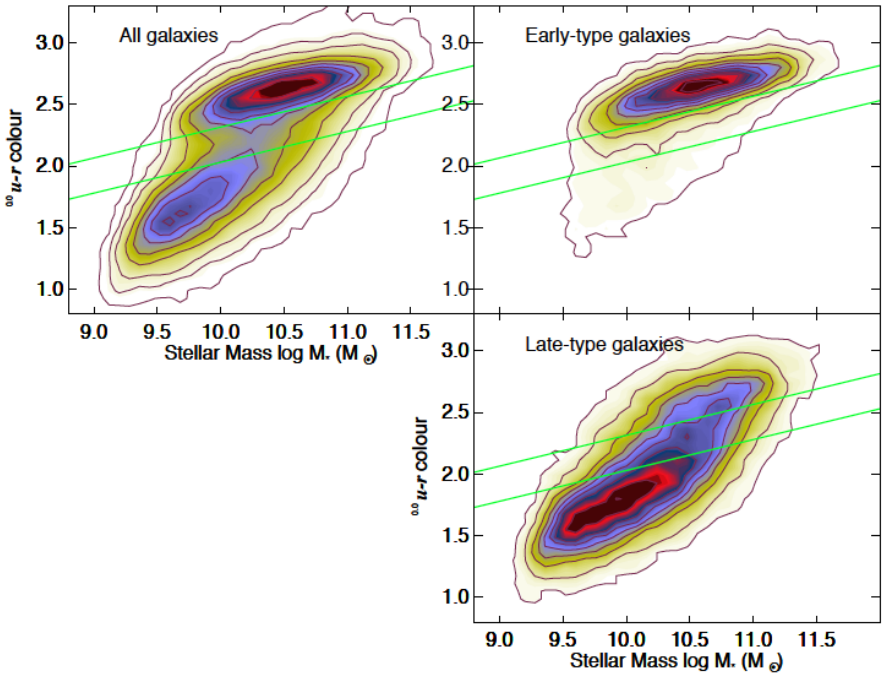

FIGURE 1.4: The u-r colour-mass diagram for a sample of galaxies from the Sloan Digital Sky Survey (SDSS), illustrating the bimodal distribution (Schawinski et al., 2014, Figure 2). Blue galaxies live in the bottom region of the plot (colloquially called the "blue cloud"), and tend to be early-type (elliptical) galaxies. Red galaxies live in the top region of the plot (the "red sequence"), and tend to be late-type (spiral) galaxies. The green lines indicate the location of the green valley, defined in the all-galaxies (upper-left) diagram.

Observational studies of galaxies have revealed a bi-modal distribution in colour: galaxies can be roughly divided into red and blue populations (Figure 1.4). The blue population tends to be comprised of spiral galaxies, with younger stellar populations, and more active star formation. These galaxies also tend to live in the field (1.2.1) (Blanton and Moustakas, 2009; Belfiore et al., 2018). On the other hand, the red population is comprised of ellipticals, lenticulars, and dust-reddened spirals, with older stellar populations and lower star formation rates (Kennicutt, 1998a; Masters et al., 2011; Strateva et al., 2001; Schawinski et al., 2014; Blanton and Moustakas, 2009). Groups and clusters have a larger fraction of red galaxies, especially

nearer the centre (George et al., 2013; 1.2.2). An intermediary population exists between the red passive and blue star-forming populations known as the "green valley," so called due to its location in $u - r$ versus M_* phase space (Baldry et al., 2006; Strateva et al., 2001; Leslie et al., 2015; Figure 1.4).

1.1.3 Effective Radius

The effective radius (R_e) is a common measure of galaxy size. This is defined as the radius of a circle (or ellipse) enclosing half of the total light of the galaxy. The effective radius is also known as the half-light radius.

Galaxies do not have well-defined edges, and do not all have the same surface brightness profile. A standard system is therefore needed to quantify the total light from a galaxy and determine its half-light radius. The Petrosian (1976) system is one such system created in order to ensure photometric consistency across galaxies. Since this was the system used in the data reduction process for galaxies in my sample (see section 2.1.1), I will explain it briefly here.

The Petrosian flux is defined as the flux within a certain number, k, of r_P Petrosian radii:

$$F_P = 2\pi \int_0^{kr_P} I(r) r dr \tag{1.1}$$

where I(r) is the surface brightness profile of the galaxy, and r_P is the Petrosian radius satisfying:

$$\eta = \frac{I(r_P)}{2\pi \int_0^{kr_P} I(r) r dr / (\pi r_P^2)} \tag{1.2}$$

The "Petrosian ratio" η at a radius r from the centre is the ratio of the local surface brightness in an annulus at r to the mean surface brightness within r. In practise, such as for the Sloan Digital Sky Survey (SDSS)

(Yasuda et al., 2001), this implicit equation for η and r_P is replaced with:

$$\eta = \frac{2\pi \int_{0.8r_P}^{1.25r_P} I(r) r dr / \{\pi[(1.25r_P^2) - (0.8r_P^2)]\}}{2\pi \int_0^{kr_P} I(r) r dr / (\pi r_P^2)} \tag{1.3}$$

The Petrosian fluxes calculated in the SDSS and MaNGA are defined as the flux within 2 Petrosian radii ($k = 2$), and with η set to 0.2 (Yasuda et al., 2001; Wake et al., 2017). The aperture $2r_P$ was chosen to mimimize sky noise in F_P while containing nearly all of the flux for typical galaxy profiles. Effective radii values used for galaxies in this thesis (2.1.1) are determined from this elliptical Petrosian photometry.

1.1.4 Mass

Galaxies are comprised of stars, dust, gas, and dark matter. One way to determine the total mass of spiral galaxies is through rotation curves: the rotational velocity of the stars or gas in the galaxy is plotted against the distance to the galaxy's centre. Using Newton's Law of Gravity, the total mass within the orbit of the stars/gas can be obtained from the velocity curve. The discrepancy between the mass of a galaxy determined through its rotation curve, and that measured through its total luminosity - which traces the stellar component of the mass - was first noted by Rubin and Ford (1970). It is now understood that luminous matter makes up just a small component of the total mass of a galaxy, and that galaxies live in dark matter halos (Einasto et al., 1974; Wechsler and Tinker, 2018).

The total mass is difficult to measure, since galaxies are comprised mainly of dark matter. Instead, we can easily estimate the stellar masses (M_*) of galaxies. The M_* is most commonly estimated through spectral energy distribution (SED) fitting. The SED measures the flux of an object at a range of wavelengths. The SED fitting method assumes that the galaxy's spectrum can be approximated by a linear combination of individual stellar populations. The SED of a galaxy is compared to a library of synthetic spectra, which are created from Single Stellar Population templates (SSPs)

using stellar population synthesis (SPS) codes (e.g. Vazdekis et al., 2010; Sánchez-Blázquez et al., 2006; Falcón-Barroso et al., 2011). The SED of simple stellar populations depends on a set of characteristics such as the star formation rate, metallicity, and initial mass function[3]. By matching a galaxy SED with synthetic templates, properties such as stellar mass and star formation rate can be determined (e.g. Kennicutt, 1998a; Sánchez et al., 2016a).

Observational studies have found that many properties scale with stellar mass. Effective radius, metallicity, and mean stellar age increases with stellar mass (Lequeux et al., 1979; Garnett, 2002; Gallazzi et al., 2005; Lian et al., 2019), while atomic and molecular gas fractions decrease with stellar mass (Young and Scoville, 1991; Springob et al., 2005). Star formation rate (1.1.5) also tends to increase with stellar mass (Brinchmann et al., 2004); however, the specific star formation rate (star formation rate per unit mass) decreases with stellar mass (Feulner et al., 2005; Catalán-Torrecilla et al., 2017; Brinchmann et al., 2004). The passive (non-star-forming) fraction of galaxies increases steeply with stellar mass, total halo mass, and bulge mass (Bluck et al., 2014).

1.1.5 Star Formation Rate

Stars form in regions of dense cold gas known as molecular clouds. Stars are born when denser pockets of these clouds begin to collapse under their own self-gravity (see, for example, Disney et al., 1969). While detailed studies of the process of cloud contraction and fragmentation are best done by looking to nearby regions within our own galaxy, studying the collective effects of star formation over entire star-forming regions, or entire galaxies, can give insight into the large-scale processes involved in star formation. The star formation rate (SFR) parameterizes these processes; it is a measure of stars formed per year. By looking at the SFR of different regions within a galaxy,

[3]The initial mass function (IMF) describes the distribution of stellar masses in a newly formed population.

or by comparing the SFR amongst different galaxy populations, we can get a better understanding of how galaxies form and evolve. In addition, the mean specific star formation rate (sSFR) of galaxies over cosmic time is a key observable in cosmology and can tell us about galaxy growth and evolution over time.

The star formation rate of a galaxy can be estimated in a number of ways. For a complete overview of the various SFR determinations see Kennicutt (1998a) and Kennicutt and Evans (2012). The two main methods for determining SFR relevant to this thesis are via fitting the galaxy spectra to SSP models (see section 1.1.4) and estimating the SFR from measured Hα emission.

Hα (λ6563) is an excitation line of hydrogen in the Balmer series. Hydrogen gas is heated around stars with masses $> 10M_{\odot}$ and lifetimes < 20 Myr, and the resulting Hα emission provides a nearly instantaneous measure of the SFR (Kennicutt, 1998a). The first study of global SFR in galaxies using the Hα line was done by Kennicutt and Kent (1983). This method is still widely used today as it is one of the best-understood and most reliable measures of SFR, especially in nearby galaxies (Moustakas et al., 2006; Sánchez et al., 2016a; Brinchmann et al., 2004). The calibration commonly used between H-α luminosity, L(H-α), and the SFR is given by Kennicutt (1998a):

$$\mathrm{SFR}(\mathrm{H}\alpha) = 7.9 \times 10^{-42} \frac{L(\mathrm{H}\alpha)}{ergs\ s^{-1}}\ M_{\odot}\ yr^{-1} \tag{1.4}$$

where L(Hα) has been corrected for underlying stellar absorption and interstellar dust attenuation.

Using the Hα line as a measure of SFR has a number of advantages; not only does it allow a direct coupling between line emission and SFR, but it also has high sensitivity and facilitates mapping the SFR in nearby galaxies at high resolution (Kennicutt, 1998a). One of the primary limitations of Hα as a SFR indicator is its sensitivity to uncertainties in extinction, which is the scattering and absorption of ionized radiation by dust and

gas. However, it is less affected by dust extinction than other tracers such as ultraviolet emission (Glazebrook et al., 1999). Moustakas et al. (2006) found that extinction-corrected Hα, using a simple Milky Way extinction curve and the observed Balmer decrement[4], is a reliable SFR tracer even in highly obscured star-forming galaxies. Hα as a SFR tracer is also limited by the assumption that all of the massive star formation is traced by ionized gas (Kennicutt, 1998a) and that all of the ionizing radiation comes from star formation (Baldwin et al., 1981; see section 1.1.6).

The Star Forming Main Sequence

When plotting the star formation rate against stellar mass for a large sample of galaxies, two populations emerge (see Figure 1.5). The bi-modality in galaxy star formation rate generally follows that of colour (discussed in 1.1.2), with star-forming galaxies having the bluest colours, and non-star-forming, or passive galaxies, having the reddest colours (Glazebrook et al., 1999; Leslie et al., 2015). Galaxies with the highest SFRs in the low redshift Universe tend to be moderately massive ($10^{10} - 10^{11} M_{\odot}$) disc galaxies with high surface brightness, and half-light radii around 3kpc (Brinchmann et al., 2004). Galaxies lying above the star-forming population in the SFR-M_* plane are referred to as 'starburst' galaxies, which tend to have disturbed or irregular morphology (Wang et al., 2018).

The relation between the star-formation rate and stellar mass in the star forming population can be approximated by a linear relationship known as the star forming main sequence (Leslie et al., 2015; Brinchmann et al., 2004). This empirical relationship has been found to depend on the type of SFR indicator used, and the selection of the "star forming" population (Popesso et al., 2019; Belfiore et al., 2018). Main sequence galaxies are often

[4]The Balmer decrement is the ratio between the intensity of the Balmer lines of hydrogen. Interstellar dust causes a shift in the Balmer decrement from what is expected for star forming regions, thus, the observed Balmer decrement can be used to determine dust attenuation in galaxies.

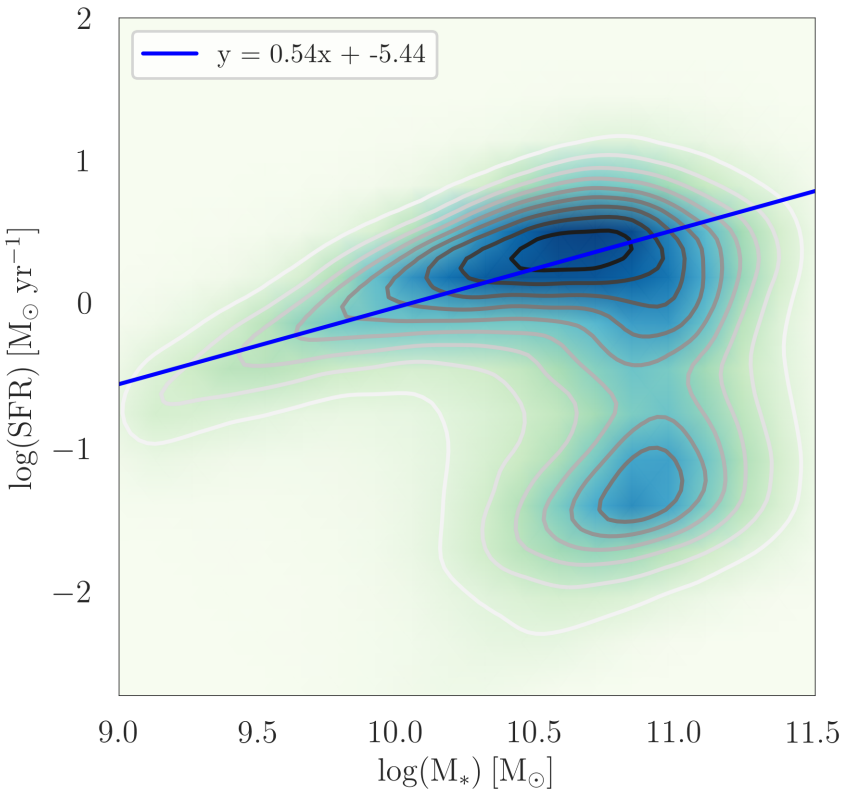

FIGURE 1.5: Star formation rate versus stellar mass of a large sample of galaxies ($\sim$ 700,000), shown using a gaussian kernel density estimation (kde). Data are from the SDSS (Salim et al., 2018). The main sequence line, y = 0.54x -5.44, is obtained from a fit to the data with sSFR $> 10^{-11}$yr^{-1}.

defined as galaxies that lie within one or two dex of the main sequence line (Belfiore et al., 2018).

The origin and nature of the SFR-M$_*$ relation is an area of active study in both observational and theoretical astrophysics. Since the SFR is heavily dependent on the amount of gas available and the surface density of the gas (Kennicutt, 1998b), models have focused on the interplay between gas accretion, star-formation and feedback-driven outflows in order to explain the nature of the main sequence relation and its scatter (Popesso et al., 2019; Hani et al., 2020; Matthee and Schaye, 2019). However, it is also well known that environment plays a role in where a galaxy lives in relation

to the main sequence: at a given M_*, galaxies in denser environments have lower SFR than galaxies in the field (Blanton and Moustakas, 2009; Schaefer et al., 2016). Resolved studies of galaxies can give more insight into the interplay between environment, stellar feedback, and other factors in determining the location and evolution of galaxies in relation to the main sequence.

Studies of the mean sSFR over cosmic time have revealed that more star formation was happening in the early Universe than it is today (see Madau and Dickinson, 2014, for a review). This has lead to the current consensus that, on average, galaxies start their lives as actively star forming, then move off of the main sequence, through the green valley, and into the "red-and-dead" region (Moustakas et al., 2013). The study of galaxy evolution is thus concerned with how galaxies move off of the star forming main sequence as their star formation shuts off. Any process that causes the star formation activity in a galaxy to cease is known as "quenching." A small number of galaxies also "rejuvenate," that is, go from passively evolving to actively star forming (Schawinski et al., 2007; Chauke et al., 2019). This thesis is concerned primarily with galaxy quenching, which will be further discussed in 1.3.

1.1.6 Active Galactic Nuclei

Some galaxies have compact, super luminous regions at their centre called active galactic nuclei (AGN). These regions of excess luminosity have been observed across the entire electromagnetic spectrum, and their spectra and luminosity indicate that their emission does not come from stars (Seyfert, 1943; Greenstein and Schmidt, 1964). It is now understood that AGN emission comes from the accretion disk of supermassive black holes in the galactic centre (Lynden-Bell, 1969; Shakura and Sunyaev, 1973; McCray, 1979; Begelman, 1985). An accretion disk is formed when gas falls towards the central black hole and energy is dissipated either through radiation or is retained as heat (Begelman, 1985). This accretion flow is the source of X-ray, optical and ultraviolet (UV) emission, which ionizes the surrounding

gas creating line emission (Koratkar and Blaes, 1999). A spinning accretion disk can also act as the driver for jets, which become collimated due to the magnetic stress of the disk wind (see Blandford et al., 2019 for a review of AGN jets). These jets can be relativistic and tens to hundreds of kiloparsecs in length (Ferrari, 1998; Zhai et al., 2014). AGN jets were first identified as strong radio sources (Jennison and Gupta, 1953; Schmidt, 1963), but are also sources of γ-ray (e.g. Dermer and Giebels, 2016) and X-ray emission (Hogan et al., 2011).

AGN activity is thought to impact the evolution of its host galaxy, especially its star forming status (Springel et al., 2005; Kauffmann et al., 2003; Sijacki et al., 2007). Some research has shown that galaxies with AGN have enhanced star formation (Kauffmann et al., 2003; Silverman et al., 2009). However, more recent studies that account for trends in SFR and AGN with stellar mass have shown that AGN act to quench galaxies from the inside out (Salim et al., 2007; Shimizu et al., 2015; Ellison et al., 2016; Wang et al., 2018). The presence of AGN is therefore an important factor to take into account when doing large scale statistical studies of galaxy evolution.

There are a number of ways to detect AGN, due to their strong continuum and line emission across the electromagnetic spectrum. Aside from their extraordinary luminosities, AGN are unique in that they show similarity in their spectral features across seven orders of magnitude in luminosity (Koratkar and Blaes, 1999) - making them relatively easy to identify. Of interest to this thesis is the detection of AGN through line emission, particularly, their strong Hα emission (Schmidt, 1963).

It is necessary to distinguish Hα emission that comes from AGN from that of star formation. One such system for identifying the source of extragalactic emission was devised by Baldwin, Philips, and Terlevich (1981). Since different objects have characteristically different spectra, Baldwin et al. (1981) developed a system for classifying extragalactic objects based on the relative strengths of easily-measured lines, such as OIII/Hβ, NII/Hα,

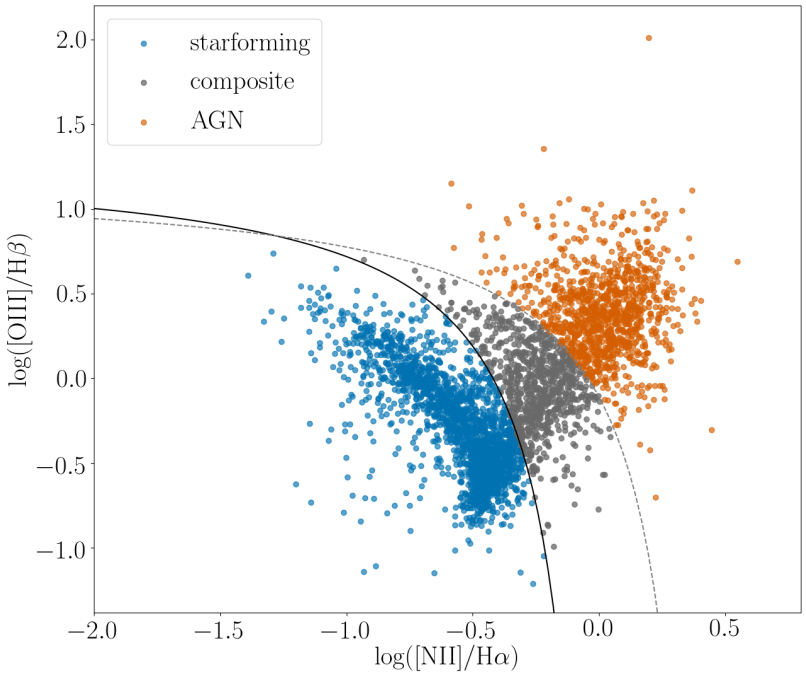

FIGURE 1.6: An example of a BPT diagram created in order to classify galaxies in my sample. Galaxies are classified as star-forming, AGN, or both (composite) based on the relative strengths of their emission line ratios. This system was originally proposed by Baldwin et al. (1981), but we use the updated demarcation lines of Kewley et al. (2006). The solid black line divides the star-forming and the composite regions, while the dashed grey line divides the composite and AGN regions of the plot. The emission line fluxes of each galaxy are integrated within a central 2.5 arcsecond aperture (Sánchez et al., 2016b).

and SII/Hα. Objects are placed on an emission-line ratio phase-space diagram, now referred to as a Baldwin Philips and Terlevich (BPT) diagram, and their location on this diagram indicates the source of the emission. Figure 1.6 illustrates the BPT classification scheme using galaxies in my sample.

1.2 Galaxy Environments

Galaxies live in different environments, which can have significant effects on their evolution. The proximity of a galaxy to other galaxies, its location within its halo, and the mass and density of its surroundings have been found to influence some of the properties discussed above, such as star formation rate, stellar mass, colour, and morphology (Blanton and Moustakas, 2009; Carollo et al., 2013; Schaefer et al., 2016; Demers et al., 2019). There are a number of ways that environment can be defined, including group or cluster halo mass, projected nearest neighbour density[5], group-centric radius, or whether the galaxy is a central or satellite[6], to name a few (Carollo et al., 2013). An important division I make in this thesis is between field (isolated) galaxies and group or cluster galaxies. This section discusses attributes of galaxies within these two broad categories, as well as further investigations of galaxies based on environment relevant to this thesis.

1.2.1 Field

Field galaxies in this thesis are defined as galaxies not gravitationally bound to other galaxies of similar mass. These isolated galaxies are not influenced by other galaxies, nor the hot gas that permeates the surroundings

[5]Originally prescribed by Dressler (1980), the nearest neighbour density is determined by measuring the distance r to the Nth nearest neighbour, and then measuring the surface density within a circle whose radius is r.

[6]"Centrals" are galaxies that live at the centre of their dark matter halo. "Satellites" are group or cluster galaxies that do not live at the centre of their dark matter halo.

of galaxies in groups and clusters. They are therefore ideal for studying how galaxies evolve internally due to their mass, structure, or any AGN activity. An understanding of isolated galaxies is necessary in order to distinguish internal from external processes in galaxy evolution.

Many observational and theoretical studies have looked at the internal properties and evolution of isolated galaxies in an effort to gain a baseline for how galaxies behave on their own (Varela et al., 2004; Márquez and Moles, 1999; Mayer et al., 2008; Hwang et al., 2012; Alpresa et al., 2010). These studies have found that the fraction of elliptical and lenticular galaxies is lower in the field than in groups (Dressler, 1980; Márquez and Moles, 1999; Varela et al., 2004; Wel, 2008). Field galaxies tend to be blue spiral galaxies, with higher star-formation rates than those in groups (Varela et al., 2004; Blanton and Moustakas, 2009).

1.2.2 Groups and Clusters

Groups and clusters are collections of a few to thousands of galaxies gravitationally bound to one another. By the original Abell (1958) definition, galaxy clusters contain anywhere from 30 to thousands of members. They have total masses ranging from 10^{14} to 10^{15} solar masses (Applegate et al., 2014; Yang et al., 2007). On the other hand, galaxy groups contain about 30 or fewer members; group masses are typically on the order of 10^{13} solar masses (Lim et al., 2017; Yang et al., 2007). The total mass of a group or a cluster is referred to as the 'halo mass' - the member galaxies of a group or a cluster all live in the same dark matter halo, which accounts for most of the mass (Zwicky, 1933) and encompasses the entire group or cluster. Permeating the galaxies in groups and clusters exists the intragroup medium or intracluster medium (ICM), which is a hot plasma (10-100 megakelvins) comprising mainly of ionized hydrogen and helium (Mitchell et al., 1976; Serlemitsos et al., 1977).

Most galaxies, groups, and clusters themselves belong to larger structures known as superclusters. Our Milky Way galaxy belongs to the Local

Group, which is part of the Virgo Supercluster, which is part of the Laniakea Supercluster (Tully et al., 2014). Unlike groups and clusters, superclusters expand with the Hubble expansion (Chon et al., 2015). Therefore, groups and clusters are the largest known gravitationally bound structures in the Universe.

There are a number of observational techniques for identifying groups and clusters. A common method is to use optical imaging to find overdensities (Abell, 1958), and then confirming by checking that the galaxies are at a consistent redshifts using spectroscopy (e.g. Gunn et al., 1986). The ICM plasma emits in the X-ray, making X-ray telescopes another useful tool for detecting groups and clusters (Mitchell et al., 1976; Bower et al., 1994), although this is more effective for identifying more massive clusters (Connelly et al., 2012). Gravitational lensing (Einstein, 1936) can also be used to identify massive clusters: the observed distortion of background galaxies can be used to determine the amount of mass in the foreground cluster (Zwicky, 1937; Postman et al., 2012).

Of interest to this thesis is the identification of group and cluster members via group-finding algorithms. In general, group-finding algorithms take into account the projected surface density as well as redshift information to place galaxies in groups and clusters. The 'friends of friends' (FoF) algorithm is an example of a basic group-finding algorithm that defines a linking length and iteratively links all galaxies within a particular linking volume centred on each galaxy (Eke et al., 2004). Yang et al. (2007) used a similar process to identify groups and clusters in the Sloan Digital Sky Survey (SDSS), however, they improved upon the FoF algorithm by estimating halo mass based on the luminosity of galaxies within the group, and then using the velocity dispersion corresponding to that mass as part of the iterative process to help determine group members. This algorithm was further updated by Lim et al. (2017) with improved assignment for lower mass halos.

As previously noted, galaxies in groups and clusters tend to have elliptical and lenticular morphology, or are more bulge-dominated, than galaxies

in the field (Dressler, 1980; Varela et al., 2004; Yang et al., 2007; George et al., 2013; Wel, 2008; George et al., 2013). They tend to be redder in colour and have lower star star formation rates than field galaxies (Varela et al., 2004; Blanton and Moustakas, 2009; Schaefer et al., 2016; Medling et al., 2018). Even the lowest mass groups show reduced SFRs relative to the field (Martínez et al., 2002).

Further classifications of galaxies based on group or cluster halo mass, and proximity to the halo centre, can help to elucidate the influence of environment on these observed properties and on galaxy evolution. When studying the influence of environment on galaxy properties, however, it is important to control for stellar mass. While it is clear that there is a stark difference in properties when comparing field and group or cluster galaxies, recent studies have found that, within groups and clusters, stellar mass has a more significant effect on galaxy morphology, colour, metallicity, and star formation rate than halo mass or halo-centric distance (Pasquali et al., 2009; Vulcani et al., 2014; Medling et al., 2018; Lian et al., 2019). Studies of the influence of halo-centric distance on galaxy properties must account for any presence of mass-segregation in groups, a phenomena whereby galaxies tend to be most massive at the halo centre and decrease in mass with increasing halo-centric distance (e.g. Roberts et al., 2014; Kafle et al., 2016).

1.3 Galaxy Quenching

Since stars are born out of cold molecular gas (1.1.5), any process that removes the cold gas or cuts off the cold gas supply will cause star formation to stop. This is called "quenching," and a galaxy with very little star formation activity is called "quenched". Galaxies in groups and clusters have systematically lower star formation rates than galaxies in the field. Studies seeking to understand the physical mechanisms that drive quenching look to both external and internal processes. The question remains whether quenching primarily occurs as a result of the group or cluster environment, or whether a reduction in star forming activity is part of a galaxy's

evolution, irrespective of environment. Some of the key internal and environmental quenching mechanisms that have been proposed are discussed in this section, as well as observational constraints on quenching mechanisms.

1.3.1 Internal Quenching Mechanisms

Internal quenching mechanisms are any processes within a galaxy that act to heat up or expel cold gas from the galaxy, thereby removing the fuel necessary for star formation. The existence of quenched galaxies in the field (Baldry et al., 2006; Geha et al., 2012) supports the idea that internal mechanisms play a role in galaxy quenching. Numerous ideas have been proposed for internal quenching mechanisms, including: stellar feedback, AGN feedback, halo mass quenching, and morphological quenching.

Stellar Feedback

Stellar feedback was first proposed by White and Rees (1978) as a means of preventing over-cooling of halo gas and excessive star formation in galaxy simulations. Stellar feedback is the process of the heating of gas through young stars via ionising radiation, stellar winds, or supernova explosions (McKee and Ostriker, 1977). While stellar feedback plays an important role in galaxy formation and evolution, it does not provide enough energy to account for quenching timescales, which are longer than the gas cooling time (Pontzen et al., 2016). Therefore, an additional energy source is required.

AGN Feedback

AGN produce a lot of energy that can either heat up the surrounding gas, prevent cool gas from accreting, or expel the gas through powerful jets. In addition to stellar feedback, AGN feedback is now included in many theoretical, numerical, and semi-analytic models as a mechanism to prevent cooling of the gas or expel cool gas to slow down star formation and limit the growth of central super-massive black holes (Springel et al., 2005; Sijacki et al., 2007; Schaye et al., 2015). That star formation is suppressed

in galaxies with powerful AGN is observational evidence for AGN feedback (Schawinski et al., 2006; Page et al., 2012).

Halo Mass Quenching

It is thought that in massive galaxies above some critical mass $M_* \gtrsim 10^{12}$ $M_\odot$, infalling gas undergoes virial shock heating, starving galaxies of cool gas (Birnboim and Dekel, 2003; Kereš et al., 2005). Since central galaxies (either isolated or in groups) by definition are less likely to be subjected to environmental quenching, a combination of AGN feedback and halo gas shock-heating could be the main drivers of quenching in central galaxies (Medling et al., 2018; Chen et al., 2020). Lin et al. (2019) classified galaxies in the Mapping Nearby Galaxies at Apache Point Observatory (MaNGA) integral field unit (IFU) survey (see 2.1.1) as either having inside-out quenching, which indicates the existence of an internal process such as AGN feedback, or outside-in quenching, which is a signature of an external quenching mechanism. They found that the fraction of galaxies showing inside-out quenching increases with halo mass, irrespective of stellar mass or environment.

Morphological Quenching

For star formation to take place, there must be gravitational instabilities in the disk that allow for the cold gas to clump and collapse. Morphological quenching is the process whereby the structure of the galaxy changes, resulting in stability of giant molecular clouds against collapse (Martig et al., 2009). For example, the bulge component of the galaxy is thought to create tidal torques that stabilize the disk against star formation (Martig et al., 2009; Bluck et al., 2014). There is some observational evidence to support this idea: it has been shown that green valley galaxies have more massive bulges than main sequence galaxies (Moustakas et al., 2006; Belfiore et al., 2018). On the other hand, studies have indicated that the presence of a bulge is correlated with a reduction in star formation but not sufficient to

fully quench a galaxy (Fang et al., 2013; Wang et al., 2018; Eales et al., 2020).

1.3.2 Environmental Quenching Mechanisms

There is evidence that with increasing environment density, star formation in galaxies is suppressed (Blanton and Moustakas, 2009; Schaefer et al., 2016). The study of environmental quenching seeks to explain this suppression. Environmental quenching mechanisms are any processes that remove or heat gas in a galaxy as a result of the galaxy interacting with its surrounding environment, thereby removing the fuel available for star formation. These mechanisms can be divided into two general categories: galaxy-galaxy interactions, and galaxy-halo interactions.

Galaxy-Galaxy Interactions

Galaxies in a high density environment will interact gravitationally with one other in a number of ways, which can sometimes lead to quenching. Some examples of interacting galaxies are shown in Figure 1.7, illustrating galaxies in various stages of collision. The mergers of galaxies can cause a starburst event, followed by quenching: greater instability in the gas causes rapid star formation that depletes the cold gas (Dekel and Burkert, 2014; Cortijo-Ferrero et al., 2017). Tidal interactions in groups can also cause quenching, either by triggering a starburst event (Moore et al., 1998), or through the stripping of gas and other material of a satellite by a more massive galaxy (Toomre and Toomre, 1972; Merritt, 1983). In high-speed fly-bys, the galactic disk is disturbed in what is known as harassment. Harassment can lead to starburst events or to morphological quenching (Lake and Moore, 1999).

Observations indicate that galaxy interactions and mergers become increasingly common at higher redshifts, when the Universe was smaller and denser (Giavalisco, 2002). Not all of these processes scale with galaxy density, however. Major mergers are more likely to occur in smaller groups

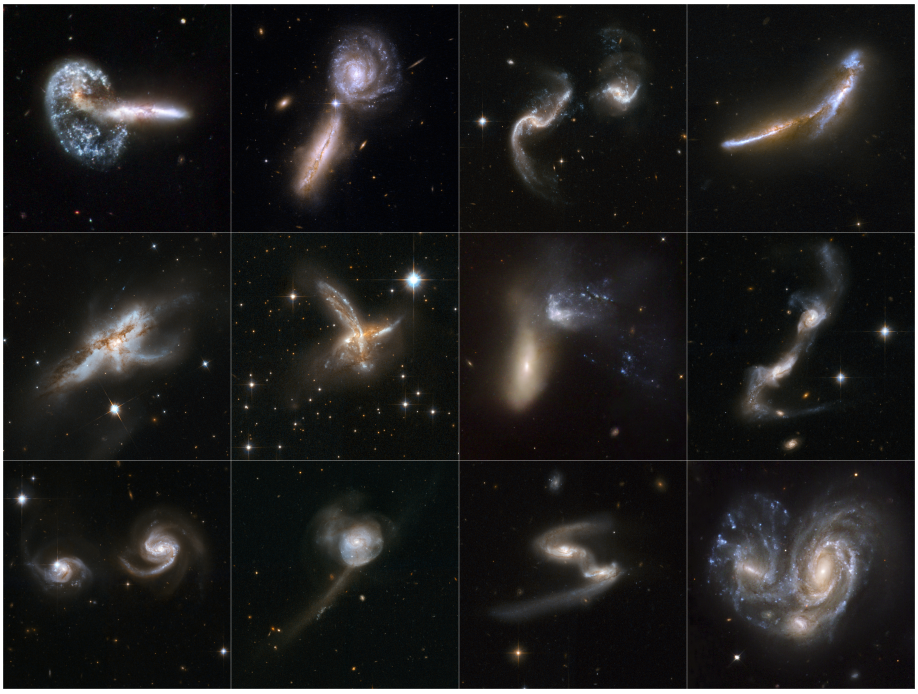

FIGURE 1.7: Images from the GOALS project (Great Observatories All-sky LIRG Survey) capturing galaxy mergers and interactions. Source: NASA et al. (2008).

where galaxies are moving more slowly (Moore et al., 1996; Cortese et al., 2006).

Galaxy-Halo Interactions

As a galaxy moves onto or through the group or cluster, it interacts gravitationally with the dark matter halo and hydro-dynamically with the hot gas that permeates the halo (the ICM). Starvation and ram pressure stripping are two types of galaxy-interaction processes that have been proposed to explain environmental quenching.

As a galaxy falls into a group or a cluster, quenching can happen through what is called "starvation" or "strangulation," so named because the group or cluster halo starves the in-falling galaxy of its fuel for star formation. The cold gas within galactic disks is ordinarily replenished from the intergalactic medium (IGM) (Larson, 1972; Sancisi et al., 2008). When the galaxy falls

into the group or cluster, its own gaseous halo can be swept up by the larger halo, and any in-falling IGM gas instead falls onto the group or cluster halo. The in-falling galaxy therefore loses its gas reservoir. The process of starvation is expected to be slow, since the galaxy will still form stars from the cold gas reservoir in the disk, and to produce a uniformly suppressed star-formation across the whole galaxy (Larson et al., 1980). In an analysis of MaNGA data, both Spindler et al. (2018) and Belfiore et al. (2018) found a uniform suppression of star formation in satellites at all galactic radii compared to centrals, which also supports strangulation as a key process in environmental quenching.

Galaxies can also become quenched as they move through the halo via ram pressure stripping. Ram pressure is the increased pressure a body experiences due to its motion through a fluid. The faster an object moves through a fluid of a given density, the more particles it hits, so the more pressure it experiences. Ram pressure stripping of galaxies was first proposed by Gunn and Gott (1972), who calculated the ram pressure that a galaxy would experience moving through the ICM and determined that it was more than the force a typical spiral galaxy has to hold onto its gas. A number of hydrodynamic simulations and semi-analytic models have explored the effects of ram pressure stripping (e.g. Abadi et al., 1999; Quilis et al., 2000; Book and Benson, 2010). One of the key results of simulations is that ram pressure stripping would cause a truncation of its gaseous disc, a prediction that matches observational studies that have found star formation is confined to the central regions of galaxies in groups and clusters (Schaefer et al., 2016; Medling et al., 2018; Finn et al., 2018; Lian et al., 2019). Ram pressure is thought to be most effective in the most dense environments (Abadi et al., 1999; Singh et al., 2019), and nearest the cluster centre (Vollmer, 2009), and indeed evidence of ram pressure stripping has been found in galaxies in rich clusters (Oosterloo and van Gorkom, 2005; Lee et al., 2017). Weak ram pressure stripping has been shown to be less effective at removing the gas, and can also sometimes enhance star formation by compressing the gas (Tonnesen and Bryan, 2009).

1.3.3 Outline of this Thesis

We have learned a great deal about the properties of galaxies over the past hundred years; however, there remain some broad questions within the field of galaxy evolution about how star formation is being shut off: What are the dominant processes that cause quenching? Which has a bigger effect - processes that occur from within the galaxy, or from the galaxy interacting with its environment? Whether quenching is happening internally or externally will result in different patterns of star formation that we see. For example, environmental processes are thought to cause an outside-in type pattern of quenching, as is the case for ram pressure stripping, or a uniform quenching across the galaxy via strangulation. On the other hand, internal quenching mechanisms such as AGN feedback are thought to result in an inside-out pattern of quenching. The question that I address in this thesis is: What is the dependence of the spatial pattern of star formation on environment, and can we use this information to constrain quenching mechanisms? Chapter 2 is an overview of the data used and methods of analyzing the star-forming disks of nearby galaxies. The integrated star formation in each galaxy is mapped via the strength of the Hα line. Resolved Hα properties are then measured at fixed stellar mass and compared in different environments. Chapter 3 presents the results of these analyses. We find that star formation is suppressed at all galactic radii in groups or clusters compared to the field, and that star forming disks are truncated nearer group or cluster centres. Finally, Chapter 4 contains a discussion of the results presented and implications for constraining quenching mechanisms, as well as ideas for future work.

Chapter 2

Data and Methods

2.1 Sample

2.1.1 Galaxy Data

Galaxy data were obtained from the Mapping Nearby Objects at Apache Point Observatory (MaNGA) survey, data release 16 (DR16), which contains 4675 galaxies (Bundy et al., 2015; Law et al., 2015; Yan et al., 2016). The MaNGA survey uses an integral field unit (IFU) spectrograph to collect the resolved spectra for ∼10,000 nearby galaxies in the Sloan Digital Sky Survey (SDSS).

MaNGA Target Selection and Observations

Galaxy targets for MaNGA were chosen such that the 10,000 galaxies could be divided into groups that adequately sample each of the three "principle components" defining a galaxy population: stellar mass (M_*), star formation rate (SFR), and environment (Bundy et al., 2015).

The MaNGA sample covers a stellar mass range of 5×10^8 to 3×10^{11} $M_\odot/h^2$ (Wake et al., 2017) (see Figure 2.1). One of the science requirements for the survey was to have a flat distribution of stellar mass, M_* so that studies of mass-dependent trends could make use of adequate numbers of high-mass compared to more numerous low-mass systems (Bundy et al.,

2015). Note that for the data released thus far, the stellar mass distribution is not flat below $M_* \sim 10^{9.5} M_\odot$ nor above $M_* \sim 10^{11} M_\odot$ (see Figure 2.1).

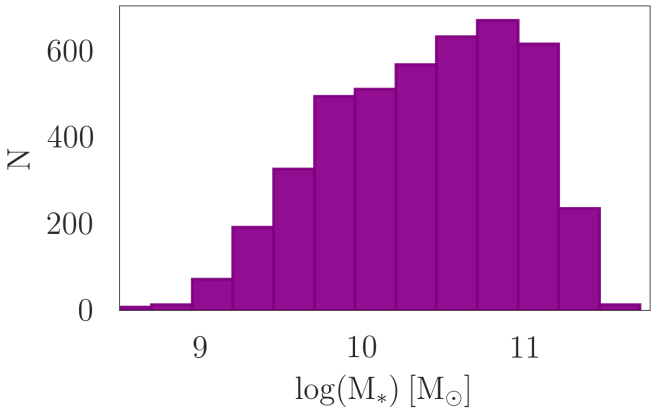

FIGURE 2.1: The stellar mass distribution of MaNGA galaxies.

Galaxies in the MaNGA survey are imaged by IFUs, which contain tightly packed arrays of optical fibres. These fibres are fed to the BOSS spectrographs (Smee et al., 2013) such that each fibre yields a spectrum at a different position in the galaxy. Each fibre has a 2" diameter, and the fibres are bundled together in groups of 19, 37, 61, 91 or 127 fibres per IFU; the bundle chosen for each galaxy target depends on the target's angular size. A key objective of the survey was to have full spectral coverage out to 1.5 R_e for $\sim 50\%$ of the sample (called the Primary sample), and 2.5 R_e for $\sim 40\%$ of the sample (the Secondary sample). The remaining galaxies were targeted as part of the Colour Enhanced sample, which was introduced to be able to include star-forming massive galaxies and non-star-forming low-mass galaxies, and is selected based on the *NUV-i* colour (Wake et al., 2017).

The redshift range of MaNGA targets ($0.02 < z < 0.15$, see Figure 2.2) was selected to balance angular size and resolution. Note that the roughly uniform radial coverage in R_e means that galaxies do not have the same physical spatial resolution across the sample (Wake et al., 2017). To increase resolution, IFU observations are dithered: since there are spaces between the fibres, each galaxy is imaged a minimum of three times, with

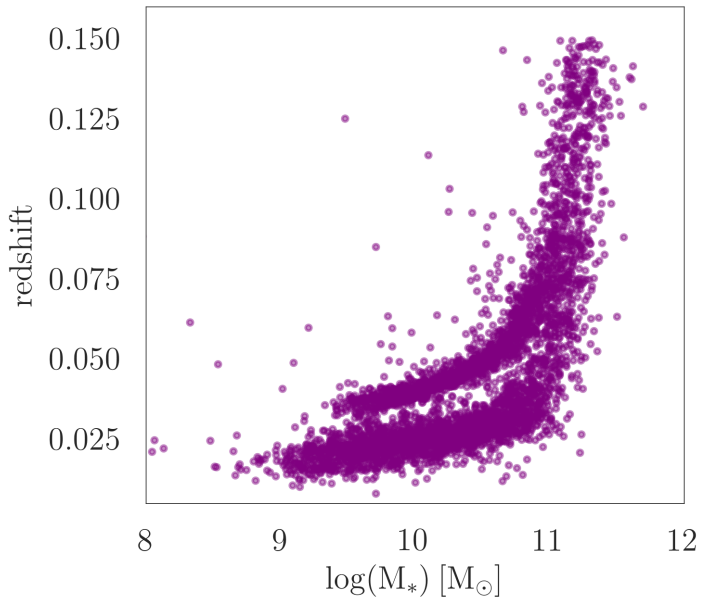

FIGURE 2.2: Redshift and stellar mass distribution of MaNGA galaxies. Note the offset distribution of the Primary and Secondary samples: galaxies in the Secondary sample are at higher redshift to facilitate increased radial coverage in R_e.

the IFU slightly offset in each pointing. Dithering the IFU maximizes the spatial information obtained to yield a combined signal to noise ratio (SNR) of 5 $Å^{-1}$ per fibre in the r-band continuum. Each IFU has a spectral coverage of 3600 - 10,000 Å and a typical spectral resolution of R $\sim$ 2000 (where R = $\lambda/\Delta\lambda$) (Law et al., 2015). The spectra have a median spatial resolution of 2.5", full width at half maximum (FWHM), or 1.8 kpc at the median redshift of z $\sim$ 0.037 (Drory et al., 2015; Law et al., 2015; Law et al., 2016b).

Data Reduction and Value Added Catalogs

The Data Reduction Pipeline (DRP) processes the raw data to produce flux-calibrated, sky subtracted, coadded datacubes for each exposure of a given galaxy (Law et al., 2016b). Each datacube contains two spatial dimensions and one spectral dimension. The spectral data for each cube

are stored in what is called "spatial pixels" or "spaxels," 0.5×0.5 arcseconds in size.

The datacubes are then processed by the Data Analysis Pipeline (DAP) (Westfall et al., 2019; Belfiore et al., 2019). The DAP measures the shape and location of spectral features, fits stellar population models, and derives astrophysical quantities. Data provided by the DAP include, for example: spatially stacked spectra, continuum and line SNR, stellar kinematics, and emission line properties such as flux and equivalent widths (EW).

Of primary interest to this thesis are the DAP's EW measurements. An EW measurement is defined as the width of a rectangle whose height is the continuum emission and area is the area of the spectral line. These measurements are obtained in two ways in the DAP, details of which can be found in Westfall et al. (2019) and Belfiore et al. (2019). The first method is through Gaussian line-profile modeling using a full-spectrum fit with pPXF, a spectral fitting routine (see Cappellari and Emsellem, 2004; Cappellari, 2016). The first full-spectrum fit of the DAP uses pPXF to derive stellar kinematics. The second fit models all emission-line features and re-optimizes the weights of the spectral templates to the underlying stellar continuum (Westfall et al., 2019). Whereas stellar kinematics are determined using binned spectra (spaxel spectra grouped together so that their combined SNR > 10), the stellar-continuum+emission-line fit is performed for individual spaxels.

Equivalent widths are also calculated based on non-parametric emission-line measurements, which only differ significantly from the Gaussian line measurements at low flux levels. The zeroth moment of the continuum-subtracted spectra is computed and combined with measurements of the local continuum to determine non-parametric equivalent widths (Westfall et al., 2019).

Note that all emission-line fluxes have been corrected for Galactic foreground extinction because the spectra are de-reddened before being modelled. However, the line fluxes are not corrected for attenuation by dust

within the target galaxy itself (Westfall et al., 2019).

The main output of the DAP are two dimensional maps containing DAP-derived data, which can be accessed via the SDSS website or through Marvin (Cherinka et al., 2019). Marvin consists of a Python package, Application Programming Interface (API), and web application for downloading and interacting with MaNGA datacubes and maps. Using the Marvin Python package, signal to noise ratio, Petrosian elliptical coordinate, and emission line maps were accessed for further analysis (see section 2.2).

There are also a number of value added catalogs (VAC) derived using the MaNGA data. Properties not available from the DAP were obtained from the Pipe3D VAC (Sánchez et al., 2016a; Sánchez et al., 2016b). The Pipe3D pipeline is an analysis pipeline using the FIT3D fitting tool, a set of algorithms designed to analyze the properties of stellar populations and ionized gas of IFU data (Sánchez et al., 2016a). FIT3D is a stellar population synthesis code that models and subtracts the stellar spectrum and fits emission lines using the GRANADA (Martins et al., 2005) and MILES (Sánchez-Blázquez et al., 2006; Vazdekis et al., 2010; Falcón-Barroso et al., 2011) simple stellar population (SSP) libraries. The output from the Pipe3D pipeline are individual data files for each galaxy containing spatially resolved properties such as star formation histories, emission line fluxes, stellar absorption indices and stellar population properties (Sánchez et al., 2016b). The pipeline also provides a catalog of properties, integrated within the field of view (FOV) of the MaNGA datacubes. The integrated star formation rates and stellar masses were obtained from this catalog, as well as emission lines from the central 2.5" aperture; these data were primarily used to put constraints on our selection (see section 2.1.3).

2.1.2 Group Data

Group information were obtained primarily from the Lim et al. (2017) group catalog and supplemented with the Yang et al. (2007) group catalog. The Lim et al. (2017) group catalog is a halo-based group finder based on the

group finder of Yang et al. (2007) and Lu et al. (2016), but with a more uniform and improved halo mass assignment over a wider range of halo masses. It uses four large surveys: 2MRS (Two Micron All-Sky Redshift Survey), 6dFGS (Six-degree Field Galaxy Survey), SDSS (Sloan Digital Sky Survey) and 2dFGRS (Two-degree Field Galaxy Redshift Survey) to construct group catalogs in the low-redshift Universe. Data obtained from the group catalogs include group mass, group centre, and group membership.

Briefly, galaxies are assigned to groups as follows (see Lim et al. (2017) for more information): in the first step, a preliminary halo mass is assigned to every galaxy based on a galaxy stellar mass (luminosity) - halo mass relation obtained from a hydrodynamical simulation. In the second step, galaxies are assigned to groups based on the physical properties of dark matter halos expected from the current cold dark matter cosmology, such as halo mass, virial radius, and velocity dispersion. The stellar mass-weighted (or luminosity-weighted) centre of the member galaxies is then identified. In the third step, groups are ranked based on their halo mass proxies. For groups with only one member, this is the galaxy stellar mass - halo mass relation. For groups with more than one member, the halo mass proxy is obtained using the 'GAP correction' method of Lu et al. (2016). This method uses a combination of the luminosity/stellar mass of the central galaxies, and the luminosity/stellar mass GAP (the difference in luminosity/stellar mass between the central galaxy and the n-th brightest galaxy) to compute a group mass proxy. In step four, group masses are updated using abundance matching between the mass function of the preliminary groups and an adopted theoretical mass function. Steps two through four are then iterated until convergence in group membership is achieved.

2.1.3 Sample Selection

Of the 4656 galaxies processed in the Pipe3D pipeline (Sánchez et al., 2016b), 4456 galaxies were matched to group data from Lim et al. (2017) and Yang et al. (2007). Any cubes flagged as 'critical' in either the DRP or

the DAP were then removed. Cubes are marked as critical for a variety of reasons including, for example, poor focus due to hardware failure, failed astrometric registration due to a bright star, or cosmic rays confusing the flux calibration routine (Law et al., 2016b). Law et al. (2016b) and Westfall et al. (2019) note that any galaxies marked as critical due to any issues caught in either the DRP or DAP, respectively, should be used with extreme caution or omitted from science analyses. After removing the 76 galaxies with the 'critical' flag, the sample consisted of 4380 galaxies.

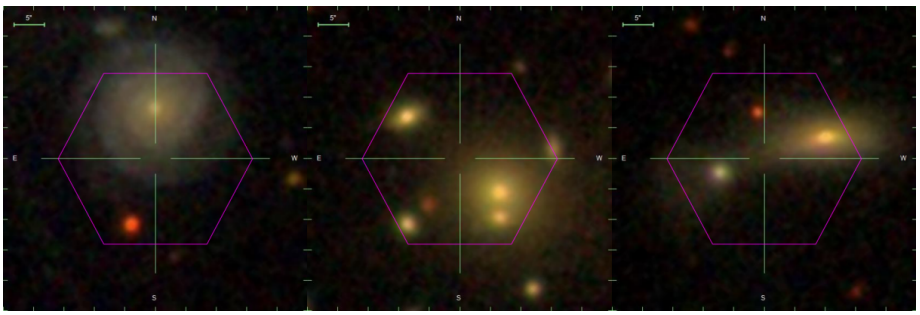

FIGURE 2.3: Examples of MaNGA galaxies for which the target galaxy centre has a large offset from the IFU centre. These galaxies were removed from the sample. Images are obtained from the Marvin web interface through their IFU-ID (Cherinka et al., 2019).

A few of the MaNGA galaxies in this sample have very large pointing offsets, and were removed (for examples, see Figure 2.3). Galaxies identified as mergers by eye were also removed, leaving 4310 galaxies.

We limit our stellar mass range to $10^9 < M_* < 10^{11.5}$ $M_\odot$ in order to have an adequate number of galaxies in each mass bin (see Figure 2.1). Galaxies are subsequently subdivided into smaller mass bins with an approximately equal number in each mass bin. After stellar mass cuts there were 4254 galaxies. To differentiate between the different galaxy environments, we defined field galaxies as having a group number of n=1, and galaxies in groups as having a group number of n > 2 and $M_{halo} > 10^{13} M_\odot$, as identified in the Lim et al. (2017) and Yang et al. (2007) group catalogs. Thus, galaxies in pairs were removed from the sample. The total number of isolated galaxies is 1601 and group galaxies is 1228. Thus, the sample after

the initial cuts consists of 2829 galaxies, and will be referred to as the MaNGA sub-sample.

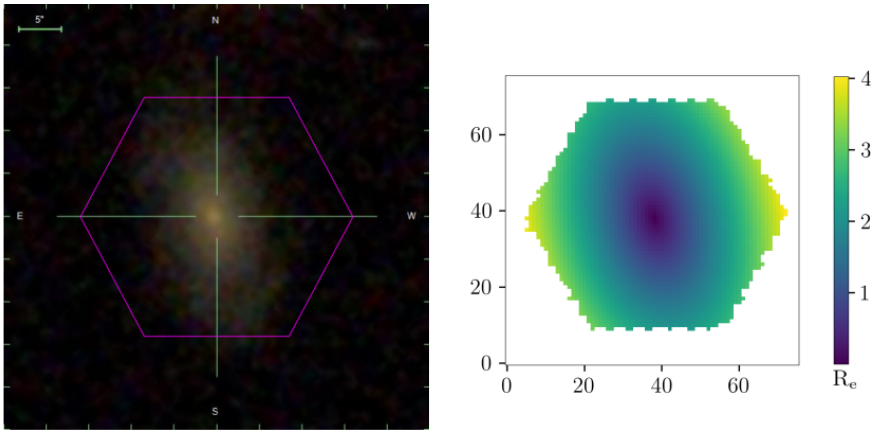

FIGURE 2.4: Left: The SDSS image of a sample galaxy. Right: R_e map of the same galaxy. Both the image and map were created using the Marvin Python package of Tools (Cherinka et al., 2019).

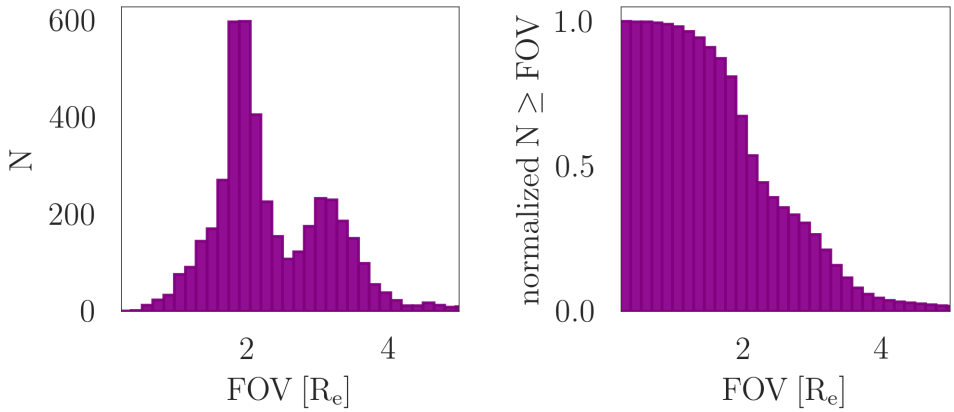

FIGURE 2.5: Left: The FOV coverage of all MaNGA galaxies. Right: The normalized cumulative distribution of MaNGA FOV coverage showing that ∼60% are mapped to $2R_e$.

To ensure consistency in spatial coverage of galaxies across the sample, galaxies not covered out to 2 effective radii (R_e, see section 1.1.3) were removed. The cutoff at $2R_e$ was chosen in order to balance wanting to examine as large an extent of the galaxy as possible while maintaining an adequate sample size. The IFU coverage of each galaxy in R_e was

determined by taking the maximum effective radius value covered by the IFU footprint, which gives the coverage along the short axis (b) of the galaxy, and then weighting this value by the axis ratio (b/a) to determine the coverage along the long axis (a), in effective radii (see example in Figure 2.4).

Figure 2.5 shows the distribution of FOV coverage for MaNGA galaxies; for about 60% of the MaNGA sample, the FOV encloses up to $2R_e$ of the galaxy along the long axis. Of the 2829 galaxies after the initial cuts, 1600 galaxies are covered out to $2R_e$ (981 isolated and 619 in groups). This sample is referred to hereafter as the $2R_e$ FOV sample, or simply 'the sample.'

Star-forming Galaxies

A primary goal of this thesis is to explore how the distribution of star formation in star-forming galaxies differs in different environments. We use two different methods to classify galaxies based on their global star formation rate. The distribution of the specific star formation rate (sSFR - star formation rate per stellar mass) of the MaNGA sub-sample is shown in Figure 2.6. Any galaxy with sSFR $> 10^{-10.8}\mathrm{yr}^{-1}$ is classified as star-forming. This cut is similar to other definitions of star-forming galaxies in the literature (e.g. Wetzel et al., 2013; sSFR $> 10^{-11}\mathrm{yr}^{-1}$), and we found that shifting this sSFR cut off slightly did not significantly change the results. Galaxies were also classified based on where they lay in relation to the main sequence in the logarithmic SFR-M_* plane. A main sequence line was fit to the MaNGA data (Figure 2.7), and the distance from the main sequence line, ΔMS, computed for each galaxy (Figure 2.8). While we present our findings using the sSFR cut to classify galaxies, using the ΔMS to classify galaxies as star forming led to no significant changes in the results.

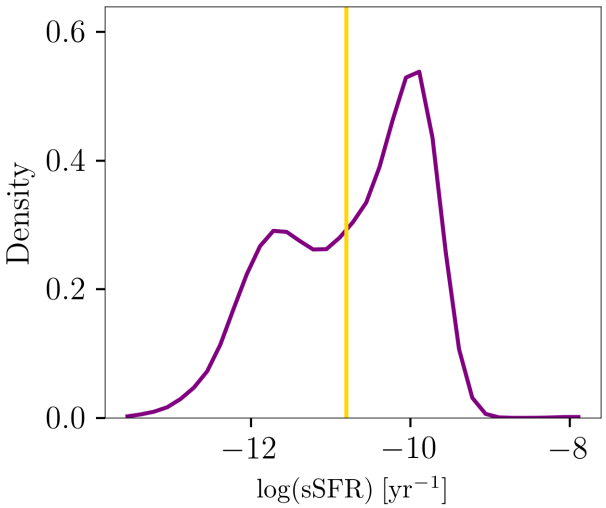

FIGURE 2.6: The sSFR distribution of the 2829 galaxies in the MaNGA sub-sample. Star forming galaxies are defined in this thesis as being to the right of the gold line (sSFR $> 10^{-10.8}$yr^{-1}).

2.1.4 Sample Properties

The sample consists of 1600 galaxies, 871 of which are star forming. Our analysis (2.2) primarily focused on this star-forming sub-sample. The stellar mass and star formation rate distributions of the sub-samples are shown in Figure 2.9. The stellar mass distribution of the $2R_e$ FOV sample does not differ noticeably from the stellar mass distribution of the full MaNGA sample (see Figure 2.1 for comparison), and is relatively flat. However, the stellar mass distribution of the star-forming sub-sample skews towards the low-mass end. There are more low-mass galaxies than high-mass galaxies when only galaxies with sSFR $> 10^{-10.8}$yr^{-1} are selected. Note that the correlation plots in Figures 2.12 and 2.13 (discussed further below) also illustrate the trend of low mass galaxies having higher sSFR than high mass galaxies. This is expected from previous surveys (section 1.1.4), as well as a more recent study of the MaNGA data: Belfiore et al. (2018) also found that low mass galaxies in MaNGA have higher sSFR than high mass galaxies.

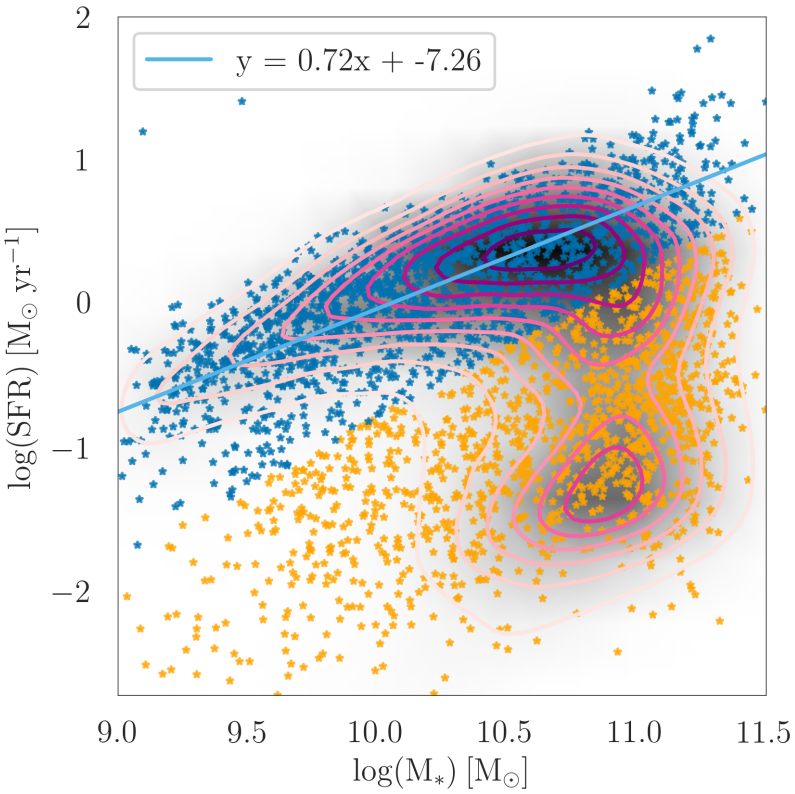

FIGURE 2.7: Star formation rate versus stellar mass for MaNGA galaxies (data obtained from the Pipe3D catalog, Sánchez et al., 2016b). The blue stars are star-forming galaxies, and the orange are non-star-forming. The MaNGA star-forming main sequence line, $y = 0.72x - 7.26$ (light blue line) was obtained from a fit to the MaNGA star-forming sample ($\log(M_{halo}) > 13$, $9.0 < \log(M_*) < 11.5$ [$M_\odot$], sSFR $> 10^{-10.8}[yr^{-1}]$). The background grey scale and pink contour lines are a kernel density estimation (KDE) of the SFR and stellar mass data for a large sample of SDSS galaxies (Salim et al., 2018).

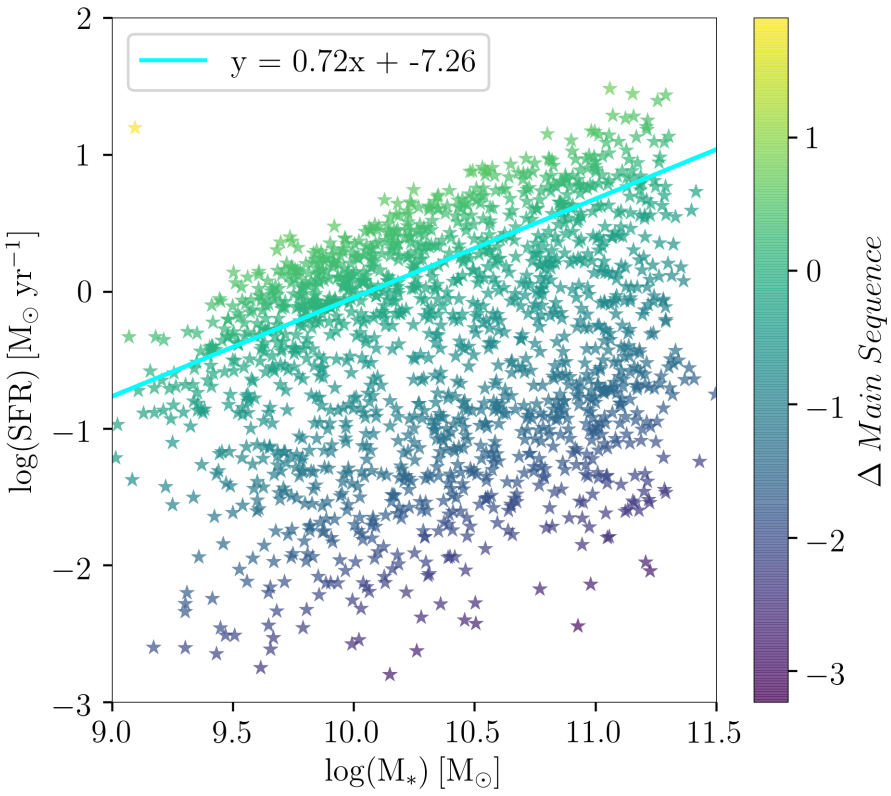

FIGURE 2.8: The SFR vs M_* for the $2R_e$ FOV sample galaxies. The colour of the symbols indicates the distance from the MaNGA main sequence line (ΔMS).

Figure 2.10 shows stellar mass and specific star formation rate distributions, but now illustrating the different distributions in the isolated (n=1) and group (n>2) sub-samples. Of the 1600 $2R_e$ FOV galaxies, 981 are isolated, and 619 are in groups. Of the 871 star-forming galaxies, 671 are isolated and 200 are in groups. The distribution of isolated galaxies tends to skew towards lower mass and higher specific star formation rates than that of the group galaxies, even in the star-forming-only sub-sample. More environment trends in the sample are discussed in section 3.1.

Correlations between pairs of basic properties of the $2R_e$ FOV sample and the star-forming sub-sample are illustrated in Figures 2.12 and 2.13, respectively. The basic properties investigated in these figures include stellar mass, effective radius, and specific star formation rate. Stellar mass and

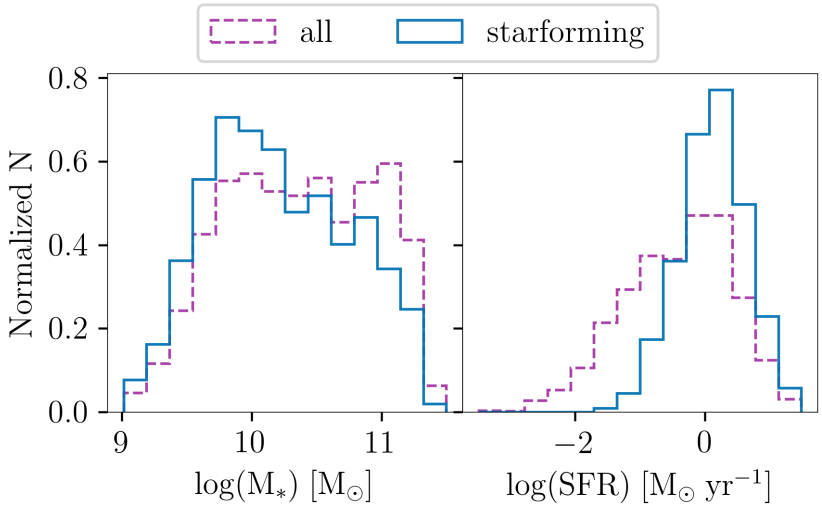

FIGURE 2.9: The stellar mass and star formation rate distribution of the 2Re FOV sample. The 2R_e FOV sub-sample consists of 1600 galaxies, of which 871 are star forming.

effective radius have a strong positive correlation, while stellar mass and sSFR are negatively correlated. However, despite the strong correlation between R_e and M_*, effective radius is only slightly negatively correlated with sSFR. This is expected if star-forming galaxies of a given mass have a more extended disk and thus a larger effective radius than their non-star-forming counterparts of equal mass, which is true in the sample (see Figure 2.11). Note that the correlations between the pairs of properties does not differ significantly between the 2R_e FOV sample and the star-forming sub-sample.

The correlations between the basic properties and redshift are also shown in Figures 2.12 and 2.13 in order to probe how the MaNGA selection criteria affects the distributions of sample properties. As a result of the survey design, galaxies of higher redshift have larger effective radii and thus larger stellar mass, and we can see that there are positive correlations between redshift and M_*, R_e in Figure 2.12. The survey was designed to ensure the galaxy face fills the IFU and is not too small or too large inside the IFU frame, while also aiming for an even distribution in galaxy mass. For a given IFU size (i.e. a given angular size on the sky), the IFU will cover a

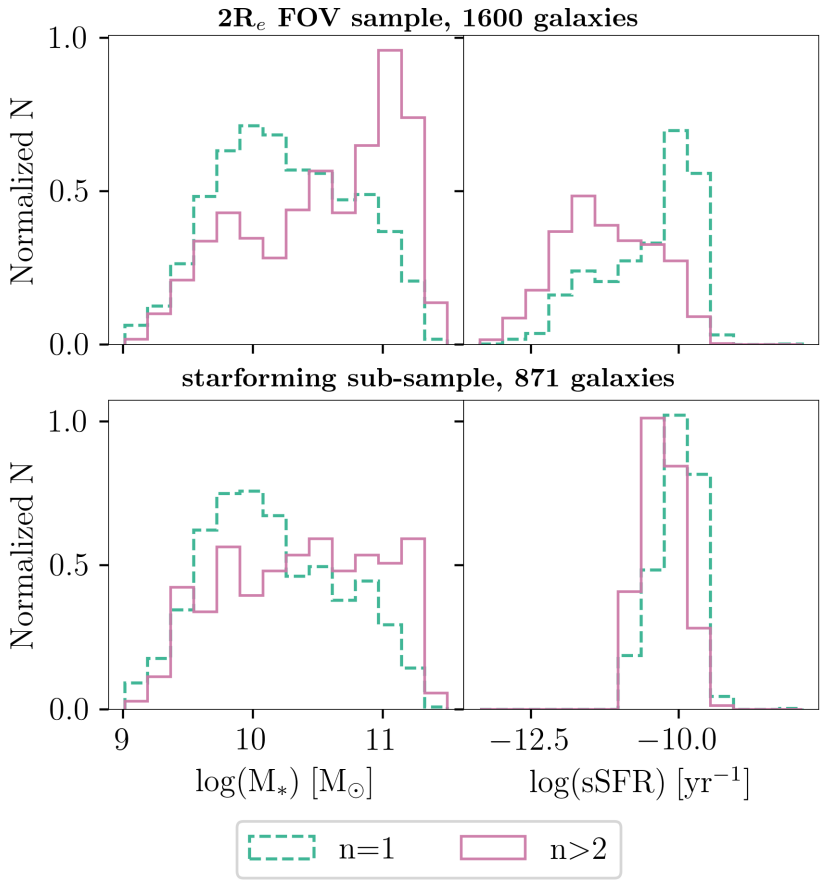

FIGURE 2.10: The stellar mass and sSFR distribution of the 2Re FOV sample, in two environment bins. In the isolated (n=1) sample, there are more low-mass stellar mass and higher sSFR galaxies than in the group (n>2) sample, even when selecting star-forming-only galaxies.

larger physical galaxy size at higher redshift. Therefore, it was necessary to go to higher redshift in order to target larger, higher mass galaxies while not overflowing the IFU frame (Wake et al., 2017). Note that while it has been shown that the mean specific star formation rate increases with redshift (Madau and Dickinson, 2014), we do not see this correlation due to the small redshift range of our sub-sample.

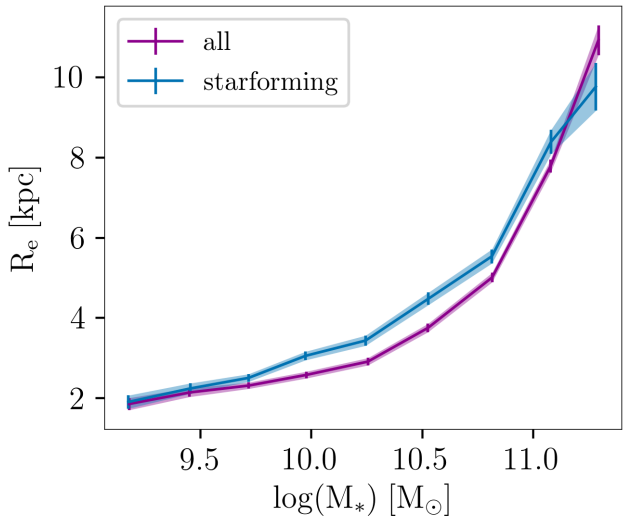

FIGURE 2.11: The effective radius versus stellar mass of galaxies in the $2R_e$ sample compared to the star-forming sub-sample, with standard error shown.

AGN Galaxies

All MaNGA galaxies were classified on the Baldwin et al. (1981) emission line diagrams (see section 1.1.6), using the classification scheme of Kewley et al. (2006). Line ratios were obtained from the Pipe3d catalog, which provides emission line ratios within the central 2.5 arcsecond aperture for each galaxy (Sánchez et al., 2016b). Two systems were used: one which compares the OIII/Hβ to NII/Hα line ratios (the NII diagram), and another which compares the OIII/Hβ to SII/Hα (the SII diagram). These two diagrams are shown in Figure 2.14. Galaxies were classified as AGN, composite AGN-starburst, or star-forming based on these diagrams. Galaxies are unclassifiable if they do not contain all four lines with sufficient signal (S/N $\gtrsim$ 3; Sánchez et al., 2016b).

Figure 2.15 shows how the two classification schemes used on the MaNGA sample compare to one another and to that of SDSS Data Release 8 (DR8) using the Max Planck for Astrophysics and Johns Hopkins University (MPA-JHU) spectroscopic parameters pipeline (the methods they

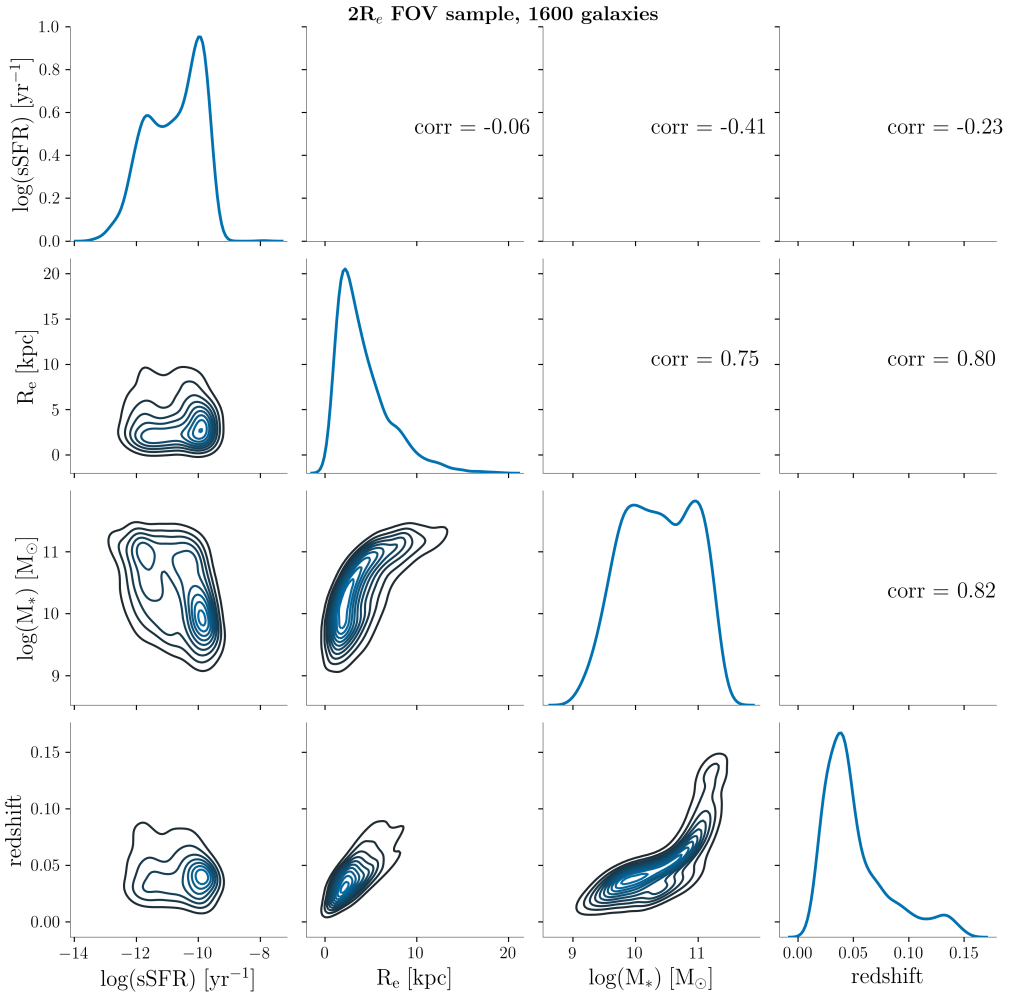

FIGURE 2.12: Correlation grid of properties of galaxies in the 2R$_e$ FOV sample. Properties shown include effective radius, stellar mass, and specific star formation rate, as well as galaxy redshift. Below the diagonal are the 2-D density distributions, while along the diagonal are the 1-D distributions. Above the diagonal are the Spearman's rank correlation coefficients, which assesses how well the relationship between the two parameters can be described by a monotonic function.

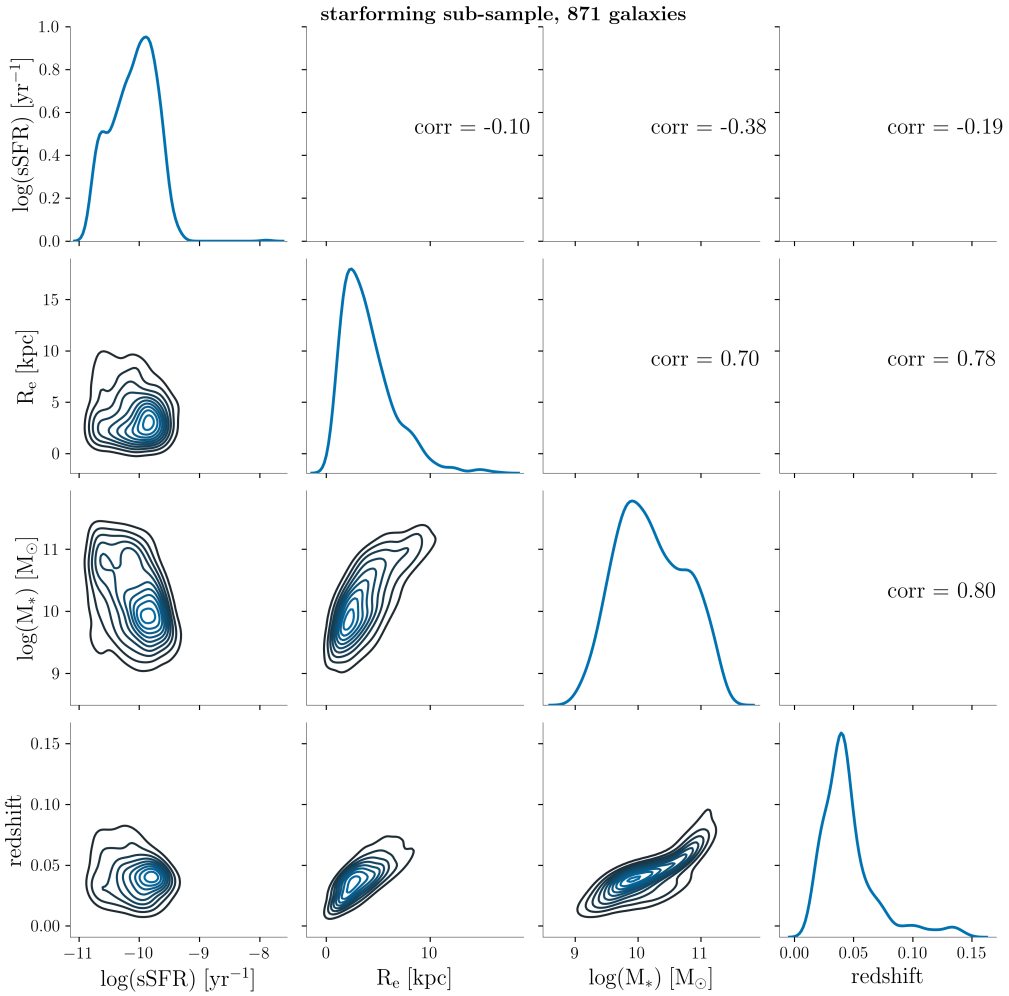

FIGURE 2.13: Correlation grid of properties of galaxies in the $2R_e$ FOV, star-forming sub-sample. Properties shown include effective radius, stellar mass, and specific star formation rate, as well as galaxy redshift. Below the diagonal are the 2-D density distributions, while along the diagonal are the 1-D distributions. Above the diagonal are the Spearman's rank correlation coefficients, which assesses how well the relationship between the two parameters can be described by a monotonic function.

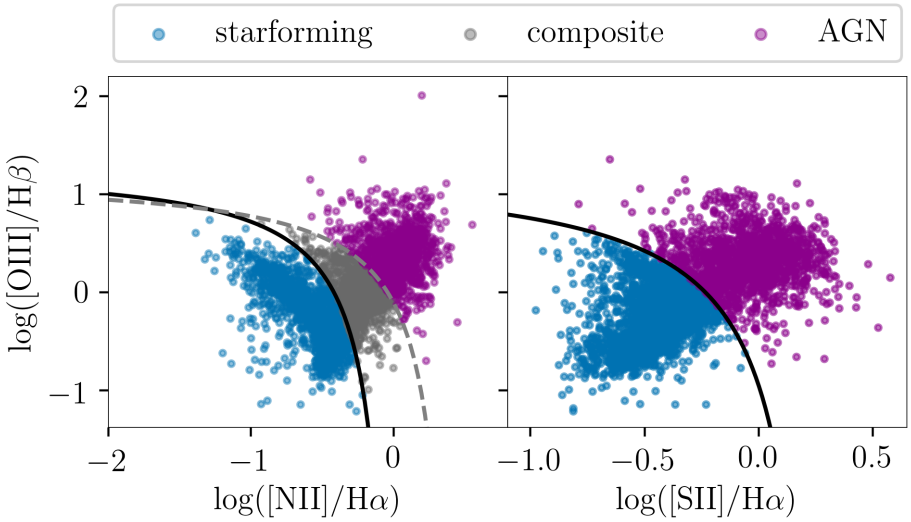

FIGURE 2.14: The Kewley et al. (2006) NII (left) and SII (right) BPT Diagrams for MaNGA. Objects lying below the solid-black line are classified as star-forming in both phase-space diagrams, and are shown in blue. On the NII diagram, objects lying between the black and dashed-lines are composite (grey) and above the grey-dashed line are AGN (purple). On the SII diagram, objects lying above the black line are AGN (shown in purple).

used are described in Brinchmann et al., 2004). The NII and SII classification schemes show similar distributions of star-forming and AGN galaxies; however, the NII scheme defines a composite region that is not present on the SII diagram. Galaxies classified as composite in the NII diagram are therefore distributed into the star-forming or AGN bins on the SII plot.

Instead of removing AGN galaxies from the main sample, spaxels for galaxies within our sample were classified, and AGN spaxels removed (see 2.2.1). However, this global classification was used as a check on our results. We repeated our measurements on the sample with all AGN galaxies removed (the entire galaxy, not just the AGN spaxels), and found no significant changes in results (see Appendix A).

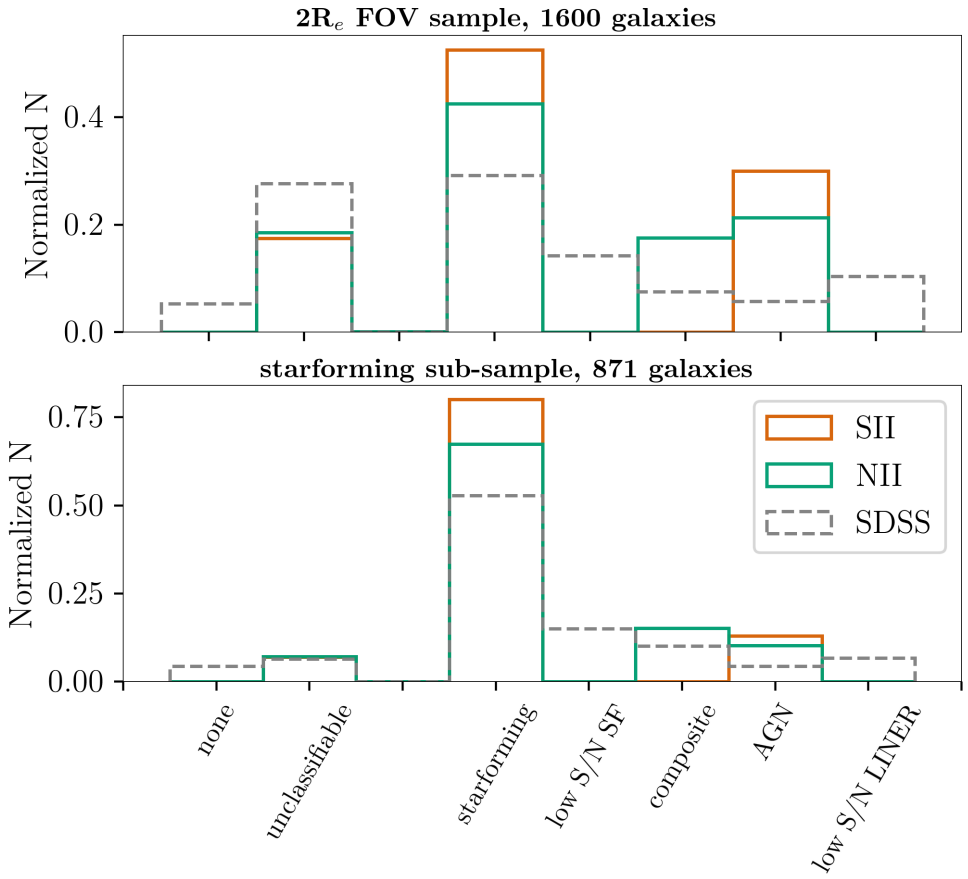

FIGURE 2.15: Histograms comparing the NII, SII, and SDSS BPT emission-line classification of MaNGA galaxies in the 2R$_e$ sample and the star-forming sub-sample. The SII and NII schemes in general show good agreement in galaxies classified as star-forming or AGN, however, galaxies classified as composite in the NII diagram are distributed into the star-forming or AGN bins in the SII diagram. The SDSS classification includes two other categories not present in the NII or SII diagrams: low S/N star-forming, and low S/N Low Ionization Narrow Emission-line Regions (LINER).

2.2 Analysis

2.2.1 The Star-forming Hα Maps

The star-forming region of each galaxy was determined through analysis of the Hα emission line equivalent width (EW) maps. As discussed in section 1.1.5, Hα emission is an indicator of active star formation. Equivalent width is a convenient and accurate way to measure the overall strength of the emission line, since it takes into account variations in the shape, such as broadening of the line (Carroll and Ostlie, 2007). The Hα EW maps are provided by the data analysis pipeline (DAP) (see section 2.1.1 as well as Westfall et al., 2019), and were retrieved through the Marvin Python package of Tools (Cherinka et al., 2019). The DAP creates detailed masks of each spectrum. Any spectra flagged DONOTUSE by the data reduction pipeline (Law et al., 2016a) – for example, due to a foreground-star, detector artifacts, or broken fibers – were masked and not included in analysis. The DAP also masks any spectrum with a g-band signal-to-noise S/N$_g$ < 1. We further applied a spaxel mask to negative Hα EW values, as well as any spaxels with Hα S/N < 3. Masked spaxels are either not included in the calculation, or treated as zero (see 2.2).

Using Marvin, a BPT (Baldwin et al., 1981) diagram was generated for each spaxel of each galaxy in order to classify the emission. Marvin makes use of the Kewley et al. (2006) classification system to return classification masks. We use a strict classification criteria to mask AGN spaxels: in order for a spaxel to be classified as AGN, it must be classified as AGN according to the three diagnostic criteria of Kewley et al. (2006) (NII, SII, and OI), and must therefore have S/N > 3 in all 6 lines (NII, SII, OI, Hα, OII and Hβ). Spaxels identified as AGN based on these criteria were masked.

Finally, to maintain consistency across the sample, any data outside of 2R$_e$ was masked. Figure 2.16 shows examples of the final star forming Hα EW maps for a few galaxies in our star-forming sample alongside the SDSS image and the Petrosian elliptical coordinate maps.

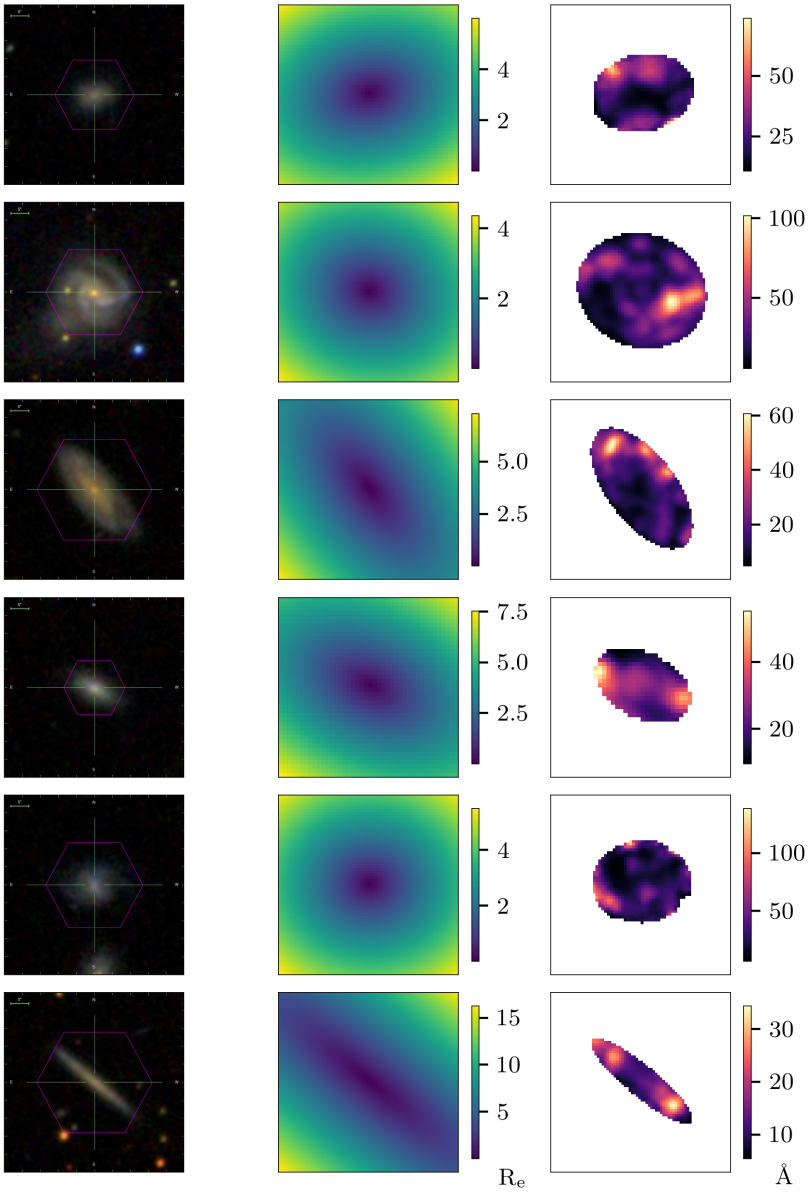

FIGURE 2.16: Example SDSS Images (left), elliptical coordinate maps (middle), and masked Hα EW maps (right) for 6 galaxies from the star-forming sub-sample. Each row corresponds to one galaxy. Note that we mask Hα data outside of $2R_e$ to maintain consistency across the sample.

2.2.2 Hα Map Parameters

The spatial distribution of the Hα emission was characterized by four main measurements: the first moment, the asymmetry index, the half-light radius, and the concentration. The methods for obtaining each of these parameters are described in this section.

First Moment of Hα

The first moment of Hα was determined for each galaxy by taking the mean elliptical coordinate of the Petrosian elliptical coordinate map, where each spaxel R_e value in the mean is weighted by the corresponding H-α EW values. The Hα first moment of a galaxy with n spaxels within $2R_e$ was therefore computed as:

$$first\ moment = \frac{\sum_{i=1}^{n} r_i f_i}{\sum_{i=1}^{n} f_i}$$

where r is the elliptical coordinate of the spaxel, and f is the Hα EW measurement for that spaxel. Masked data are weighted as zero and not counted towards the mean.

Asymmetry

The asymmetry of each galaxy was calculated using the formula from Conselice et al. (2000):

$$A_{abs} = \frac{\Sigma|I_o - I_\phi|}{2\Sigma|I_o|} \tag{2.1}$$

where I_o is the intensity distribution of the original Hα map, and I_ϕ is the intensity distribution of the map rotated by 180° about the optical centre of the galaxy. An example of the original masked map, the rotated map, and the residual map are shown in Figure 2.17.

Half-light Radius

The Hα EW half-light was determined for each galaxy by summing up the EW values in all spaxels to get the total EW, then determining the

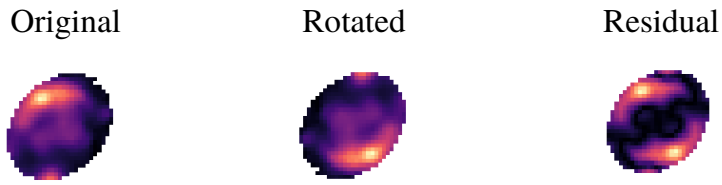

FIGURE 2.17: Example of maps used in asymmetry measure: original (I_i), rotated (I_ϕ) and residual ($|I_o - I_\phi|$) maps for a galaxy used in the sample, IFU plate 8483-6103.

location, in R_e, within which half of the total EW is contained. Masked spaxels (recall that this includes spaxels outside of $2R_e$) are not included in the sum. The profiles in Figure 2.18 illustrate how the half-light value was obtained for each galaxy: the Hα was summed in each annulus, then the cumulative Hα at each radial value was determined, and the radius whose cumulative value corresponded to half of the total Hα within $2R_e$ was identified as the half-light radius.

Concentration

The concentration was defined as $C = R_{80}/R_{20}$ (as in Conselice, 2003), where R_{80} is the radius within which 80% of the Hα EW is contained, and R_{20} is the radius containing 20%. The R_{80} and R_{20} are shown as green and orange vertical lines respectively on the cumulative profile in Figure 2.18.

2.2.3 Hα EW Profiles

We created radial profiles to explore how Hα EW as a function of galactic radius (R_e) differs in different environments. The radial profile of each galaxy's star forming Hα emission was determined by calculating the median Hα EW value in each annulus of width 0.15 R_e. A couple of example radial profiles are given in Figure 2.19. Stacked radial profiles were then created by taking the median profile of all of the galaxies in each stellar

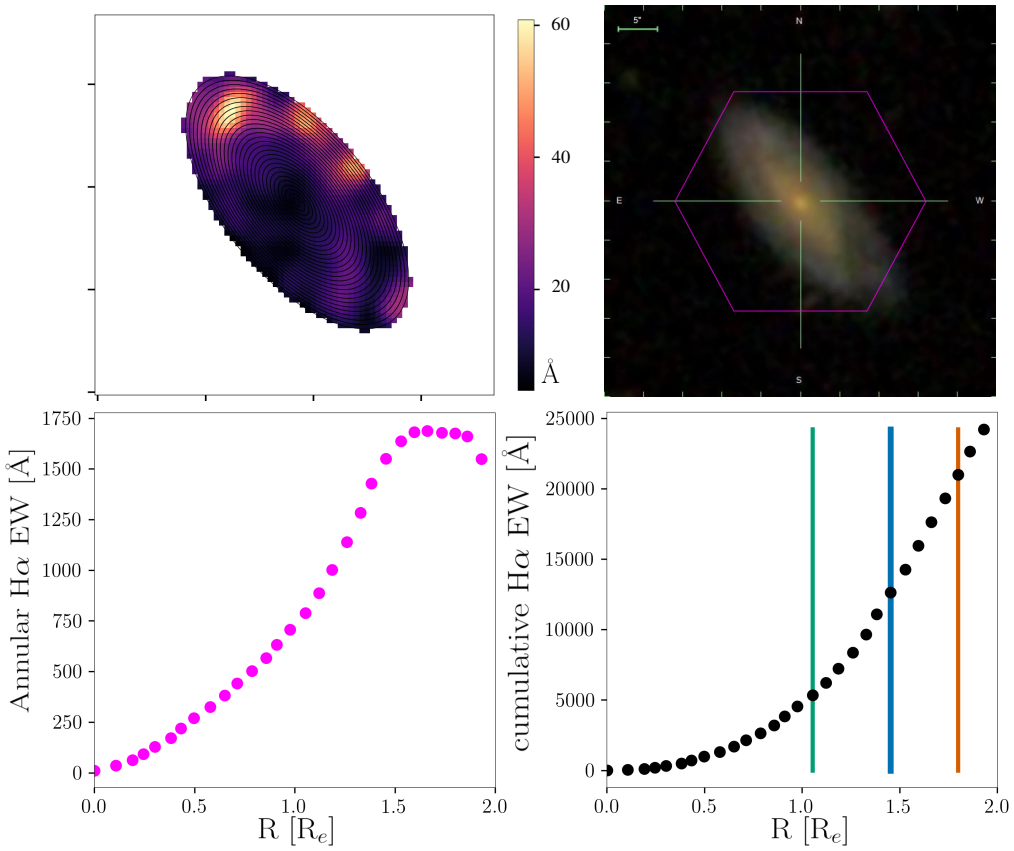

FIGURE 2.18: Top: Hα EW map for IFU plate 7443-12705 and associated SDSS image. The map shows annuli within which Hα EW was summed as black elliptical rings. Bottom: The corresponding annular sum profile (left) and cummulative profile (right), with the radii containing 20%, 50% and 80% of the Hα identified with green, blue, and orange lines, respectively.

mass bin. This was done by finding the median Hα EW value at each radius of all of the galaxies in each bin.

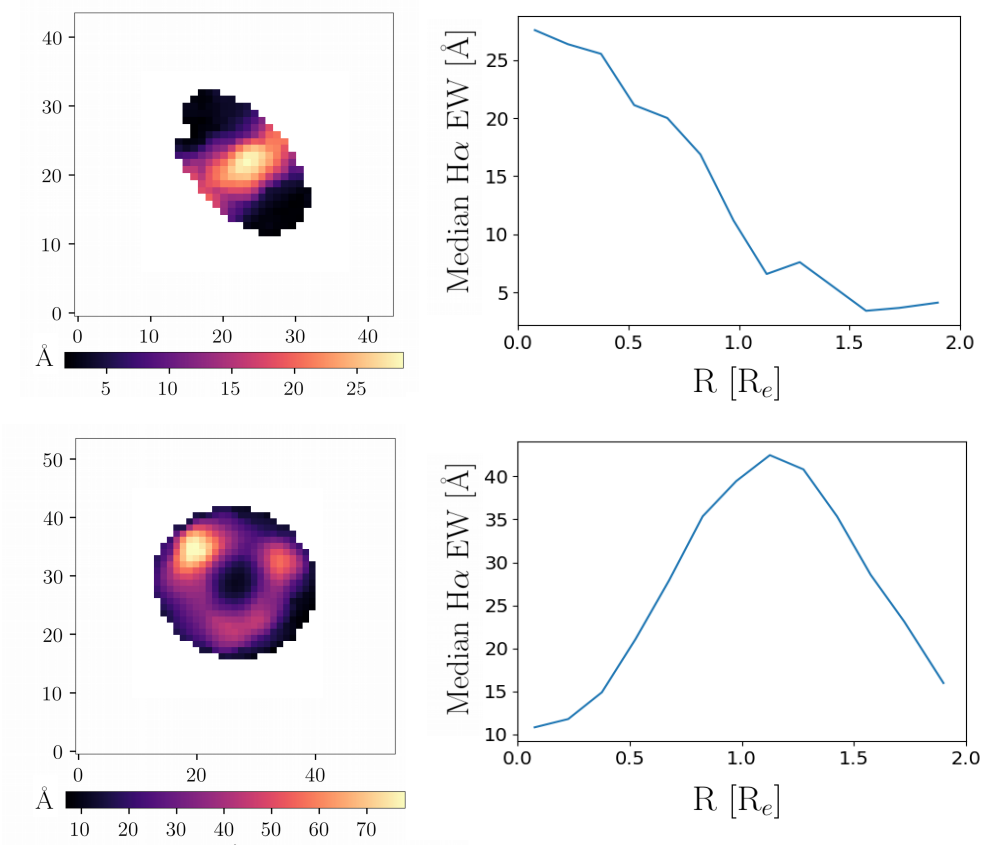

FIGURE 2.19: The Hα EW maps and associated radial profiles are shown for two galaxies in the sample (plateifus 8322-3704 and 8322-6102). The profiles were obtained by finding the median value in each annulus of width 0.15 R$_e$.

Masked values are treated in two ways when creating the profiles. The first way is by leaving the values as masked in the map, which means they are not counted toward the median when creating individual profiles. When creating the stacked profiles, if a particular annulus of a particular galaxy is missing a median Hα value (due to all data in that annulus being masked), then that galaxy is not counted toward the stacked median for that annulus, but may still be counted toward the stacked median in other annuli where that galaxy does have data. The second way is to include all of the

masked values as zeros in each galaxy. An annulus which normally would have resulted in a missing value due to masked spaxels in that annulus would now have a median of zero. Thus, all galaxies have complete profiles and every annulus is counted towards the stacked profiles. In Chapter 3, we present stacked profiles where missing data were treated as zeros and counted towards the median. However, not counting missing values towards the median did not have a significant effect on the stacked profiles.

2.2.4 Environment Measures

Two main measures were used to probe the environmental dependence of Hα distribution: halo mass and halo-centric distance. Halo masses were obtained from the group catalogs of Lim et al. (2017) and Yang et al. (2007). These catalogs also provide the group centre in right ascension (RA), declination (DEC), and redshift (z) coordinates. The offset between the group centre and each galaxy in the group was computed. This halo-centric distance value was then normalized by the halo-radius, r_{180}, which is defined as the radius of the halo within which the mean mass density is 180 times the mean density of the Universe at the given redshift (Yang et al., 2007). Halo radii were computed using equation (5) from Yang et al. (2007):

$$r_{180} = 1.26\ h^{-1}\text{Mpc}\left(\frac{M_h}{10^{14}\ h^{-1}\ \text{M}_\odot}\right)^{1/3}(1+z_{group})^{-1} \tag{2.2}$$

The distribution of galaxies based on halo mass and halo centric distance are shown in Figure 2.20. Of note is that there are fewer star-forming galaxies nearer the cluster centre in the sample, which is expected if star formation is quenched in higher environment densities (see section 1.3.2). It is interesting that the distribution of halo masses for the whole sample is similar to that of the star-forming sub-sample.

We also classify galaxies as backsplash, virialized, or infalling. Virialized galaxies are galaxies that live within the virial radius of the group. Infalling

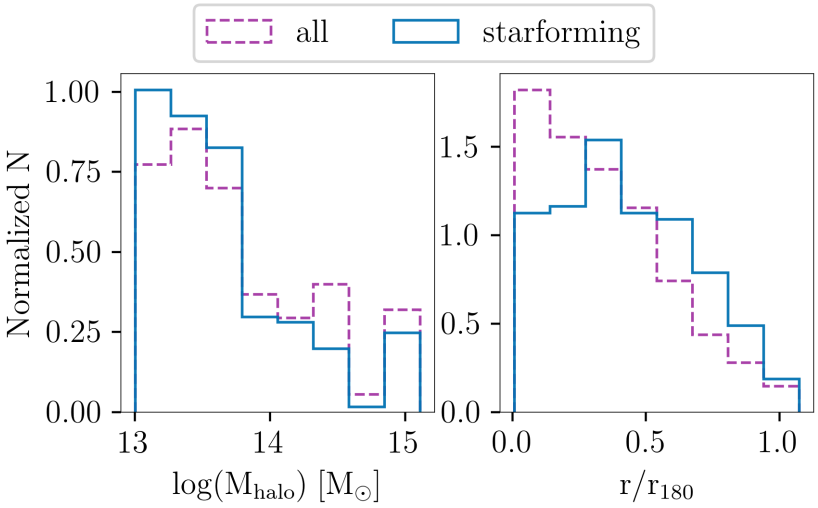

FIGURE 2.20: Histograms showing the distribution of halo masses (left) and halo-centric distance (right) for the whole $2R_e$ FOV sample (purple dashed lines) and the star-forming sub-sample (blue solid line).

galaxies are also within the projected virial radius, but have a higher velocity as would be expected if they were falling into the group (Oman et al., 2013) . Backsplash galaxies are satellite galaxies that were once inside the virial radius of the host halo, but now live beyond it (Gill et al., 2005). Galaxies were categorised as virialized, infalling, or backsplash based on where they live in $|\Delta cz|/\sigma$ phase space, using regions outlined in Mahajan et al. (2011) (see Figure 2.21). The radial velocity ($|\Delta cz|$) is computed by multiplying the speed of light (c) by the redshift offset between the galaxy and the group centre (Δz). The line-of-sight velocity dispersions of the galaxy groups (σ) were calculated using equation (6) of Yang et al. (2007):

$$\sigma = 397.9 \text{ km s}^{-1} \left(\frac{M_h}{10^{14}\ h^{-1}\ \text{M}_\odot} \right)^{0.3214} \tag{2.3}$$

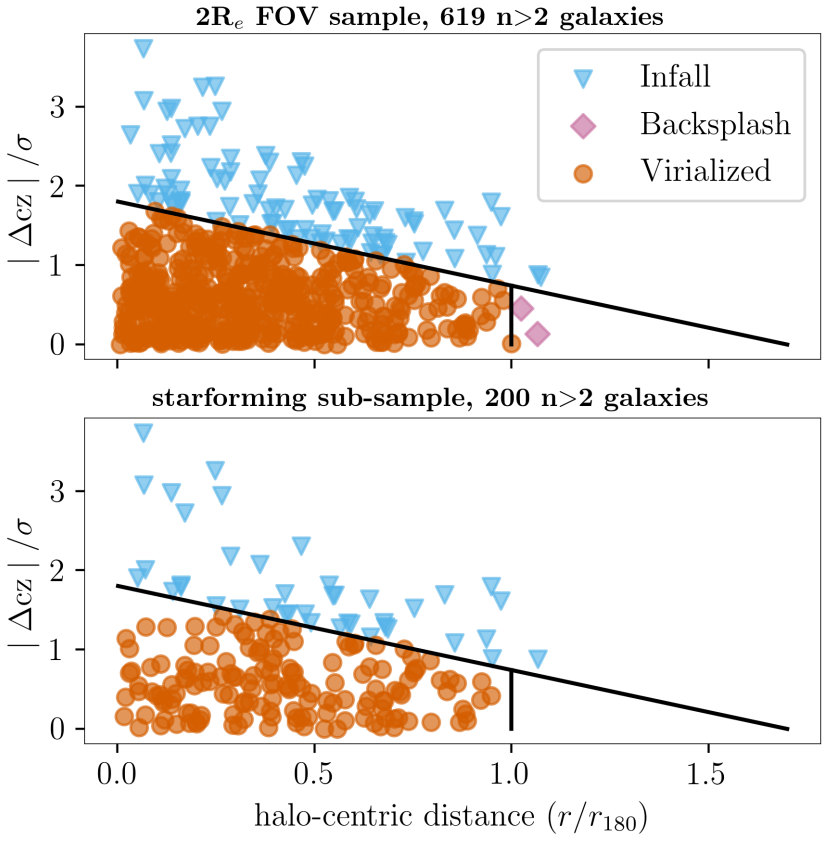

FIGURE 2.21: Galaxies are identified as infalling (blue), backsplash (pink) and virialized (orange) based on their positions in $|\Delta cz|/\sigma$ vs. r/r_{180} phase space. The three different regions are adapted from Mahajan et al. (2011). The top plot contains all of the group galaxies in the 2R$_e$ FOV sample, and the bottom plot contains only galaxies in the star-forming sub-sample.

Chapter 3

Results

This chapter presents results of our analysis of resolved Hα disk properties in different environments. It is divided into two sections. In section 3.1, we present the dependence of integrated properties on environment, since it is important to understand the resolved Hα trends in relation to well-studied integrated property trends. Section 3.2 then presents the results of our study of the environmental dependence of Hα disk properties in the MaNGA star-forming sub-sample. Section 3.2 is divided into sub-sections based on the three environment indicators investigated: halo mass, halo-centric distance, and whether the galaxy is infalling or virialized.

3.1 Integrated Sample Properties: Trends with Environment

This section looks at the dependence of integrated stellar mass, effective radius and specific star formation rate on environment for galaxies in our sample. As described in 2.1.3, our sample includes all galaxies mapped out to at least $2R_e$. Figure 3.1 plots the mean effective radii and stellar mass of the sample galaxies against halo mass and halo-centric distance. Note that effective radius and stellar mass are correlated (see also Figure 2.11). The high mass halos are groups that have higher galaxy membership, and we can see in this figure that on average there are more lower mass galaxies in groups with higher halo mass (or higher group membership) than in groups

with lower halo mass, and that this trend is stronger for the star-forming sub-sample. Figure 3.1 also shows that galaxy stellar mass decreases with halo-centric distance, with no significant difference between the full sample and star-forming sub-sample. The mass segregation exhibited in the sample helps explain the stellar mass trend with halo mass. We can also see from Figure 3.1 that on average, isolated (n=1) galaxies have lower stellar mass and smaller effective radii than galaxies in groups and clusters.

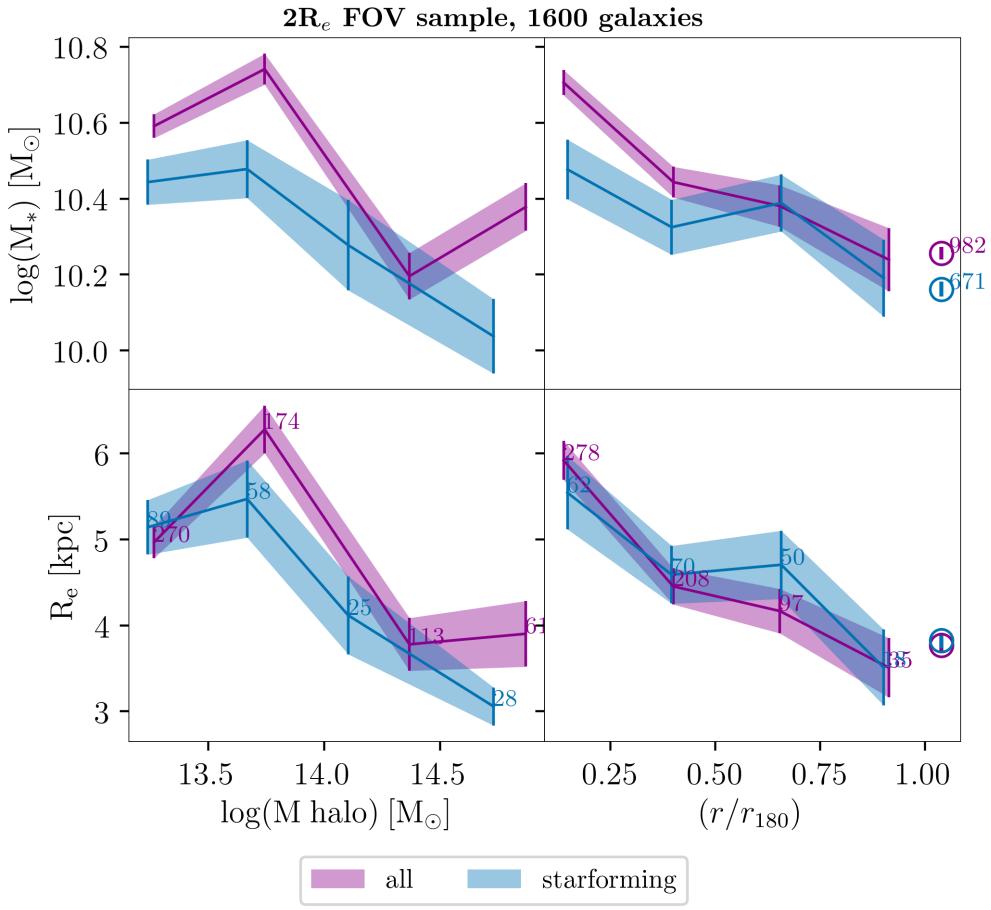

FIGURE 3.1: The mean stellar mass (top row) and effective radii (bottom) of galaxies is plotted against halo mass (left) and halo-centric distance (right) for galaxies in the 2R$_e$ sample (purple) and the star-forming sub-sample (blue). The isolated galaxy bins are plotted as open circles in the right hand side. Data points are labelled with the number of galaxies in each bin. The standard error is shown as vertical bars.

Figures 3.2 and 3.3 further investigate the integrated properties of our

sample with halo-mass and halo-centric distance using continuous probability density curves of the binned data. Kernel density estimate (KDE) distributions of stellar mass, R_e, and now log(sSFR), are plotted in bins of halo mass, halo-centric distance, and whether the galaxy is virialized or infalling. Galaxies are divided into bins based on whether they are isolated (n=1) or in a group (n>2). We further divide the group galaxies based on environmental properties. Galaxies are put into two bins of halo mass of roughly equal size: $M_{halo} < 10^{13.5} M_\odot$ or $M_{halo} > 10^{13.5} M_\odot$. We also divide galaxies into two bins of halo-centric distance, those that live in the inner halo ($r/r_{180}<0.5$), and those that live in the outer halo ($r/r_{180}>0.5$). Finally, galaxies are categorized as infalling or virialized based on their position in phase-space, as described in section 2.2.4. Note that there were not enough galaxies classified as backsplash to include this category in the analysis.

Figure 3.2 investigates the full sub-sample, while Figure 3.3 focuses on the star-forming sub-sample. The left-most column in both figures shows the stellar mass KDE distributions of galaxies in different environments. It is evident that isolated galaxies tend to have lower stellar mass, with a peak in number distribution at about $10^{10} M_\odot$ in the full sample and $10^{9.9} M_\odot$ in the star-forming sub-sample. We can see in Figure 3.2 that although there are slightly more low-mass galaxies in the high mass halos (as seen in Figure 3.1), the stellar mass distribution peaks at a slightly higher stellar mass for high-mass halos than for low-mass halos, as expected - however, these very high mass galaxies are not present in the starforming sample, as seen in Figure 3.3.

There is a peak in stellar mass number density at $\sim 10^{11} M_\odot$ for galaxies in the inner-cluster bin ($r/r_{cluster} < 0.5$) and in the virialized bin in the full sample. These trends are also present in the star-forming sub-sample, however, the peak in high stellar mass in the inner part of the halo is less significant in the star-forming sub-sample. These higher-mass galaxies are more likely to be virialized and live nearer the centre of the halo, and are less likely to be part of the star-forming sub-sample.

The right-most column of Figures 3.2 and 3.3 show the KDE distributions of the specific star forming rates of the full sample and the star-forming sub-sample, respectively. Both figures show that group galaxies near the centre of the halo tend to have lower star-formation rates. In the full sample (Figure 3.2), we see that virialized galaxies have lower star formation rates than infalling galaxies. Isolated galaxies have the highest star formation rates, as expected.

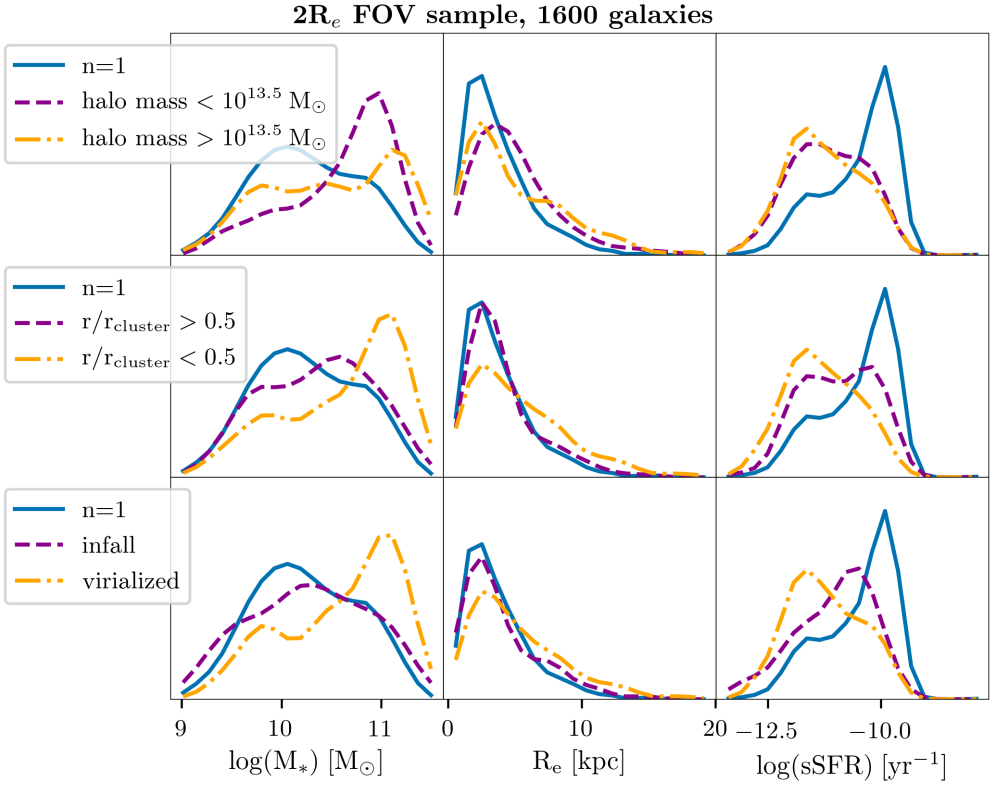

FIGURE 3.2: Kernel density estimate (KDE) distributions of total M_* (left), R_e (middle), and log(sSFR) (right) are plotted for galaxies in the sample, where galaxies are divided into bins based on environment. The bin of isolated galaxies is shown in blue in each plot. In the top row, the low mass halo ($M_{halo} < 10^{13.5} M_\odot$) bin is purple, while the high mass halo ($M_{halo} > 10^{13.5} M_\odot$) bin is yellow. In the middle row, the outer cluster ($r/r_{180} > 0.5$) bin is shown in purple, and the inner cluster ($r/r_{180} < 0.5$) bin in yellow; in the bottom row, the bin of infalling galaxies is in purple, and virialized, yellow.

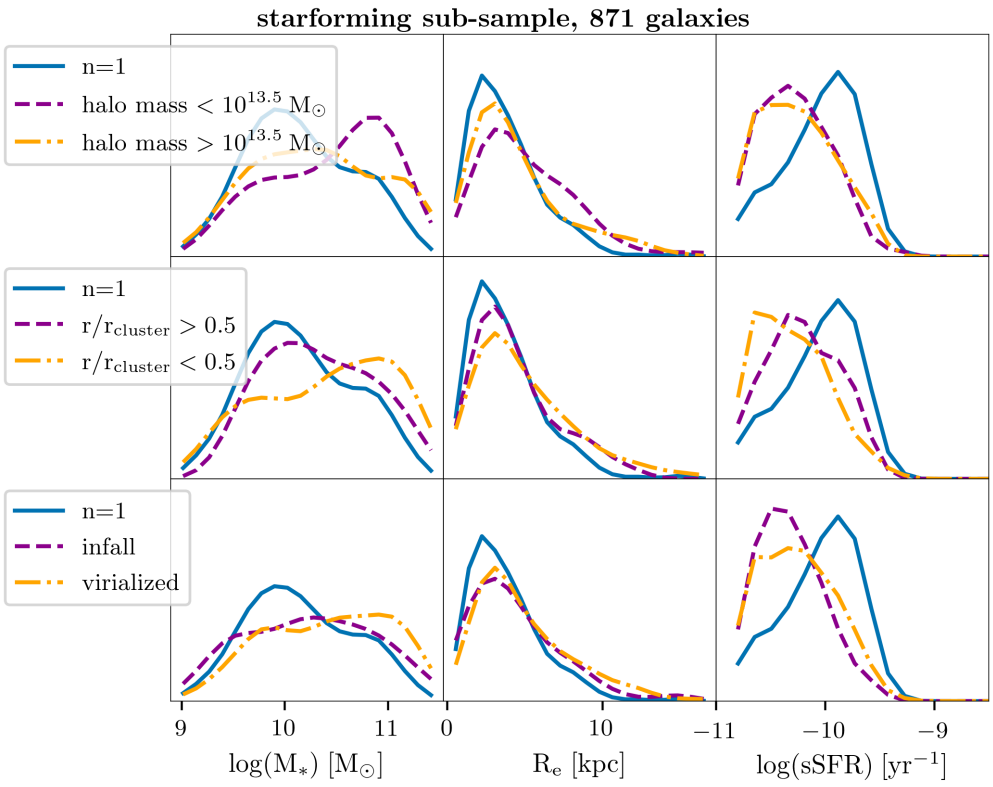

FIGURE 3.3: Kernel density estimate (KDE) distributions of total M_* (left), R_e (middle), and log(sSFR) (right) are plotted for galaxies in the star-forming sub-sample, where galaxies are divided into bins based on environment. The bin of isolated galaxies is shown in blue in each plot. In the top row, the low mass halo ($M_{halo} < 10^{13.5} M_\odot$) bin is purple, while the high mass halo ($M_{halo} > 10^{13.5} M_\odot$) bin is yellow. In the middle row, the outer cluster ($r/r_{180} > 0.5$) bin is shown in purple, and the inner cluster ($r/r_{180} < 0.5$) bin in yellow; in the bottom row, the bin of infalling galaxies is in purple, and virialized, yellow. Note: the range in the right panels (log(sSFR)) differs from Figure 3.2.

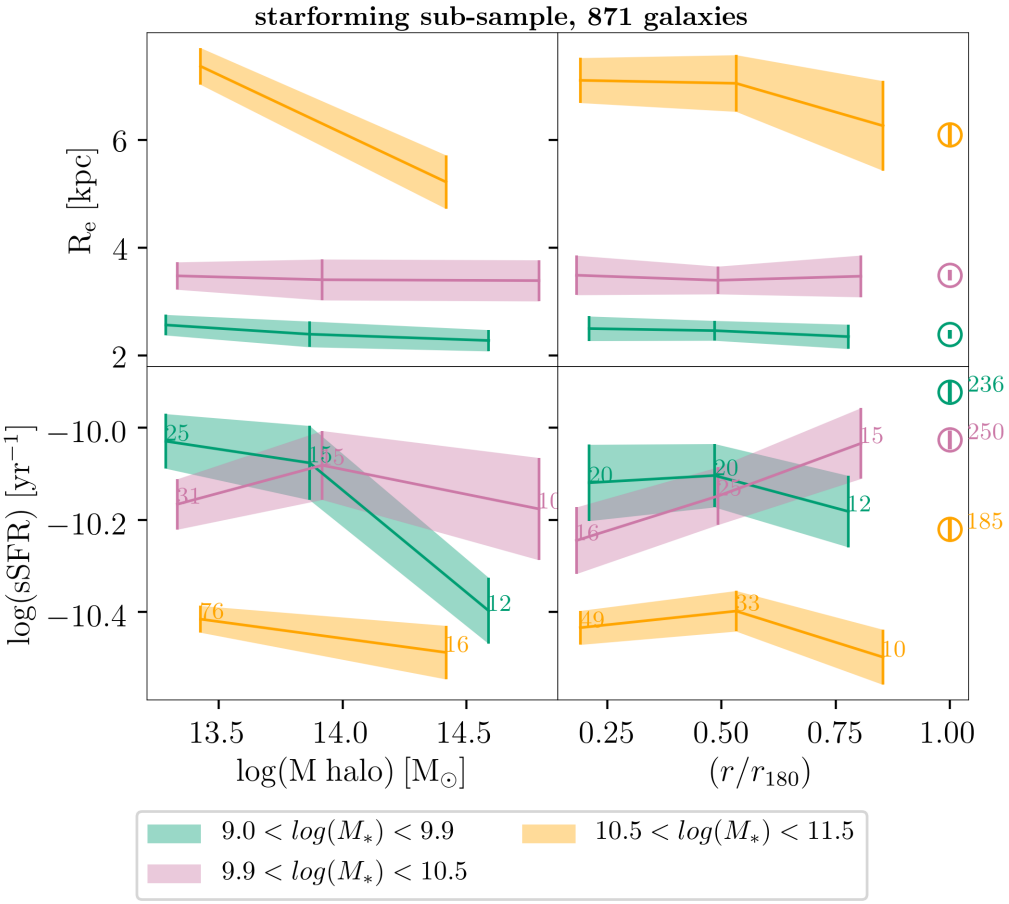

FIGURE 3.4: The log(sSFR) (bottom row) and R_e (top row) are plotted against halo mass ($\log(M_{halo})$, left) and halo-centric distance (r/r_{180}, right) for group galaxies in the star-forming sub-sample, with isolated galaxy bins shown as open circles on the right hand side of each row. Galaxies are divided into three bins of stellar mass: $9.0<\log(M_*)<9.9$ $M_\odot$ (green), $9.9<\log(M_*)<10.5$ $M_\odot$ (pink), and $10.5<\log(M_*)<11.5$ $M_\odot$ (yellow). The points in the bottom row are labelled with the number of galaxies in each bin, and standard error is given as vertical bars.

The middle columns of Figures 3.2 and 3.3 show that isolated galaxies tend to have a slightly smaller effective radius, with the peak in distribution slightly offset to lower effective radii for isolated galaxies in both the full sample and the star-forming sub-sample. However, in general there is no significant difference in effective radius between the different environments. This is confirmed in Figure 3.4, where we can see that for galaxies in the star-forming sub-sample, the R_e of low mass ($9.0 < log(M_*) < 9.9\ M_\odot$) and mid-mass ($9.9 < log(M_*) < 10.5\ M_\odot$) galaxies does not change with halo mass or halo-centric distance. In the high-mass bin, the R_e of galaxies in higher mass halos is slightly smaller than galaxies in lower mass halos, in keeping with the trend illustrated in Figure 3.1. The isolated galaxy bins are plotted as open circles in Figure 3.4; we can see that there is no significant difference in effective radius between the isolated and group galaxies.

In Figure 3.4 we can also see some trends in global sSFR with environment when galaxies are binned by stellar mass. In this and subsequent plots that bin by stellar mass, galaxies in the star-forming sub-sample are divided into three bins of equal size: $9.0 < \log(M_*)[M_\odot] < 9.9$, $9.9 < \log(M_*)[M_\odot] < 10.5$, and $10.5 < \log(M_*)[M_\odot] < 11.5$. Figure 3.4 shows that isolated star-forming galaxies overall have higher sSFR than galaxies in groups. Looking within the group environment, the low-mass galaxies tend to have lower sSFR in higher mass halos, but show no significant difference in sSFR with halo-centric distance. Meanwhile, the mid-mass galaxies have lower sSFR nearer the centre of the group halos, but have no significant trends in sSFR with halo mass. There are no significant trends in sSFR with halo mass or halo-centric distance for the high-mass galaxies.

3.2 Resolved Hα Disks: Trends with Environment

This section presents the results of our analysis of how the spatial properties of Hα disks of star-forming galaxies depend on environment.

3.2.1 Hα EW Profiles

Median Hα EW radial profiles for the star-forming sub-sample are shown in Figure 3.5. The profiles are binned based on stellar mass and environment. The profiles illustrate that Hα EW is suppressed across the entire face of galaxies in groups and clusters compared to field (n=1) galaxies. This is true for galaxies of all stellar masses. Removing AGN galaxies from the sample does not change this key result (see Appendix A1.1)

In the second row of Figure 3.5, galaxies are divided into two groups: those in the outer halo ($r/r_{180} > 0.5$) and those in the inner halo ($r/r_{180} < 0.5$). Low mass star-forming galaxies ($9.0<M_*<9.9$ $M_\odot$) tend to have more suppressed Hα EW at larger galactic radii in the inner halo compared to those in the outer halo. Mid-mass ($9.9<M_*<10.5$ $M_\odot$) and high mass ($10.5<M_*<11.4$ $M_\odot$) galaxies show a slight suppression of Hα at all galactic radii in the inner halo compared to the outer halo. When removing AGN from the sample, however, there is no suppression of Hα EW in high stellar mass galaxies in the inner compared to the outer halo (see Appendix A). This indicates that AGN may be responsible for the global suppression of Hα in the high stellar mass galaxies seen in Figure 3.5.

The third row of Figure 3.5 presents the profiles of group star-forming galaxies, now divided into those that live in high-mass halo environments ($M_{halo} > 10^{13.5} M_\odot$) and those that live in low-mass halos ($M_{halo} > 10^{13.5} M_\odot$). The low stellar mass galaxies living in high mass halos show a slight suppression in Hα at larger galactic radii compared to those living in low mass halos. There is no significant difference in the shape of the profiles for mid-mass galaxies in high mass halos compared to mid-mass galaxies in low mass halos. Interestingly, when removing AGN from the sample, mid-mass galaxies living in high mass halos have enhanced Hα EW compared to mid-mass galaxies living in low mass halos (see Appendix A).

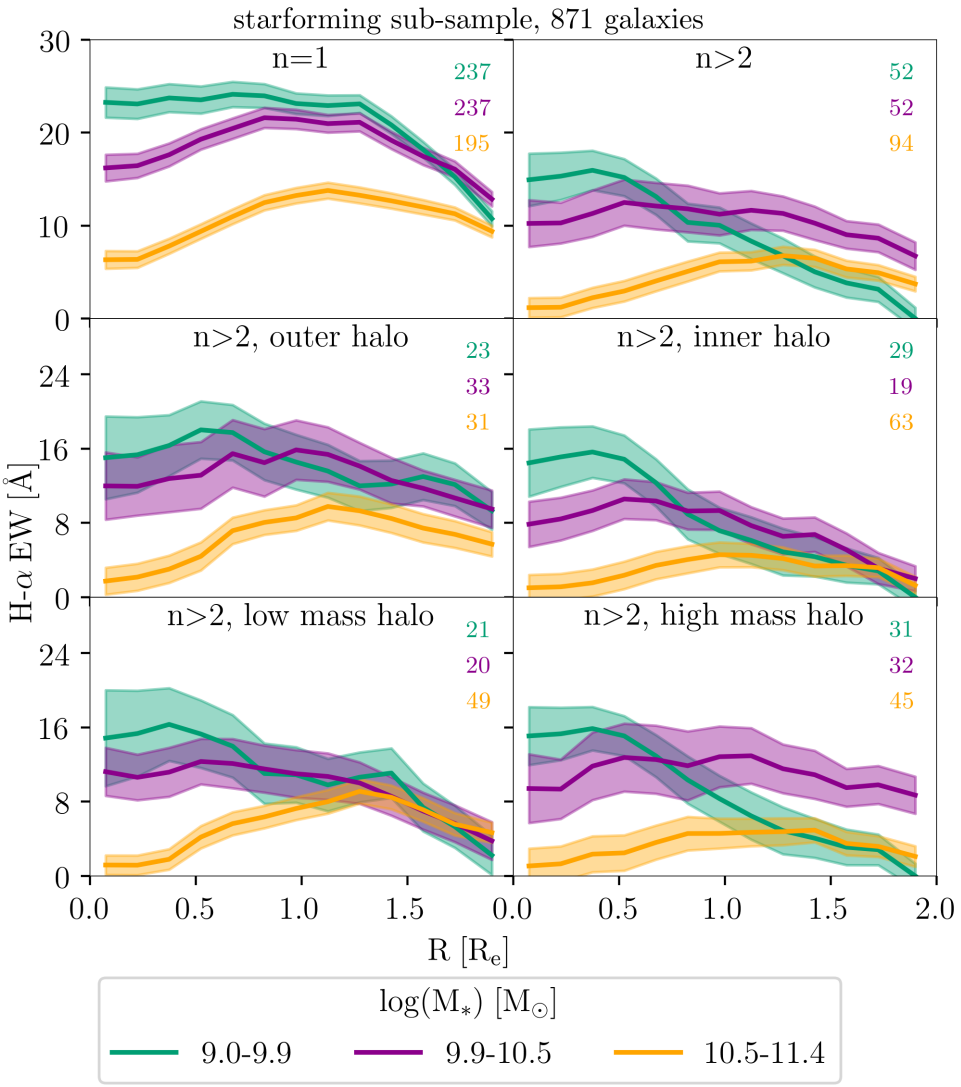

FIGURE 3.5: Median Hα equivalent width (EW) radial profiles are shown for galaxies in the star-forming sub-sample, with galaxies binned by environment and stellar mass. The top row divides galaxies into two groups, with isolated galaxies represented in the sub-plot on the left, and non-isolated galaxies on the right. In the middle row, non-isolated galaxies are divided based on halo-centric distance, with those in the outer halo (r/r180>0.5) on the left and those in the inner halo (r/r180<0.5) on the right. The bottom row divides non-isolated galaxies based on halo-mass, with those in low-mass halos on the left, and high-mass halos on the right. In each sub-plot, galaxies are divided into three bins of stellar mass: $9.0<\log(M_*)<9.9$ $M_\odot$ (green), $9.9<\log(M_*)<10.5$ $M_\odot$ (purple), and $10.5<\log(M_*)<11.5$ $M_\odot$ (yellow). The number of galaxies in each bin is given in the top right of each sub-plot.

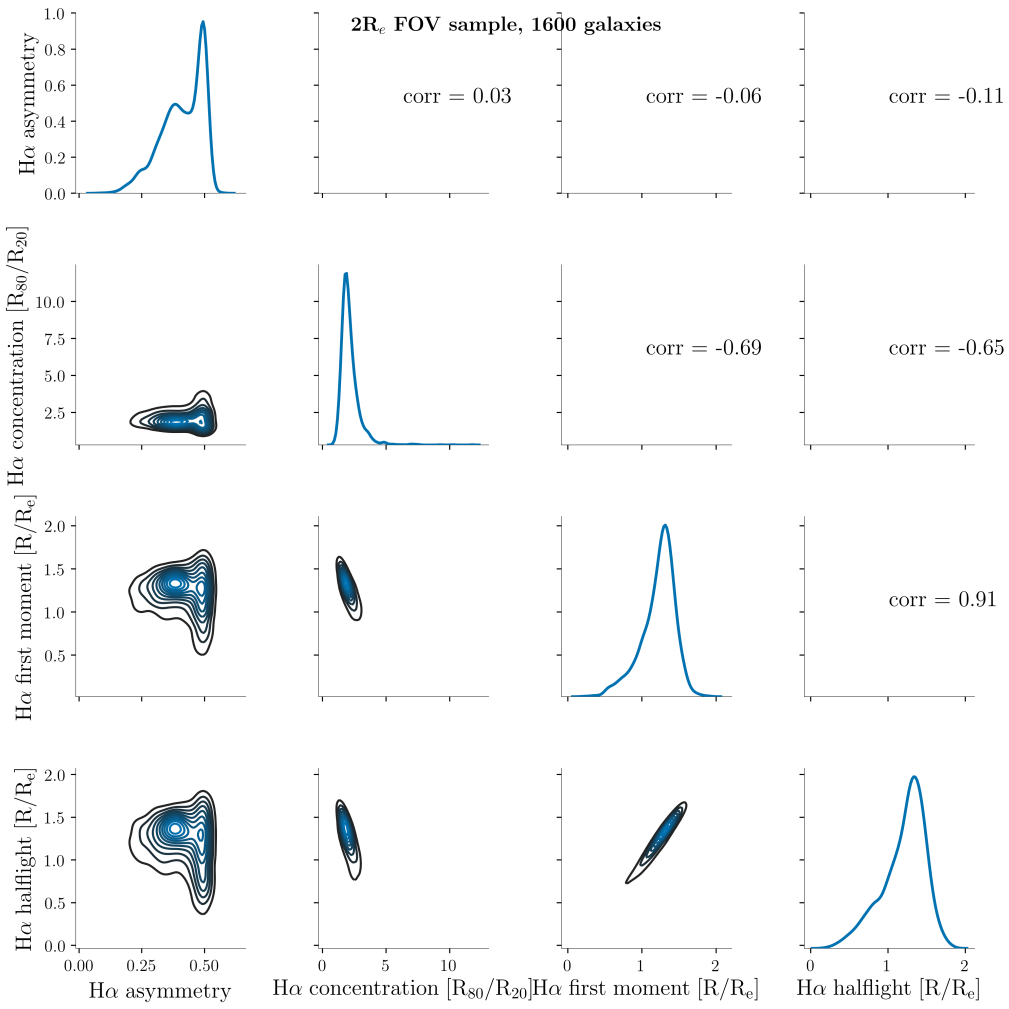

FIGURE 3.6: Correlation grid of the Hα parameters analyzed for galaxies in the sample. Properties shown include Hα EW halflight, first moment, concentration, and asymmetry. Below the diagonal are the 2-D density distributions, while along the diagonal are the 1-D distributions. Above the diagonal are the Spearman's rank correlation coefficients.

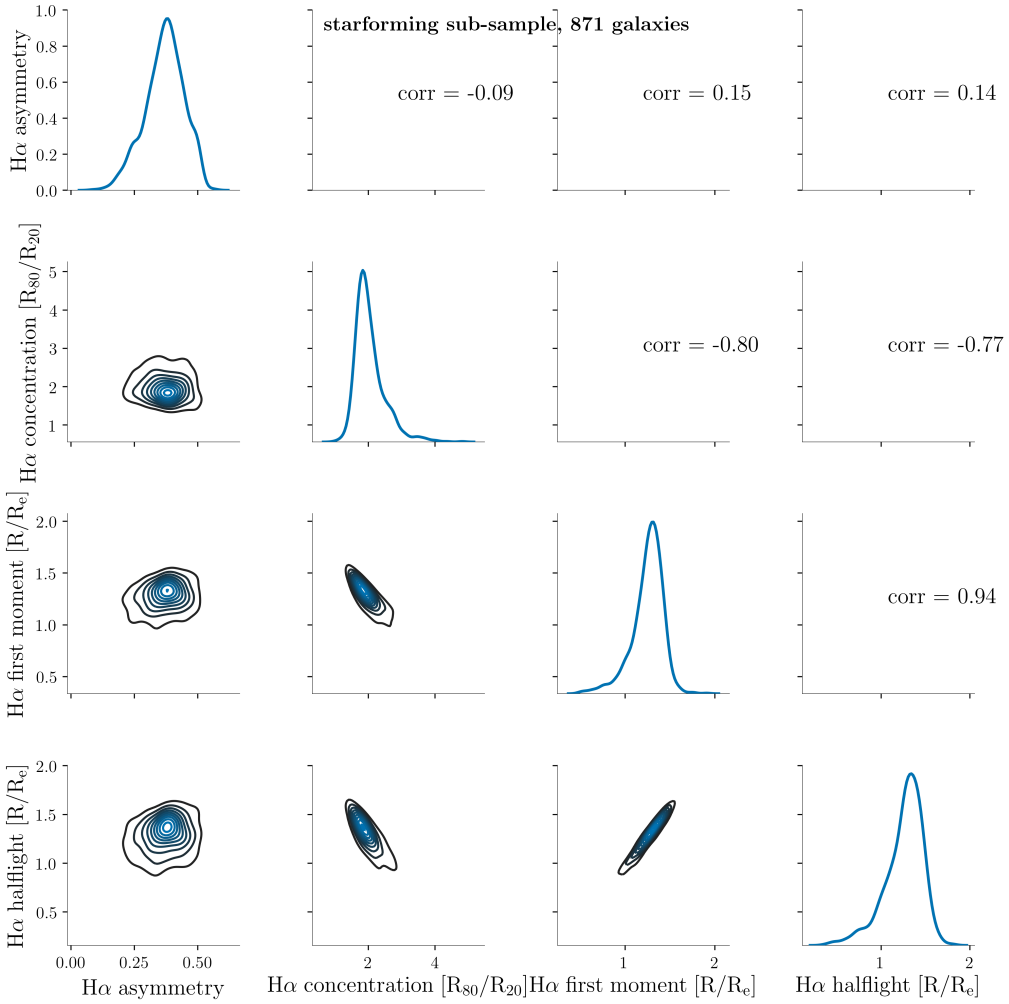

FIGURE 3.7: Correlation grid of the Hα parameters analyzed for galaxies in the star-forming sub-sample. Properties shown include Hα EW halflight, first moment, concentration, and asymmetry. Below the diagonal are the 2-D density distributions, while along the diagonal are the 1-D distributions. Above the diagonal are the Spearman's rank correlation coefficients.

3.2.2 Hα Disk Parameters

This section presents results of our investigation of the four Hα disk parameters: half-light, first moment, concentration and asymmetry. The correlations between each of these parameters are plotted in Figure 3.6 for the full 2R$_e$ sample and Figure 3.7 for the star-forming sub-sample. The half-light and first moment are strongly positively correlated with one another, and both anti-correlated with concentration. The asymmetry index is not correlated with the other Hα parameters. Comparing the asymmetry index in the full sample to the star-forming sub-sample, we see that there is a stronger peak at high asymmetry for the full sample that is not present in the star-forming sub-sample. Figure 3.8 also illustrates that the asymmetry index is lower on average for star-forming galaxies. This is most likely a result of the fact that the net Hα EW in non-star-forming galaxies is lower than that of star-forming galaxies. The asymmetry computation amplifies the small fluctuations in Hα EW across the face of a galaxy with low net Hα EW more so than for those with high net emission.

Hα Disk Trends with Stellar Mass

Each of the Hα disk parameters are plotted against stellar mass in Figure 3.8 for the full sample. Both the Hα half-light and first moment are normalized by the stellar light half-light, and are thus in units of R/R$_e$. The first row of Figure 3.8 therefore illustrates how the extent of the Hα disk as compared to that of the stellar disk differs with stellar mass for galaxies in the sample. For the full 2R$_e$ sample, there is not a significant difference in the mean Hα disk extent between low mass and high mass galaxies. However, for star-forming galaxies, it is clear that Hα disk extent increases with stellar mass. The Hα concentration does not change significantly with stellar mass for the full 2R$_e$ sample, but decreases with stellar mass for the star-forming sub-sample. The high mass star-forming galaxies on average have lower Hα concentration than the high mass galaxies in the full sample. The asymmetry index does not change significantly with mass, however, on average for the sample, very high mass galaxies

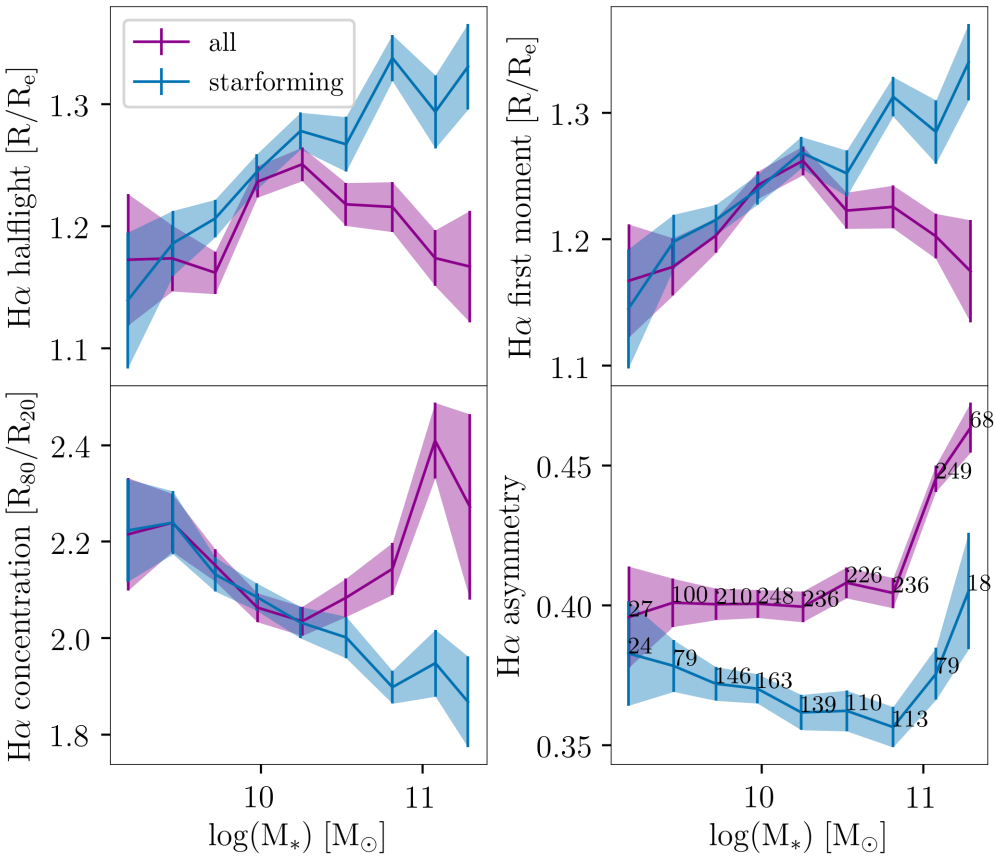

FIGURE 3.8: Hα EW halflight (top left), first moment (top right), concentration (bottom left) and asymmetry (bottom right) vs. stellar mass for the sample (purple) and the star-forming sub-sample (blue). The data points are labelled with the number of galaxies in each bin in the bottom right quadrant, and the standard error is given as vertical bars.

($M_* > 10^{11} M\odot$) have a higher Hα asymmetry index than low and mid-mass galaxies. Galaxies are binned by stellar mass in subsequent plots in order to account for these trends with stellar mass.

Hα Disks Trends with Halo Mass

Figure 3.9 shows the probability density of each of the Hα parameters binned by both stellar mass (in each of the rows) and halo mass (differing colours) for galaxies in the star-forming sub-sample. Figure 3.10 shows the mean and standard error of each of the parameters, where galaxies are binned by stellar mass (on the x-axis) and by halo mass (differing colours). In general, the probability densities of the Hα disk parameters do not change significantly with halo-mass. There is some difference in Hα disk extent of the low stellar mass star-forming galaxies between those that are isolated and those that live in groups with mid-mass halos, as shown in the lower left-most plot of Figure 3.9 and in the top row of Figure 3.10. The Hα disk concentration is slightly higher in group star-forming galaxies that live in mid-mass halos compared to those that are isolated, as seen in the bottom row, third column of Figure 3.9 and the bottom left quadrant of Figure 3.10. Figure 3.11 illustrates how the Hα disk parameters of the star-forming galaxies changes with halo mass (on the x-axis) when binned by stellar mass (colours). Overall, there is large statistical variation in each of the bins. The results in Figures 3.10 and 3.11 demonstrates the need for larger datasets.

Hα Disks of Virialized and Infalling Galaxies

Galaxies in the star-forming sub-sample were also divided based on whether they were isolated, virialized, or infalling (see section 2.2.4). Figure 3.12 shows the probability density plots of the Hα disk parameters for these three environments in bins of stellar mass for the star-forming sub-sample, while Figure 3.13 shows the parameters plotted against stellar mass and binned by the three environments. We found no significant differences in Hα disk parameters between the three environments, with the exception of Hα

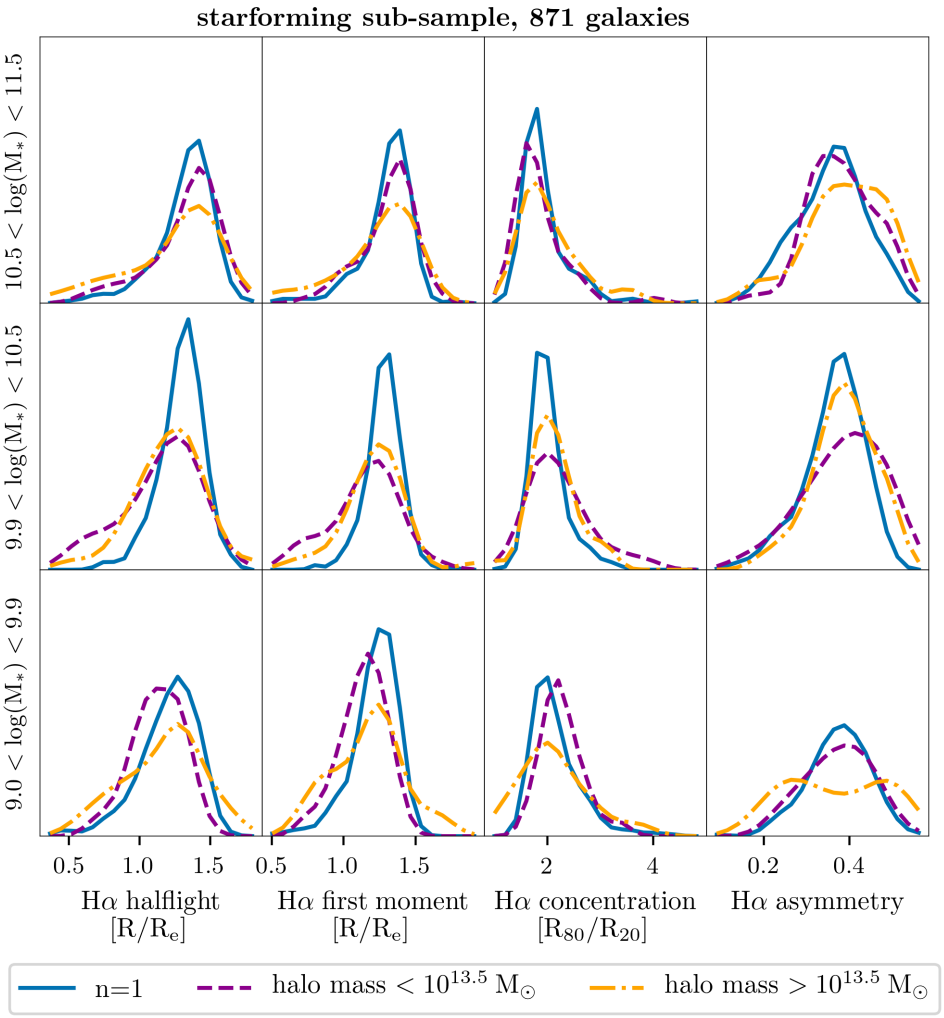

FIGURE 3.9: The KDE distributions of Hα EW parameters (columns) binned by stellar mass (rows) and halo mass (colours). The parameters shown, from left to right, are: halflight, first moment, concentration, and asymmetry. Galaxies are put into bins based on stellar mass, with high stellar mass bins shown in the top row ($10.5 < \log(M_*) < 11.5 M_\odot$), medium stellar mass in the middle row ($9.9 < \log(M_*) < 10.5 M_\odot$), and low stellar mass in the bottom row ($9.0 < \log(M_*) < 9.9 M_\odot$). Each probability distribution colour represents a different environment bin, with isolated galaxy bins in blue, low halo mass bins in purple, and high mass halo bins in yellow.

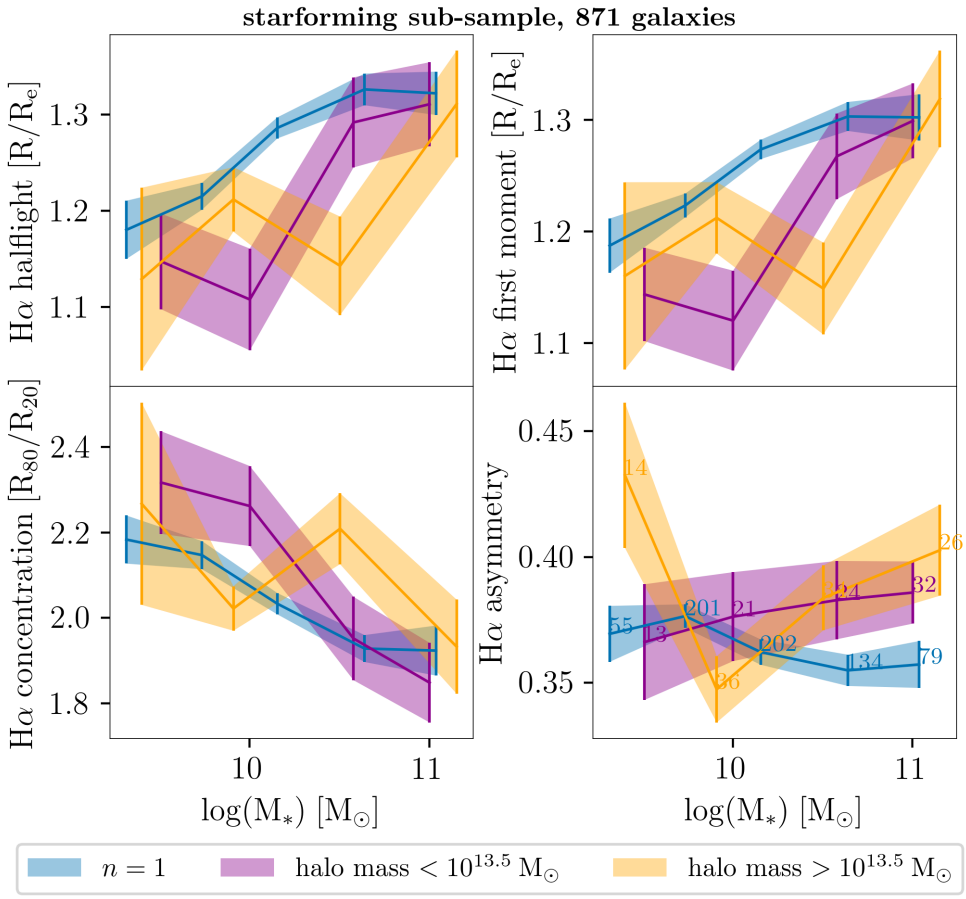

FIGURE 3.10: Hα EW parameters vs. stellar mass for galaxies in the star-forming sub-sample. Parameters plotted include Hα half-light (upper left), first moment (upper right), concentration (lower left) and asymmetry (lower right). Galaxies are divided into three groups based on environment, and the mean value of that parameter plotted for each stellar mass bin for each group. The standard error in the mean is shown as vertical bars at each data point. Bins of isolated galaxies are in blue, galaxies living in low-mass halos ($M_{halo} < 10^{13.5}$) in purple, and those in high-mass halos ($M_{halo} > 10^{13.5}$) in yellow. The bottom right quadrant shows the number of galaxies in each bin.

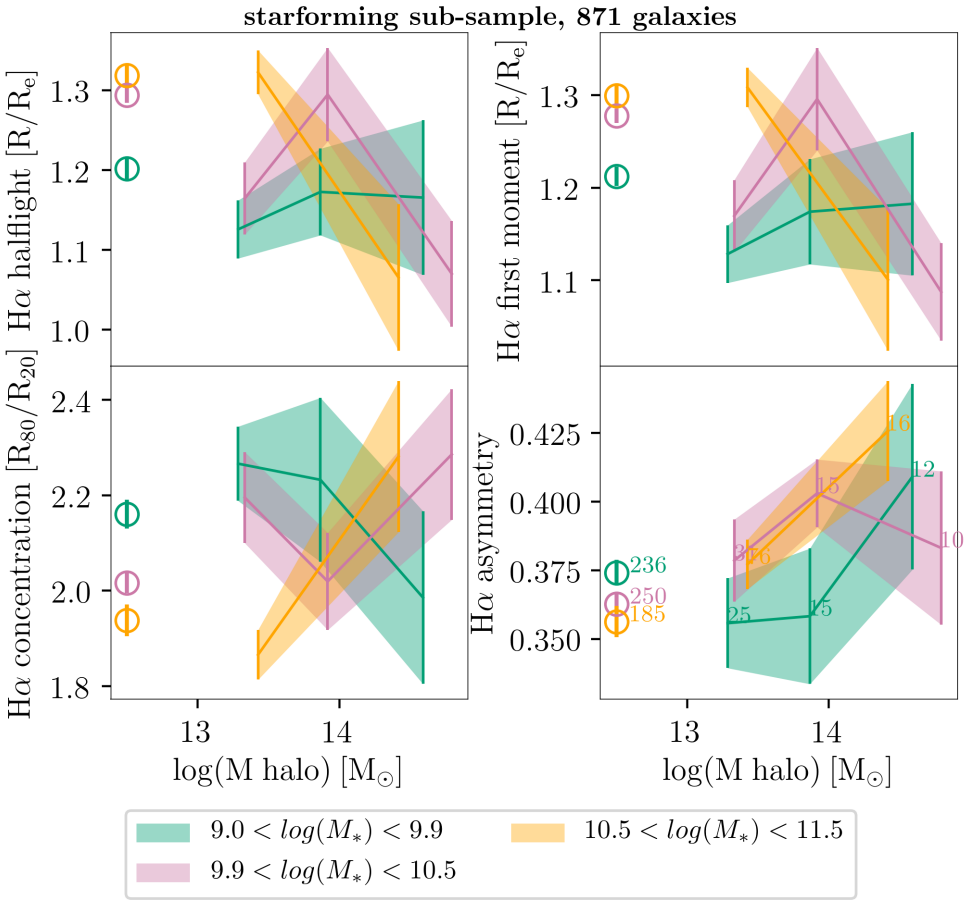

FIGURE 3.11: Hα EW parameters vs. halo mass for galaxies in the star-forming sub-sample. Parameters plotted include Hα half-light (upper left), first moment (upper right), concentration (lower left) and asymmetry (lower right). In each sub-plot, galaxies are divided into three bins of stellar mass: 9.0<log(M_*)<9.9 $M_\odot$ (green), 9.9<log(M_*)<10.5 $M_\odot$ (pink), and 10.5<log(M_*)<11.5 $M_\odot$ (yellow). The mean value of each parameter is plotted for each bin of stellar mass and halo mass, and the standard error is shown as vertical bars. The bins of isolated galaxies are shown as open circles on each sub-plot. The data in the bottom right quadrant are labelled with the number of galaxies in each bin.

asymmetry. We found that on average virialized galaxies ($M_* \gtrsim 10^{10.5} M_\odot$) have higher H$\alpha$ asymmetry than isolated galaxies of the same stellar mass.

Truncated Hα Disks Nearer Group and Cluster Centres

Group galaxies in the star-forming sub-sample have smaller Hα disk extents and higher Hα concentrations if they live near the centre of their group halo ($r/r_{180}<0.5$) compared to those that live in the outer part of the halo ($r/r_{180}>0.5$). This may be evidence of ram pressure stripping near the centre of the halo, as will be discussed in Chapter 4. In the KDE plots in Figure 3.14, galaxies are now binned by halo-centric distance. We can see that for low (bottom row) and medium (middle row) stellar mass galaxies, the Hα EW half-light and first moment probability density peak is at a lower value for the bin with galaxies that are nearer the centre of the halo (in yellow) compared to those that are in the outer parts of the halo (purple). The peak in Hα concentration is also higher for low stellar mass galaxies nearer the centre of the cluster compared to those in the field or the outer part of the cluster. We can see in the top row of Figure 3.14 that the Hα disk extent and concentration of high mass galaxies does not change significantly with halo centric distance.

Figure 3.15 again shows the Hα disk parameters plotted against stellar mass, but now galaxies are in two bins of halo-centric distance and one isolated bin. The largest offset in Hα disk extent (top row) occurs between star-forming galaxies with stellar masses of $\sim 10^{9.9} - 10^{10.5} M_\odot$ (medium mass) that live in the inner part of a group or cluster halo and those that live in the outer part or the field. This trend is confirmed in Figures 3.16 and 3.17, where each Hα parameter is plotted against halo-centric distance in three bins of stellar mass. The medium mass galaxies show the clearest evidence of Hα disk truncation with decreasing halo-centric distance. We found that average Hα half-light (R/R_e) increases with the average halo-centric distance (r/r_{halo}) with a slope on the fit of the mean binned data of 0.40 ± 0.01 for medium-mass galaxies, as illustrated in Figure 3.17.

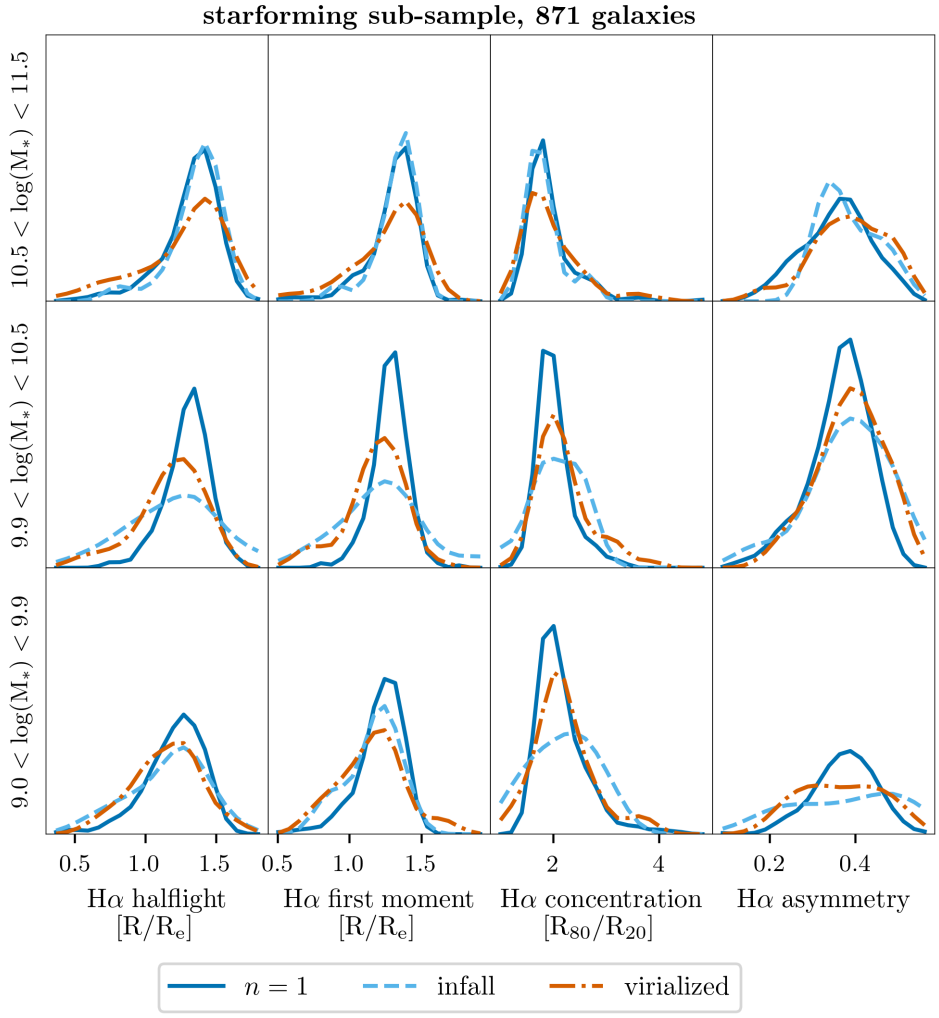

FIGURE 3.12: The KDE distributions of Hα EW parameters (columns) binned by stellar mass (rows) and whether they are isolated (blue), infall (light blue, dashed), or virialized (orange). The parameters shown, from left to right, are: halflight, first moment, concentration, and asymmetry. Galaxies are put into bins based on stellar mass, with high stellar mass bins shown in the top row ($10.5 < \log(M_*) < 11.5 M_\odot$), medium stellar mass in the middle row ($9.9 < \log(M_*) < 10.5 M_\odot$), and low stellar mass in the bottom row ($9.0 < \log(M_*) < 9.9 M_\odot$).

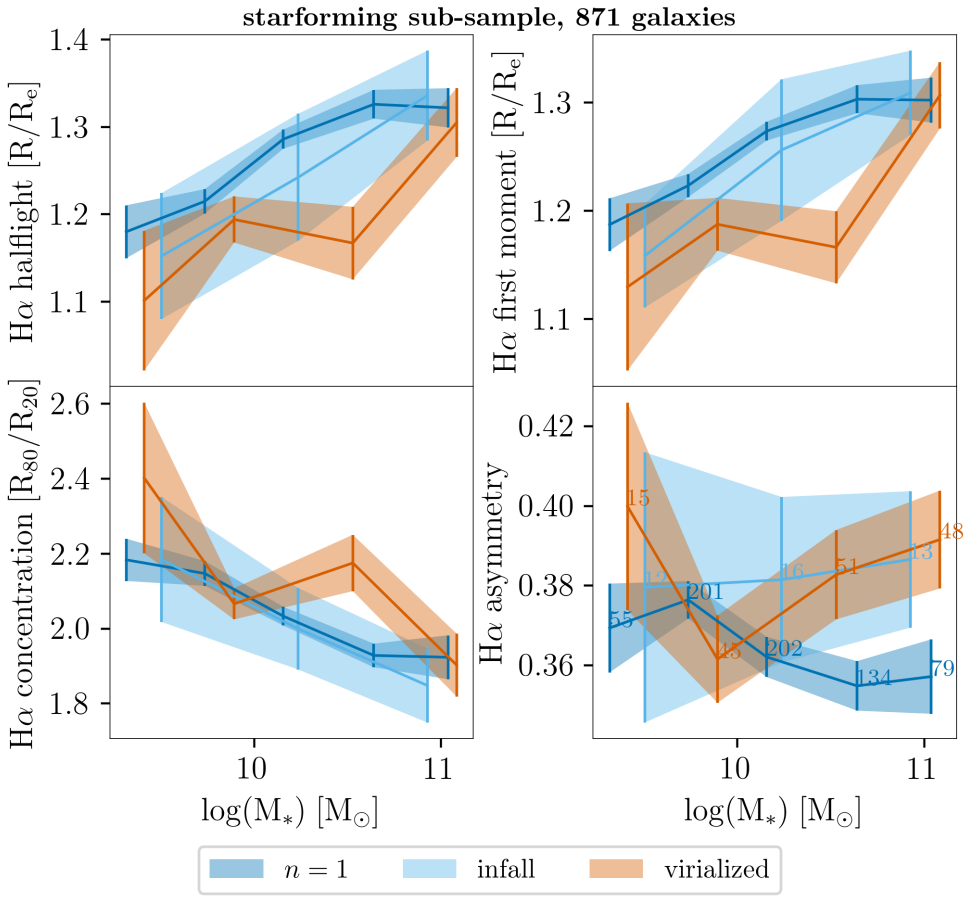

FIGURE 3.13: Hα EW parameters vs. stellar mass for galaxies in the star-forming sub-sample. Parameters plotted include Hα half-light (upper left), first moment (upper right), concentration (lower left) and asymmetry (lower right). Galaxies are divided into three groups based on environment, and the mean value of that parameter plotted for each stellar mass bin for each group. The standard error in the mean is shown as vertical bars at each data point. Bins of isolated galaxies are in blue, infalling galaxies in light blue, and virialized galaxies in yellow. The bottom right quadrant shows the number of galaxies in each bin.

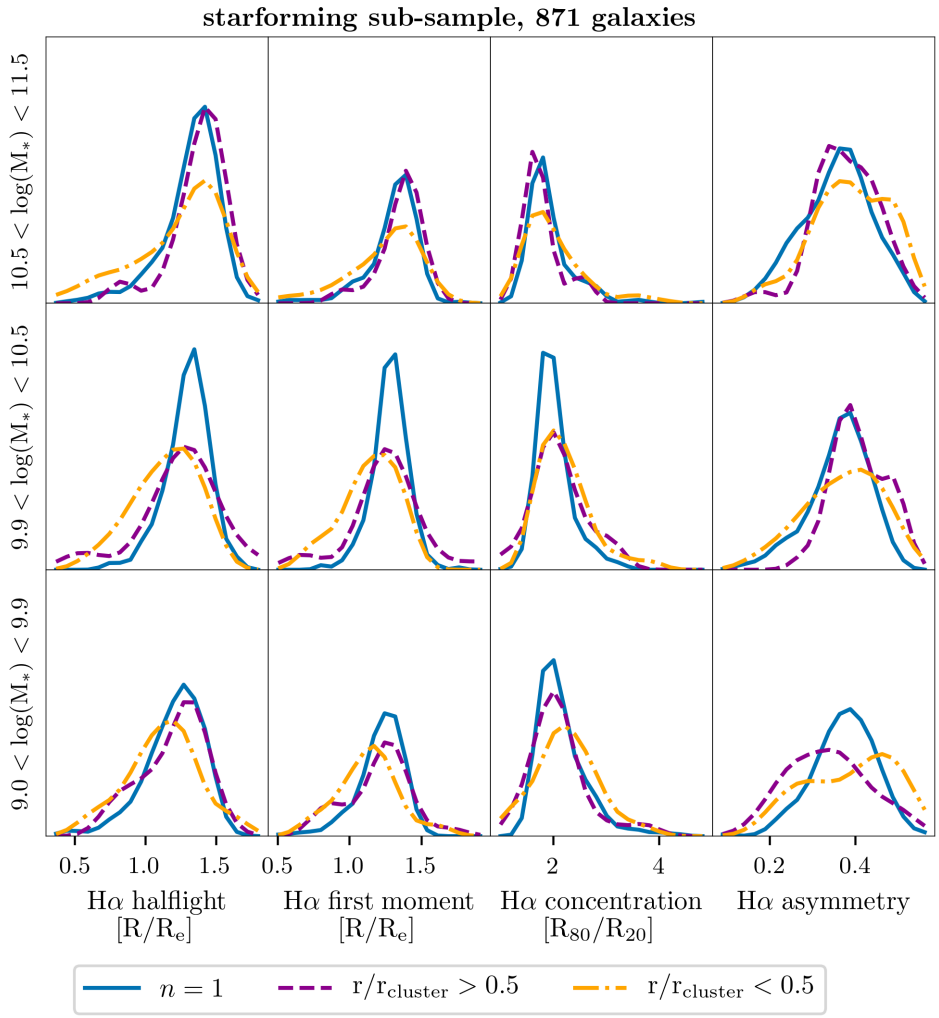

FIGURE 3.14: The KDE distributions of Hα EW parameters (columns) binned by stellar mass (rows) and halo-centric distance (colours). The parameters shown, from left to right, are: halflight, first moment, concentration, and asymmetry. Galaxies are put into bins based on stellar mass, with high stellar mass bins shown in the top row ($10.5 < \log(M_*) < 11.5 M_\odot$), medium stellar mass in the middle row ($9.9 < \log(M_*) < 10.5 M_\odot$), and low stellar mass in the bottom row ($9.0 < \log(M_*) < 9.9 M_\odot$). Each probability distribution colour represents a different environment bin, with isolated galaxy bins in blue, the outer halo bins in purple, and inner halo in yellow.

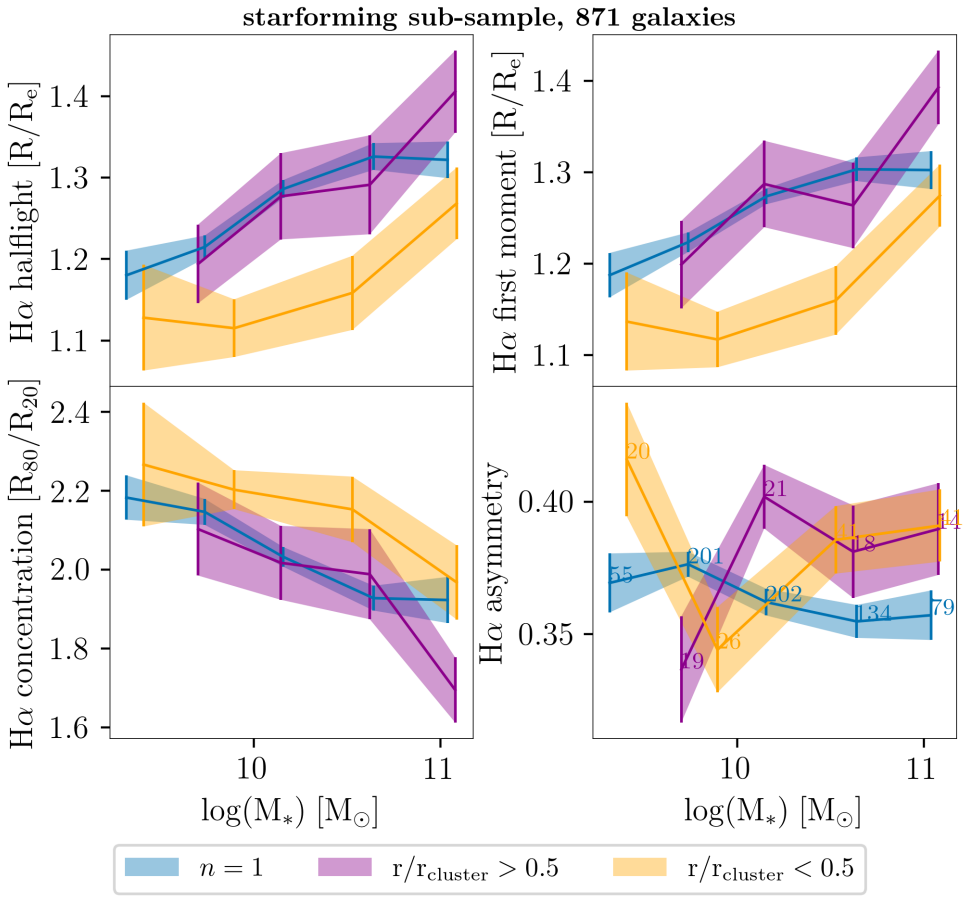

FIGURE 3.15: Hα EW parameters vs. stellar mass for galaxies in the star-forming sub-sample. Parameters plotted include Hα half-light (upper left), first moment (upper right), concentration (lower left) and asymmetry (lower right). Galaxies are divided into three groups based on environment, and the mean value of that parameter plotted for each stellar mass bin for each group. The standard error in the mean is shown as vertical bars at each data point. Bins of isolated galaxies are in blue, non-isolated galaxies living in the outer part of the halo ($r/r_{180} > 0.5$) in purple, and those in inner halo ($r/r_{180} < 0.5$) in yellow. The bottom right quadrant shows the number of galaxies in each bin.

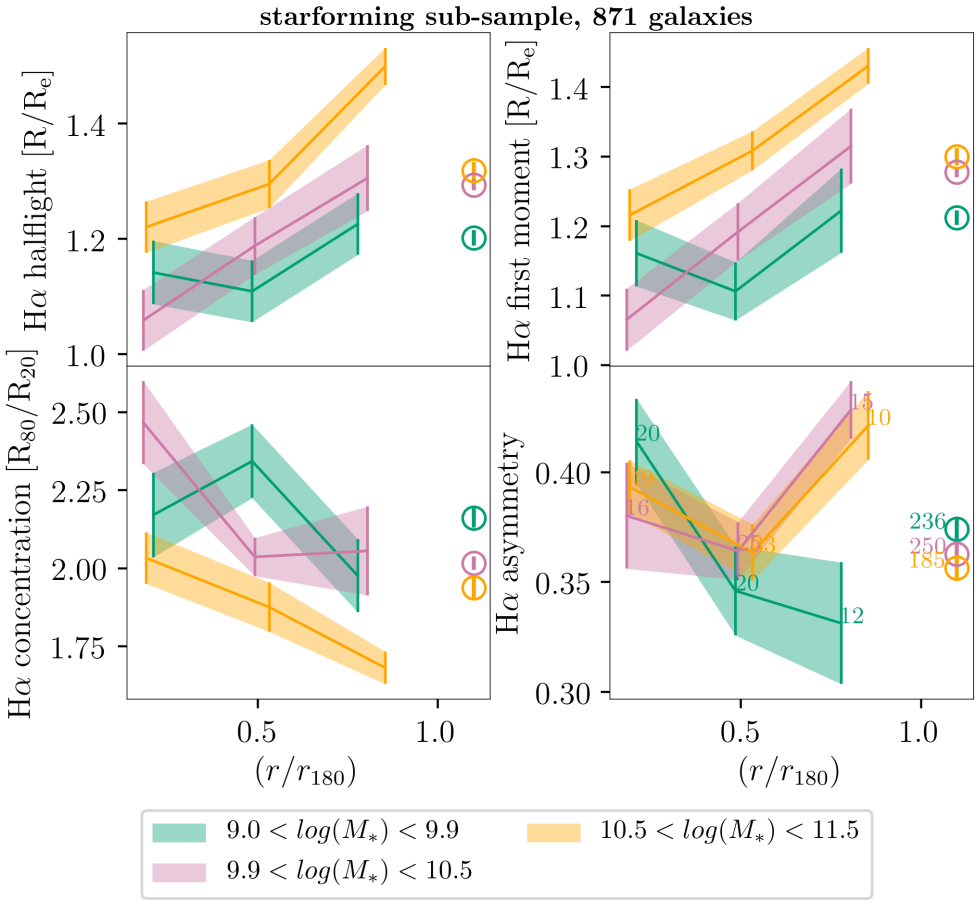

FIGURE 3.16: Hα EW parameters vs. halo-centric distance (r/r_{180}) for galaxies in the star-forming sub-sample. Parameters plotted include Hα half-light (upper left), first moment (upper right), concentration (lower left) and asymmetry (lower right). In each sub-plot, galaxies are divided into three bins of stellar mass: $9.0<\log(M_*)<9.9$ $M_\odot$ (green), $9.9<\log(M_*)<10.5$ $M_\odot$ (pink), and $10.5<\log(M_*)<11.5$ $M_\odot$ (yellow). The mean value of each parameter is plotted for each bin of stellar mass and halo-centric radius, and the standard error is shown as vertical bars. The bins of isolated galaxies are shown as open circles on the right hand side of each sub-plot. The data in the bottom right quadrant are labelled with the number of galaxies in each bin.

The Hα disk extent of star-forming galaxies does not differ significantly between the field and the outer halo, as seen in Figures 3.14 and 3.15. Looking at the profiles in Figure 3.5, we can see that star-forming galaxies in the outer halo have overall lower Hα EW at all galactic radii than field galaxies, but there is no drop in Hα EW in the outer part of the galaxy for outer group galaxies like there is for the galaxies that live in the inner halo. In summary, in the star-forming sub-sample there is on average a decrease in Hα EW for group galaxies compared to isolated galaxies across the entire galaxy face, and a truncation of the Hα disk for group galaxies that live near the centre of the halo.

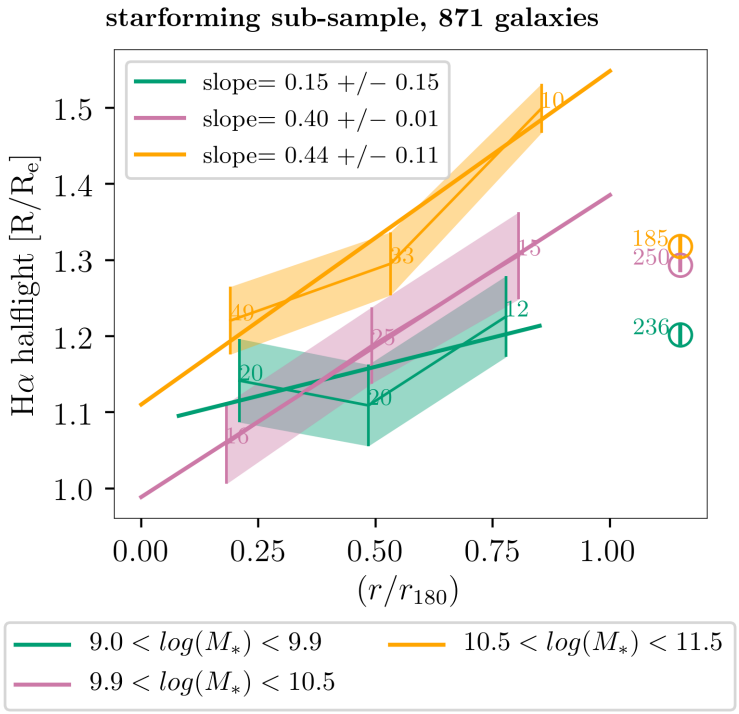

FIGURE 3.17: The Hα half-light is plotted against halo-centric distance, as in the upper left quadrant of Figure 3.16. Bins with isolated galaxies are shown as open circles on the far right. Again, galaxies are divided into three bins of stellar mass: 9.0<log(M$_*$)<9.9 M$_\odot$ (green), 9.9<log(M$_*$)<10.5 M$_\odot$ (pink), and 10.5<log(M$_*$)<11.5 M$_\odot$ (yellow). A line of best fit of the mean and standard error of the binned Hα half-light data is plotted for each stellar mass bin.

Chapter 4

Discussion and Future Work

Our study of the star-forming sub-sample of MaNGA galaxies resulted in three main findings, which are further discussed in this section:

1. sSFR and Hα EW are lower in nearby star-forming galaxies in groups and clusters compared to those in the field, and the lowest in high density environments such as group or cluster centres (see Figure 3.3 and 3.5).

2. The overall reduction in Hα EW in star-forming galaxies in denser environments occurs across the face of these galaxies (see Figure 3.5).

3. Galaxies in the star-forming sub-sample have truncated Hα disks near group and halo centres (see Figures 3.5 and 3.14 - 3.17).

Numerous studies have shown that galaxies in the field have higher star formation rates than galaxies in groups and clusters, as discussed in section 1.2. We confirmed that this is true for all of the galaxies in our sample, as well as for the star-forming sub-sample (Figures 3.2 and 3.3). We also investigated how the integrated star formation rate changes within the group or cluster environment. We found that galaxies within the inner part of the halo ($r/r_{cluster} < 0.5$) have lower sSFR rates than galaxies in the outer part of the halo, and that mid-mass star-forming galaxies in particular ($9.9 < log(\frac{M_*}{M_\odot}) < 10.5$) show a gradual decline in sSFR with decreasing halo-centric distance. This change in average sSFR with halo-centric distance was also observed by Linden et al. (2010) in a sub-sample of SDSS

galaxies. They found that the typical star formation of non-quiescent galaxies declines by a factor of approximately 2 towards the cluster centre.

Further investigations using our resolved data have revealed that this reduction in integrated star formation rate for group and cluster galaxies happens across the entire face of the galaxy, as shown in the Hα EW profiles in Figure 3.5. A number of other studies have investigated the star-forming or Hα profiles of MaNGA data, with similar results. Note that the studies discussed here do not all use the same types of measures of star formation, but come to similar conclusions when comparing how star formation changes with galactic radii in different environments, irrespective of the type of star-formation measure used. Belfiore et al. (2018) studied the radial profiles in Hα EW and sSFR of the MaNGA data for both star-forming and green valley galaxies. They found that galaxies with lower global sSFR also had lower sSFR at all radii, and concluded that quenching mechanisms must affect the entire galaxy. In our study, we focused on only star-forming galaxies but also looked at how the profiles differed in different environments, finding that galaxies in the field have higher Hα EW at all galactic radii than galaxies in groups and clusters. This is similar to the results of another study of MaNGA data by Spindler et al. (2018), who looked instead at sSFR profiles of galaxies in different environments. They found that satellites (galaxies in groups or clusters that are not the central galaxy) were more likely to have suppressed sSFR compared to centrals (which includes isolated galaxies) at all galactic radii. They argued that starvation (or strangulation) is the main quenching mechanism at play for galaxies in groups and clusters, since this is expected to reduce the gas content across the entire galaxy (see section 1.3.2).

Spindler et al. (2018) also looked at SFR surface density ($\Sigma_{\rm SFR}$) gradients and found only a slight, not statistically significant steepening in SFR surface density ($\Sigma_{\rm SFR}$) gradients with environment density in the MaNGA data. Note however that $\Sigma_{\rm SFR}$ trends with stellar mass surface density (Σ_*) for star forming regions within galaxies (see, for example, Abdurro'uf and Akiyama, 2018). Thus, $\Sigma_{\rm SFR}$ alone does not indicate whether a region is

forming stars at a rate consistent with the main sequence or not, which is why Bluck et al. (2020) instead used ΔSFR surface density ($\Delta\Sigma_{\rm SFR}$)[1] to compare star formation across the face of galaxies in MaNGA. Bluck et al. (2020) also looked at luminosity-weighted stellar age, as well as an analysis of metallicities of MaNGA galaxies. They concluded that both intrinsic and environmental quenching must incorporate starvation of gas supply. They found that high-mass satellites quench similarly to centrals, with quenching happening at the centre as illustrated by rising $\Delta\Sigma_{\rm SFR}$ profiles.

We found a similar trend in our Hα EW profiles as Bluck et al. (2020) found for $\Delta\Sigma_{\rm SFR}$ profiles: high mass galaxies both in the field and in groups and clusters tend to have lower Hα EW in their centres and rising profiles. Bluck et al. (2020) found that central velocity dispersion was the most important single parameter that correlated with central quenching. They found that $\Delta\Sigma_{\rm SFR}$ of low stellar mass satellites decline, which is what we found, but for the Hα profiles. They determined that these declining profiles are most influenced by environment, with local galaxy over-density being the biggest factor in environmental quenching.

Lian et al. (2019) also conducted an analysis of profiles of galaxies in the MaNGA data, but looked at gas metallicity gradients as well as SFR in star-forming galaxies. They looked at two measures of environment: centrals versus satellites, and using the Nth nearest neighbour as a proxy for environment density. They also used a chemical evolution model to reproduce the observed trends. They found steeper SFR gradients in denser environments in the data, which most closely aligned with the model scenario where gas accretion of low-mass satellites is suppressed at large galactic radii in dense regions. This is similar to what had previously been found by both Schaefer et al. (2016) and Medling et al. (2018) in another

[1] Bluck et al. (2020) computes the $\Delta\Sigma_{\rm SFR}$ for each spaxel by measuring the logarithmic distance each spaxel resides from the resolved star forming main sequence line. The resolved star forming main sequence line is determined from the SFR rate surface density ($\Sigma_{\rm SFR}$)) versus stellar mass surface density (Σ_*) relation for all spaxels in all galaxies.

IFU survey, the Sydney-Australian-Astronomical-Observatory Multi-object Integral-Field Spectrograph (SAMI). These studies found that the sSFR gradients of galaxies in SAMI decreased with galactocentric radius irrespective of morphology, and that this gradient was steeper in denser environments, supporting environmental quenching such as ram-pressure stripping or galaxy interactions.

Our Hα EW profiles do not show a marked reduction at the galaxy outskirts for all group galaxies. However, our profiles do show a drop in Hα EW beyond $0.75R_e$ for low mass star-forming galaxies in the inner halo. As discussed in Section 1.3.2, ram pressure stripping is thought to be most effective in the densest environments and nearest the cluster centre. Thus, while our reduced Hα EW profiles in groups and clusters are evidence of starvation or strangulation, that the profiles of low-mass galaxies show a marked drop in Hα EW at $\sim 0.75R_e$ near the centre of groups and clusters is similar to other MaNGA findings and evidence for ram pressure stripping.

Our Hα profiles show the median Hα EW emission versus galactic radius. Another means of investigating the distribution of Hα is by parameterizing the total Hα EW relative to the total continuum emission. Ram pressure stripping is thought to confine star formation to the central regions of galaxies (Quilis et al., 2000). We tested for this confinement through the characterization of the Hα disk via the half-light, first moment and concentration indices. A small half-light radius or first moment relative to the stellar disk ($R_{H\alpha}/R_e$), or high Hα concentration index indicates that either Hα EW is enhanced in the central regions, or suppressed in the galaxy outskirts, or both. We found that for star-forming galaxies with $M_* > 10^{9.9}M_\odot$, those that live near the group or cluster centre have smaller $R_{H\alpha}/R_e$ and higher Hα concentration than those that live near the outskirts.

Evidence of Hα disk truncation of star-forming galaxies in dense environments has been seen in other datasets. In an analysis of SAMI data, Schaefer et al. (2019) found that massive star-forming galaxies in high mass groups have centrally concentrated star formation. We did not see any statistically significant difference in Hα disk size between star-forming galaxies

in low and high mass halos, but this is may be due to the small sample size. On the other hand, Finn et al. (2018) used local galaxy density and distance to cluster centre as measures of environment in their analysis of star-forming galaxies. They measured the size of star-forming disks of 224 galaxies in 9 groups and clusters using 24μm imaging from the *Spitzer Space Telescope* and found that star-forming galaxies in more dense environments have more centrally concentrated star formation than galaxies in less dense environments with similar mass and bulge-to-total ratios (B/T). Along with these new results from the MaNGA data, there is growing evidence that halo-centric distance correlates with the star-forming disk size of star-forming galaxies, which points to ram pressure stripping as a key quenching mechanism in group and cluster cores.

Summary

We analysed the environmental dependence of Hα disk trends of star-forming (sSFR $> 10^{-10.8}$yr^{-1}) galaxies mapped out to 2R$_e$ using MaNGA IFU data. The most significant trends we found were with halo-centric distance. In agreement with previous studies, we found that on average, star-forming galaxies in groups and clusters have lower integrated sSFR than isolated galaxies, and that galaxies near the centre of the group or cluster halo have lower sSFR than galaxies in the outer part of the halo. We used the resolved Hα data to create median Hα profiles out to 2R$_e$ for these galaxies in bins of stellar mass and environment, finding that the Hα EW is systematically lower at all galactic radii for galaxies in groups compared to isolated galaxies. This reduction in Hα EW across the entire galaxy is evidence of starvation as a primary quenching mechanism in groups and clusters. We also saw evidence of ram pressure stripping in the inner part of the halo. Low-mass galaxies in the inner part of the halo have a more significant drop in Hα EW at ~ 0.75R$_e$ compared to low-mass galaxies in the outer part of the halo or the field. We also compared the Hα disk extent (r$_{H\alpha}$/r$_e$), concentration and asymmetry of our star-forming sub-sample in different environments. The most significant finding was that star-forming galaxies in the inner part of the halo have a slightly smaller

Hα disk extent and slightly larger Hα concentration compared to those in the outer part of the halo and the field.

Future Work

One of the main limitations of our study was the small numbers of galaxies in groups and clusters in our sub-sample. Of the $2R_e$ star-forming sub-sample, 200 galaxies are in groups and clusters. Once these 200 galaxies are further divided into different bins based on environment, low numbers in some of the bins made it difficult to find statistically significant trends in the data. Specifically, there were not adequate numbers of backsplash nor infalling galaxies identified in the sample to look for differences in the Hα disks between backsplash, virialized, and infalling galaxies. The study could be repeated with more data once the remaining MaNGA data are released.

Future IFU surveys could target group and cluster galaxies specifically to ensure adequate numbers to enable comparisons between different group and cluster environments. Furthermore, future IFU surveys should aim to target a larger extent of the galaxy. Only a subset of MaNGA galaxies are mapped out to at least $2R_e$. If ram pressure stripping is present, it can be better identified using resolved data if the galaxy is mapped out further than $2R_e$, since it occurs around the galaxy outskirts.

The Gemini Infrared Multi-Object Spectrograph (GIRMOS) is an example of an exciting new instrument that can be used to gather more resolved Hα galaxy data. Set to be operational in 2023, it will carry out simultaneous high-angular-resolution, spatially resolved infrared spectroscopy using multi-object adaptive optics (Sivanandam et al., 2018). It will therefore enable the investigation of resolved Hα disks of galaxies at higher redshift, allowing comparisons between high and low redshift galaxies that will further constrain quenching mechanisms.

Resolved measurements of gas surface density of galaxies in different environments would also be useful to determine the effects of environment

on star formation, since gas surface density directly correlates with SFR (see Kennicutt, 1998b). The Virgo Environment Traced in CO (VERTICO) project will provide high resolution maps of molecular gas in 51 spiral galaxies in the Virgo Cluster using ALMA. This and other future projects that trace molecular gas in group and cluster galaxies will help to quantify the impact of the group or cluster environment on star formation.

Appendix A

AGN Galaxies Removed from Sample

We performed our analysis of Hα disks with AGN galaxies removed from the sample. Section 2.1.4 describes the criteria used to remove AGN galaxies. Key results from Chapter 3 are presented here for the sub-sample with AGN galaxies removed. These key results remain the same once AGN galaxies are removed from the sample. Figure A1.1 shows the reduction in Hα emission at all galactic radii and the Hα disk truncation of low and mid-mass galaxies in the inner halo. The decrease in Hα half-light with halo-centric distance is also seen in Figures A1.2 - A1.4.

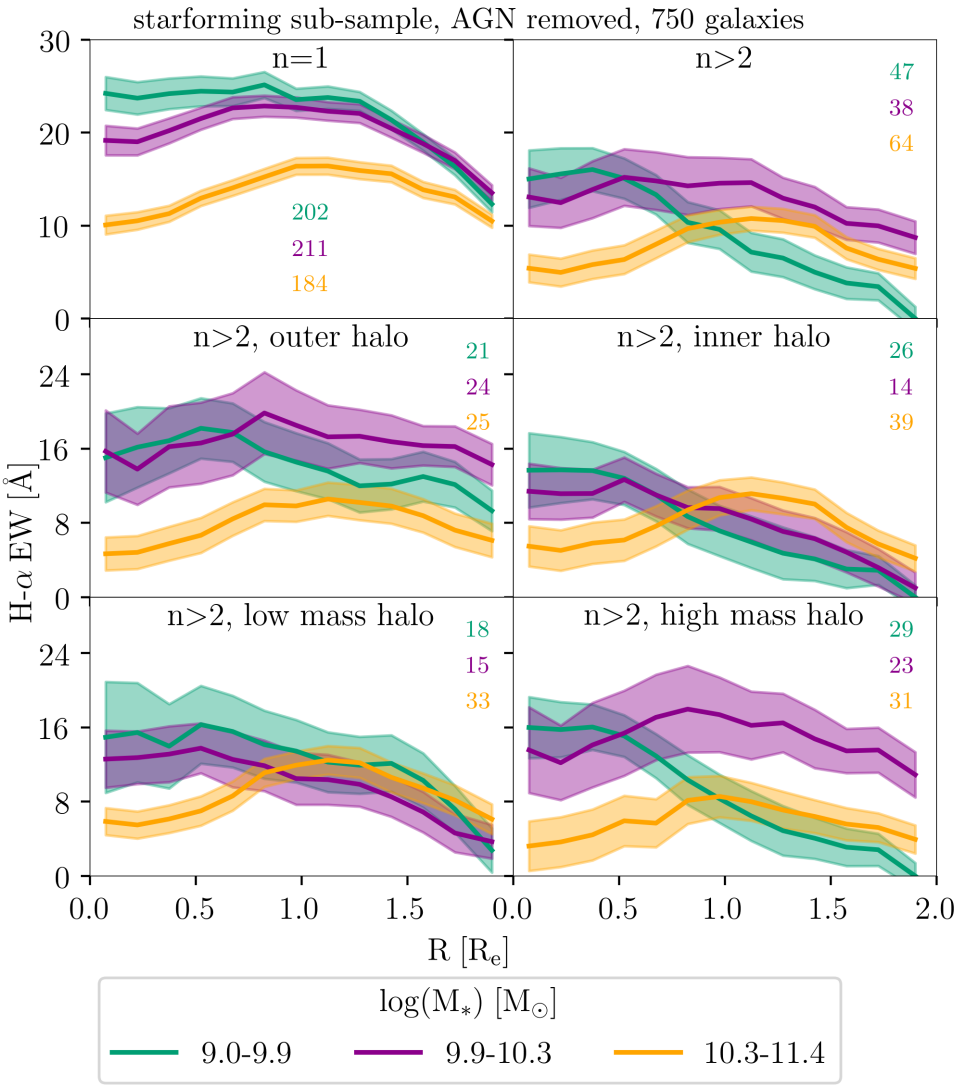

FIGURE A1.1: Median Hα equivalent width (EW) radial profiles are shown for non-AGN galaxies in the starforming sub-sample, with galaxies binned by environment and stellar mass. The top row divides galaxies into two groups, with isolated galaxies represented in the sub-plot on the left, and non-isolated galaxies on the right. In the middle row, non-isolated galaxies are divided based on halo-centric distance, with those in the outer halo on the left and those in the inner halo on the right. The bottom row divides non-isolated galaxies based on halo-mass, with those in low-mass halos on the left, and high-mass halos on the right. In each sub-plot, galaxies are divided into three bins of stellar mass: $9.0<\log(M_*)<9.9$ $M_\odot$ (green), $9.9<\log(M_*)<10.5$ $M_\odot$ (purple), and $10.5<\log(M_*)<11.5$ $M_\odot$ (yellow). The number of galaxies in each bin is given in the top right of each sub-plot.

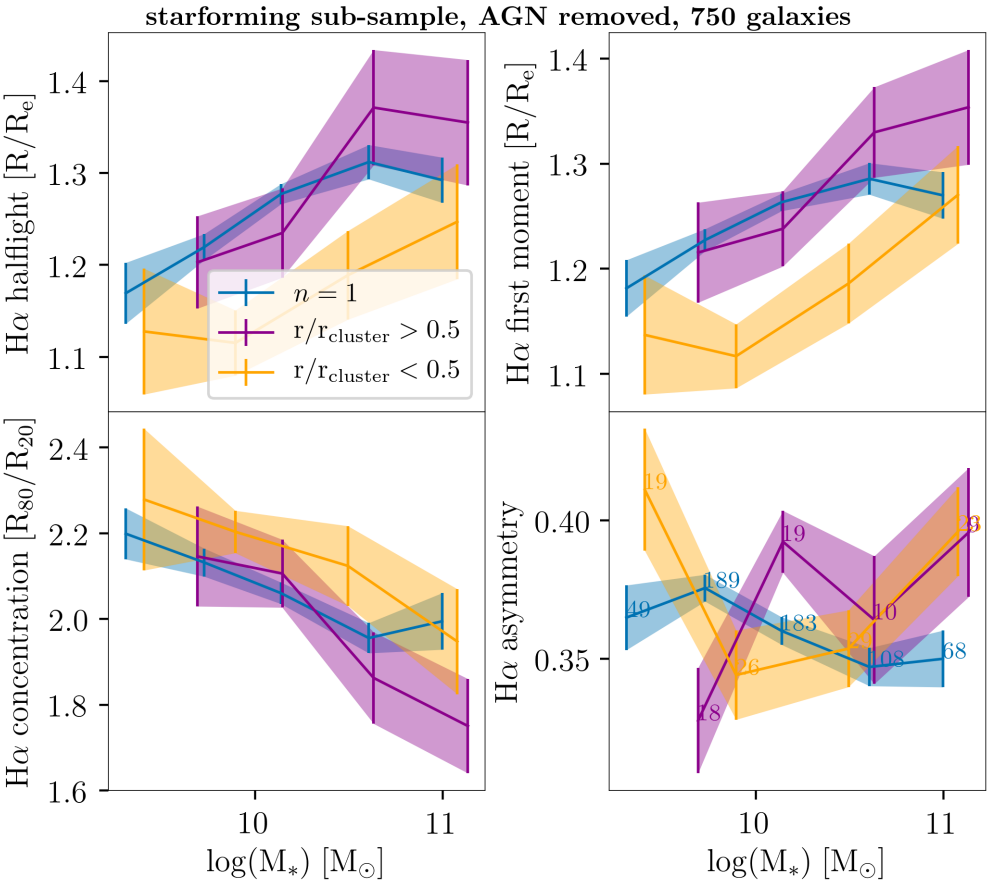

FIGURE A1.2: Hα EW parameters vs. stellar mass for galaxies in the starforming sub-sample that are not AGN. Parameters plotted include Hα half-light (upper left), first moment (upper right), concentration (lower left) and asymmetry (lower right). Galaxies are divided into three groups based on environment, and the mean value of that parameter determined for each stellar mass bin for each group. The standard error in the mean is shown as vertical bars at each data point. Bins of isolated galaxies are in blue, non-isolated galaxies living in the outer part of the halo ($r/r_{180} > 0.5$) in purple, and those in inner halo ($r/r_{180} < 0.5$) in yellow. The bottom right quadrant shows the number of galaxies in each bin.

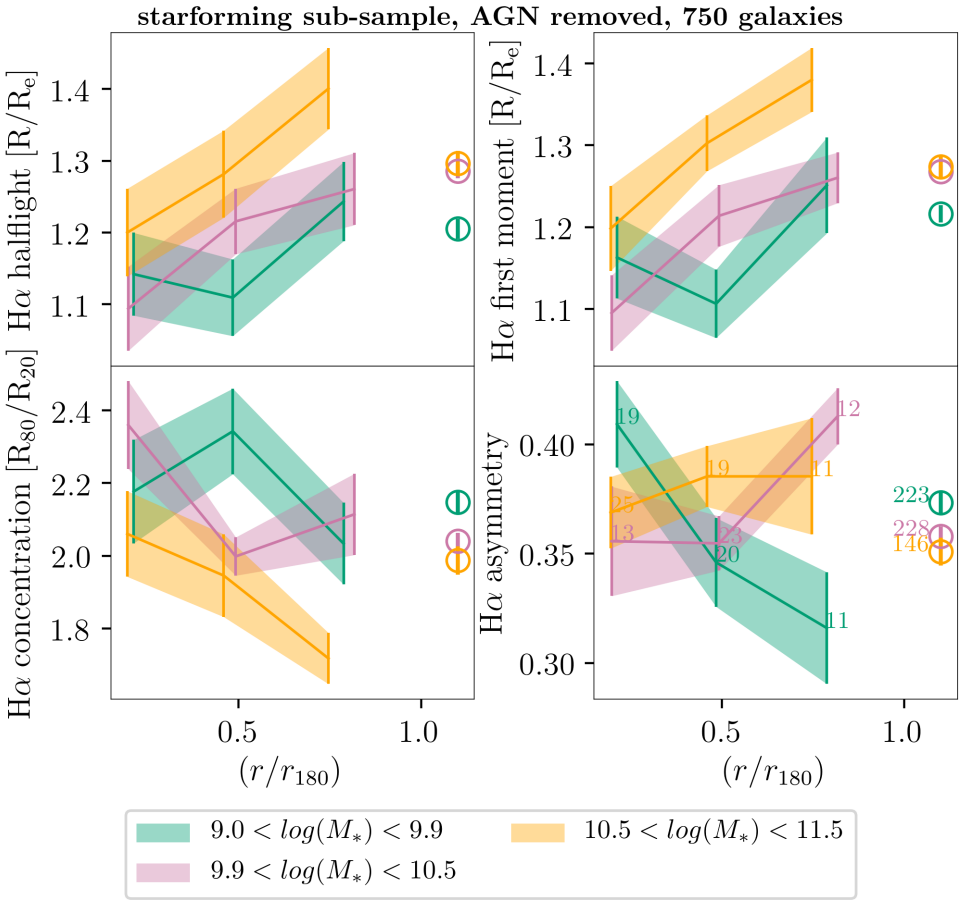

FIGURE A1.3: Hα EW parameters vs. halo-centric distance (r/r_{180}) for galaxies in the starforming sub-sample that are not AGN. Parameters plotted include Hα half-light (upper left), first moment (upper right), concentration (lower left) and asymmetry (lower right). In each sub-plot, galaxies are divided into three bins of stellar mass: $9.0<\log(M_*)<9.9$ $M_\odot$ (green), $9.9<\log(M_*)<10.5$ $M_\odot$ (pink), and $10.5<\log(M_*)<11.5$ $M_\odot$ (yellow). The mean value of each parameter is plotted for each bin of stellar mass and halo-centric radius, and the standard error is shown as vertical bars. The bins of isolated galaxies are shown as open circles on the right hand side of each sub-plot. The data in the bottom right quadrant are labelled with the number of galaxies in each bin.

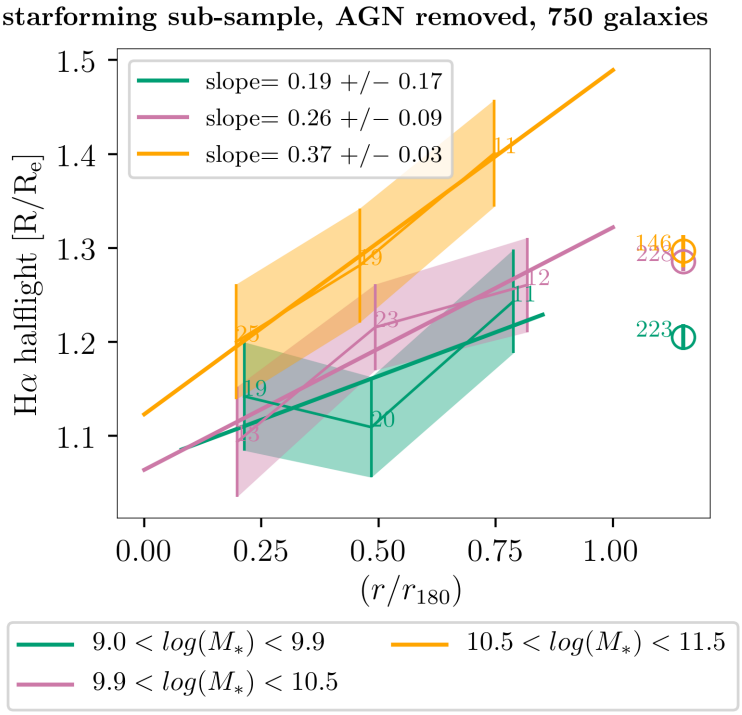

FIGURE A1.4: The Hα half-light is plotted against halo-centric distance, as in the upper left quadrant of Figure A1.3. Bins with isolated galaxies are shown as open circles on the far right of the plot. Again, galaxies are divided into three bins of stellar mass: 9.0<log(M$_*$)<9.9 M$_\odot$ (green), 9.9<log(M$_*$)<10.5 M$_\odot$ (pink), and 10.5<log(M$_*$)<11.5 M$_\odot$ (yellow). A line of best fit of the Hα half-light trend with halo-centric distance is plotted for each stellar mass bin.

Bibliography

Abadi, M. G., Moore, B., and Bower, R. G. (1999). Ram pressure stripping of spiral galaxies in clusters. *MNRAS* 308(4), 947–954.

Abdurro'uf and Akiyama, M. (2018). Evolution of spatially resolved star formation main sequence and surface density profiles in massive disc galaxies at 0 z 1: inside–out stellar mass buildup and quenching. *Monthly Notices of the Royal Astronomical Society* 479(4), 5083–5100. ISSN: 0035-8711.

Abell, G. O. (1958). The Distribution of Rich Clusters of Galaxies. *ApJ Supp.* 3, 211.

Alpresa, P. et al. (2010). Isolated Galaxies vs Galaxies in Groups: a Study of Their Properties from Cosmological Simulations.

Applegate, D. E. et al. (2014). Weighing the Giants – III. Methods and measurements of accurate galaxy cluster weak-lensing masses. *Monthly Notices of the Royal Astronomical Society* 439(1), 48–72. ISSN: 0035-8711.

Baldry, I. K. et al. (2006). Galaxy bimodality versus stellar mass and environment. *MNRAS* 373(2), 469–483.

Baldwin, J. A., Phillips, M. M., and Terlevich, R. (1981). Classification parameters for the emission-line spectra of extragalactic objects. *Publications of the Astronomical Society of the Pacific* 93, 5–19.

Begelman, M. C. (1985). Accretion disks in active galactic nuclei. In: *Astrophysics of Active Galaxies and Quasi-Stellar Objects*. Ed. by J. S. Miller, 411–452.

Belfiore, F. et al. (2018). SDSS IV MaNGA – sSFR profiles and the slow quenching of discs in green valley galaxies. *Monthly Notices of the Royal Astronomical Society* 477(3), 3014–3029. ISSN: 0035-8711.

Belfiore, F. et al. (2019). The Data Analysis Pipeline for the SDSS-IV MaNGA IFU Galaxy Survey: Emission-line Modeling. *The Astronomical Journal* 158(4), 160.

Birnboim, Y. and Dekel, A. (2003). Virial shocks in galactic haloes? *MNRAS* 345(1), 349–364.

Blandford, R., Meier, D., and Readhead, A. (2019). Relativistic Jets from Active Galactic Nuclei. *Ann. Rev. of Astron. & Astrophys.* 57, 467–509.

Blanton, M. R. and Moustakas, J. (2009). Physical Properties and Environments of Nearby Galaxies. *Ann. Rev. of Astron. & Astrophys.* 47(1), 159–210.

Bluck, A. F. L. et al. (2014). Bulge mass is king: the dominant role of the bulge in determining the fraction of passive galaxies in the Sloan Digital Sky Survey. *MNRAS* 441(1), 599–629.

Bluck, A. F. L. et al. (2020). How do central and satellite galaxies quench? – Insights from spatially resolved spectroscopy in the MaNGA survey. *arXiv e-prints* arXiv:2009.05341, arXiv:2009.05341.

Book, L. G. and Benson, A. J. (2010). The Role of Ram Pressure Stripping in the Quenching of Cluster Star Formation. *ApJ* 716(1), 810–818.

Bower, R. G. et al. (1994). ROSAT observations of distant, optically selected galaxy clusters. *MNRAS* 268, 345–353.

Brinchmann, J. et al. (2004). The physical properties of star-forming galaxies in the low-redshift Universe. *MNRAS* 351(4), 1151–1179.

Bundy, K. et al. (2015). Overview of the SDSS-IV MaNGA Survey: Mapping nearby Galaxies at Apache Point Observatory. *ApJ* 798(1) 7, 7.

Cappellari, M. (2016). Improving the full spectrum fitting method: accurate convolution with Gauss–Hermite functions. *Monthly Notices of the Royal Astronomical Society* 466(1), 798–811. ISSN: 0035-8711.

Cappellari, M. and Emsellem, E. (2004). Parametric Recovery of Line-of-Sight Velocity Distributions from Absorption-Line Spectra of Galaxies via Penalized Likelihood. *Publications of the Astronomical Society of the Pacific* 116(816), 138–147.

Carollo, C. M. et al. (2013). The Zurich Environmental Study of Galaxies in Groups along the Cosmic Web. I. Which Environment Affects Galaxy Evolution? *ApJ* 776(2) 71, 71.

Carroll, B. W. and Ostlie, D. A. (2007). *An Introduction to Modern Astrophysics*. Ed. by S. F. P. Addison-Wesley. 2nd (International).

Catalán-Torrecilla, C. et al. (2017). Star Formation in the Local Universe from the CALIFA Sample. II. Activation and Quenching Mechanisms in Bulges, Bars, and Disks. *ApJ* 848(2) 87, 87.

Chauke, P. et al. (2019). Rejuvenation in z 0.8 Quiescent Galaxies in LEGA-C. *ApJ* 877(1) 48, 48.

Chen, Z. et al. (2020). Quenching as a Contest between Galaxy Halos and Their Central Black Holes. *ApJ* 897(1) 102, 102.

Cherinka, B. et al. (2019). Marvin: A Tool Kit for Streamlined Access and Visualization of the SDSS-IV MaNGA Data Set. *Astronomical Journal* 158(2) 74, 74.

Chon, G., Böhringer, Hans, and Zaroubi, Saleem (2015). On the definition of superclusters. *A&A* 575, L14.

Coe, D. et al. (2012). CLASH: THREE STRONGLY LENSED IMAGES OF A CANDIDATE z ≈ 11 GALAXY. *The Astrophysical Journal* 762(1), 32.

Connelly, J. L. et al. (2012). EXPLORING THE DIVERSITY OF GROUPS AT 0.1 z 0.8 WITH X-RAY AND OPTICALLY SELECTED SAMPLES. *The Astrophysical Journal* 756(2), 139.

Conselice, C. J. (2003). The Relationship between Stellar Light Distributions of Galaxies and Their Formation Histories. *ApJ Supp.* 147(1), 1–28.

Conselice, C. J., Bershady, M. A., and Jangren, A. (2000). The Asymmetry of Galaxies: Physical Morphology for Nearby and High-Redshift Galaxies. *ApJ* 529(2), 886–910.

Conselice, C. J. et al. (2016). THE EVOLUTION OF GALAXY NUMBER DENSITY AT z < 8 AND ITS IMPLICATIONS. *The Astrophysical Journal* 830(2), 83.

Cortese, L. et al. (2006). Witnessing galaxy preprocessing in the local Universe: the case of a star-bursting group falling into Abell 1367. *Astron. & Astrophys.* 453(3), 847–861.

Cortijo-Ferrero, C. et al. (2017). The spatially resolved star formation history of mergers. A comparative study of the LIRGs IC 1623, NGC 6090, NGC 2623, and Mice. *Astron. & Astrophys.* 607 A70, A70.

de Vaucouleurs, G. (1959). Classification and Morphology of External Galaxies. *Handbuch der Physik* 53, 275.

Dekel, A. and Burkert, A. (2014). Wet disc contraction to galactic blue nuggets and quenching to red nuggets. *MNRAS* 438(2), 1870–1879.

Demers, M. L., Parker, L. C., and Roberts, I. D. (2019). Smaller stellar disc scale lengths in rich environments. *MNRAS* 489(2), 2216–2226.

Dermer, C. D. and Giebels, B. (2016). Active galactic nuclei at gamma-ray energies. *Comptes Rendus Physique* 17(6), 594–616.

Disney, M. J., McNally, D., and Wright, A. E. (1969). The collapse of interstellar gas clouds-IV. Models of collapse and a theory of star formation. *MNRAS* 146, 123.

Dressler, A. (1980). Galaxy morphology in rich clusters: implications for the formation and evolution of galaxies. *ApJ* 236, 351–365.

Drory, N. et al. (2015). The MaNGA Integral Field Unit Fiber Feed System for the Sloan 2.5 m Telescope. *Astronomical Journal* 149(2) 77, 77.

Eales, S., Eales, O., and de Vis, P. (2020). Do bulges stop stars forming? *MNRAS* 491(1), 69–79.

Einasto, J. et al. (1974). Missing mass around galaxies - Morphological evidence. *Nature* 252, 111–113.

Einstein, A. (1936). LENS-LIKE ACTION OF A STAR BY THE DEVIATION OF LIGHT IN THE GRAVITATIONAL FIELD. *Science* 84(2188), 506–507. ISSN: 0036-8075.

Eke, V. R. et al. (2004). Galaxy groups in the 2dFGRS: the group-finding algorithm and the 2PIGG catalogue. *MNRAS* 348(3), 866–878.

Ellison, S. L. et al. (2016). The star formation rates of active galactic nuclei host galaxies. *Monthly Notices of the Royal Astronomical Society: Letters* 458(1), L34–L38. ISSN: 1745-3925.

Falcón-Barroso, J. et al. (2011). An updated MILES stellar library and stellar population models. *Astron. & Astrophys.* 532 A95, A95.

Fang, J. J. et al. (2013). A Link between Star Formation Quenching and Inner Stellar Mass Density in Sloan Digital Sky Survey Central Galaxies. *ApJ* 776(1) 63, 63.

Ferrari, A. (1998). Modeling Extragalactic Jets. *Ann. Rev. of Astron. & Astrophys.* 36, 539–598.

Feulner, G. et al. (2005). The connection between star formation and stellar mass: specific star formation rates to redshift one. *Monthly Notices of the Royal Astronomical Society: Letters* 358(1), L1–L5. ISSN: 1745-3925.

Finn, R. A. et al. (2018). The Local Cluster Survey. I. Evidence of Outside-in Quenching in Dense Environments. *ApJ* 862(2) 149, 149.

Fukugita, M. et al. (1996). The Sloan Digital Sky Survey Photometric System. *Astronomical Journal* 111, 1748.

Gallagher, J. S. and Hunter, D. A. (1984). Structure and Evolution of Irregular Galaxies. *Annual Review of Astronomy and Astrophysics* 22(1), 37–74.

Gallazzi, A. et al. (2005). The ages and metallicities of galaxies in the local universe. *Monthly Notices of the Royal Astronomical Society* 362(1), 41–58. ISSN: 0035-8711.

Garnett, D. R. (2002). The Luminosity-Metallicity Relation, Effective Yields, and Metal Loss in Spiral and Irregular Galaxies. *ApJ* 581(2), 1019–1031.

Geha, M. et al. (2012). A Stellar Mass Threshold for Quenching of Field Galaxies. *ApJ* 757(1) 85, 85.

George, M. R. et al. (2013). GALAXIES IN X-RAY GROUPS. III. SATELLITE COLOR AND MORPHOLOGY TRANSFORMATIONS. *The Astrophysical Journal* 770(2), 113.

Giavalisco, M. (2002). Lyman-Break Galaxies. *Ann. Rev. of Astron. & Astrophys.* 40, 579–641.

Gill, S. P. D., Knebe, A., and Gibson, B. K. (2005). The evolution of substructure - III. The outskirts of clusters. *MNRAS* 356(4), 1327–1332.

Gingerich, O. (1953). Messier and His Catalogue II. *Sky and Telescope* 12, 288.

Glazebrook, K. et al. (1999). Measurement of the star formation rate from Hα in field galaxies at z=1. *Monthly Notices of the Royal Astronomical Society* 306(4), 843–856. ISSN: 0035-8711.

Greenstein, J. L. and Schmidt, M. (1964). The Quasi-Stellar Radio Sources 3C 48 and 3C 273. *ApJ* 140, 1.

Gunn, J. E., Hoessel, J. G., and Oke, J. B. (1986). A Systematic Survey for Distant Galaxy Clusters. *ApJ* 306, 30.

Gunn, J. E. and Gott J. Richard, I. (1972). On the Infall of Matter Into Clusters of Galaxies and Some Effects on Their Evolution. *ApJ* 176, 1.

Hafez, I., Stephenson, F. R., and Orchiston, W. (2011). Al-Sufi's Investigation of Stars, Star Clusters and Nebulae. In: *American Astronomical Society Meeting Abstracts #217*. Vol. 217. American Astronomical Society Meeting Abstracts, 146.01.

Hani, M. H. et al. (2020). Variations in the slope of the resolved star-forming main sequence: a tool for constraining the mass of star-forming regions. *MNRAS* 493(1), L87–L91.

Hogan, B. S. et al. (2011). Chandra Discovery of 10 New X-ray Jets Associated with FR II Radio Core-selected AGNs in the MOJAVE Sample. *ApJ* 730(2) 92, 92.

Hubble, E. (1936). *The Realm of the Nebulae*. Yale University.

Hubble, E. P. (1925). Cepheids in spiral nebulae. *The Observatory* 48, 139–142.

Hubble, E. P. (1926). Extragalactic nebulae. *ApJ* 64, 321–369.

Hubble, E. P. (1927). The classification of spiral nebulae. *The Observatory* 50, 276.

Hubble, E. (1929). A Relation between Distance and Radial Velocity among Extra-Galactic Nebulae. *Proceedings of the National Academy of Science* 15(3), 168–173.

Hwang, J.-S., Park, C., and Choi, J.-H. (2012). The initial conditions and evolution of isolated galaxy models: Effects of the hot gas halo. *Journal of Korean Astronomical Society* 46.

Jennison, R. and Gupta, M. D. (1953). Fine Structure of the Extra-terrestrial Radio Source Cygnus I. *Nature* 172, 996–997.

Kafle, P. R. et al. (2016). Galaxy And Mass Assembly (GAMA): the absence of stellar mass segregation in galaxy groups and consistent predictions from GALFORM and EAGLE simulations. *MNRAS* 463(4), 4194–4209.

Kauffmann, G. et al. (2003). The host galaxies of active galactic nuclei. *MNRAS* 346(4), 1055–1077.

Kennicutt R. C., J. and Kent, S. M. (1983). A survey of H-alpha emission in normal galaxies. *Astronomical Journal* 88, 1094–1107.

Kennicutt Robert C., J. (1998a). Star Formation in Galaxies Along the Hubble Sequence. *Ann. Rev. of Astron. & Astrophys.* 36, 189–232.

Kennicutt Robert C., J. (1998b). The Global Schmidt Law in Star-forming Galaxies. *ApJ* 498(2), 541–552.

Kennicutt, R. C. and Evans, N. J. (2012). Star Formation in the Milky Way and Nearby Galaxies. *Ann. Rev. of Astron. & Astrophys.* 50, 531–608.

Kereš, D. et al. (2005). How do galaxies get their gas? *MNRAS* 363(1), 2–28.

Kewley, L. J. et al. (2006). The host galaxies and classification of active galactic nuclei. *MNRAS* 372(3), 961–976.

Kim, S. S. and Lee, M. G. (2007). Reddening Behaviors of Galaxies in the SDSS Photometric System. *Publications of the Astronomical Society of the Pacific* 119(862), 1449–1461.

Koratkar, A. and Blaes, O. (1999). Invited Review: The Ultraviolet and Optical Continuum Emission in Active Galactic Nuclei: The Status of Accretion Disks. *Publications of the Astronomical Society of the Pacific* 111(755), 1–30.

Kormendy, J. et al. (2009). Structure and Formation of Elliptical and Spheroidal Galaxies. *ApJ Supp.* 182(1), 216–309.

Lake, G. and Moore, B. (1999). Galaxy Harassment-Interactions for the 90s. In: *Galaxy Interactions at Low and High Redshift*. Ed. by J. E. Barnes and D. B. Sanders. Vol. 186. IAU Symposium, 393.

Larson, R. B., Tinsley, B. M., and Caldwell, C. N. (1980). The evolution of disk galaxies and the origin of S0 galaxies. *ApJ* 237, 692–707.

Larson, R. B. (1972). Infall of Matter in Galaxies. *Nature* 236(5340), 21–23.

Law, D. R. et al. (2015). Observing Strategy for the SDSS-IV/MaNGA IFU Galaxy Survey. *Astronomical Journal* 150(1) 19, 19.

Law, D. R. et al. (2016a). THE DATA REDUCTION PIPELINE FOR THE SDSS-IV MaNGA IFU GALAXY SURVEY. *The Astronomical Journal* 152(4), 83.

Law, D. R. et al. (2016b). The Data Reduction Pipeline for the SDSS-IV MaNGA IFU Galaxy Survey. *Astronomical Journal* 152(4) 83, 83.

Leavitt, H. S. (1908). 1777 variables in the Magellanic Clouds. *Annals of Harvard College Observatory* 60, 87–108.3.

Lee, B. et al. (2017). The effect of ram pressure on the molecular gas of galaxies: three case studies in the Virgo cluster. *MNRAS* 466(2), 1382–1398.

Lequeux, J. et al. (1979). Reprint of 1979A&A....80..155L. Chemical composition and evolution of irregular and blue compact galaxies. *Astron. & Astrophys.* 500, 145–156.

Leslie, S. K. et al. (2015). Quenching star formation: insights from the local main sequence. *Monthly Notices of the Royal Astronomical Society: Letters* 455(1), L82–L86. ISSN: 1745-3925.

Lian, J. et al. (2019). SDSS-IV MaNGA: environmental dependence of gas metallicity gradients in local star-forming galaxies. *MNRAS* 489(1), 1436–1450.

Lim, S. H. et al. (2017). Galaxy groups in the low-redshift Universe. *MNRAS* 470(3), 2982–3005.

Lin, L. et al. (2019). SDSS-IV MaNGA: Inside-out versus Outside-in Quenching of Galaxies in Different Local Environments. *The Astrophysical Journal* 872(1), 50.

Linden, A. von der et al. (2010). Star formation and AGN activity in SDSS cluster galaxies. *Monthly Notices of the Royal Astronomical Society* 404(3), 1231–1246. ISSN: 0035-8711.

Lu, Y. et al. (2016). GALAXY GROUPS IN THE 2MASS REDSHIFT SURVEY. *The Astrophysical Journal* 832(1), 39.

Lynden-Bell, D. (1969). Galactic Nuclei as Collapsed Old Quasars. *Nature* 223(5207), 690–694.

Madau, P. and Dickinson, M. (2014). Cosmic Star-Formation History. *Ann. Rev. of Astron. & Astrophys.* 52, 415–486.

Mahajan, S., Mamon, G. A., and Raychaudhury, S. (2011). The velocity modulation of galaxy properties in and near clusters: quantifying the decrease in star formation in backsplash galaxies. *MNRAS* 416(4), 2882–2902.

Márquez, I. and Moles, M. (1999). Effects of interaction on the properties of spiral galaxies. II. Isolated galaxies: The zero point. *Astron. & Astrophys.* 344, 421–432.

Martig, M. et al. (2009). Morphological Quenching of Star Formation: Making Early-Type Galaxies Red. *ApJ* 707(1), 250–267.

Martínez, H. J. et al. (2002). Galaxy groups in the 2dF Galaxy Redshift Survey: effects of environment on star formation. *Monthly Notices of the Royal Astronomical Society* 333(2), L31–L34. ISSN: 0035-8711.

Martins, L. P. et al. (2005). A high-resolution stellar library for evolutionary population synthesis. *Monthly Notices of the Royal Astronomical Society* 358(1), 49–65. ISSN: 0035-8711.

Masters, K. L. et al. (2011). Galaxy Zoo: bars in disc galaxies. *Monthly Notices of the Royal Astronomical Society* 411(3), 2026–2034. ISSN: 0035-8711.

Matthee, J. and Schaye, J. (2019). The origin of scatter in the star formation rate-stellar mass relation. *MNRAS* 484(1), 915–932.

Mayer, L., Governato, F., and Kaufmann, T. (2008). The formation of disk galaxies in computer simulations. *Advanced Science Letters* 1, 7–27.

McCray, R. (1979). Spherical accretion onto supermassive black holes. In: *Active Galactic Nuclei*. Ed. by C. Hazard and S. Mitton, 227–239.

McKee, C. F. and Ostriker, J. P. (1977). A theory of the interstellar medium: three components regulated by supernova explosions in an inhomogeneous substrate. *ApJ* 218, 148–169.

Medling, A. M. et al. (2018). The SAMI Galaxy Survey: spatially resolving the main sequence of star formation. *Monthly Notices of the Royal Astronomical Society* 475(4), 5194–5214. ISSN: 0035-8711.

Menéndez-Delmestre, K. et al. (2007). A Near-Infrared Study of 2MASS Bars in Local Galaxies: An Anchor for High-Redshift Studies. *ApJ* 657(2), 790–804.

Merritt, D. (1983). Relaxation and tidal stripping in rich clusters of galaxies. I. Evolution of the mass distribution. *ApJ* 264, 24–48.

Messier, C. (1774). Catalogue des Nébuleuses & des amas d'Étoiles, que l'on découvre parmi les Étoiles fixes sur l'horizon de Paris; observées à l'Observatoire de la Marine, avec differens instruments. *Mémoires de l'Académie Royale des Sciences* VIII(P1), 435–461.

Mitchell, R. J. et al. (1976). Ariel 5 observations of the X-ray spectrum of the Perseus cluster. *MNRAS* 175, 29P–34P.

Moore, B., Lake, G., and Katz, N. (1998). Morphological Transformation from Galaxy Harassment. *ApJ* 495(1), 139–151.

Moore, B. et al. (1996). Galaxy harassment and the evolution of clusters of galaxies. *Nature* 379(6566), 613–616.

Moorthy, B. K. and Holtzman, J. A. (2006). Stellar populations in bulges of spiral galaxies. *MNRAS* 371(2), 583–608.

Moustakas, J., Kennicutt Robert C., J., and Tremonti, C. A. (2006). Optical Star Formation Rate Indicators. *ApJ* 642(2), 775–796.

Moustakas, J. et al. (2013). PRIMUS: Constraints on Star Formation Quenching and Galaxy Merging, and the Evolution of the Stellar Mass Function from z = 0-1. *ApJ* 767(1) 50, 50.

NASA et al. (2008). *Montage of some well known interacting galaxies.*

Nidever, D. L. et al. (2012). THE APACHE POINT OBSERVATORY GALACTIC EVOLUTION EXPERIMENT: FIRST DETECTION OF HIGH-VELOCITY MILKY WAY BAR STARS. *The Astrophysical Journal* 755(2), L25.

Oman, K. A., Hudson, M. J., and Behroozi, P. S. (2013). Disentangling satellite galaxy populations using orbit tracking in simulations. *MNRAS* 431(3), 2307–2316.

Oosterloo, T. and van Gorkom, J. (2005). A large H I cloud near the centre of the Virgo cluster. *Astron. & Astrophys.* 437(1), L19–L22.

Page, M. J. et al. (2012). The suppression of star formation by powerful active galactic nuclei. *Nature* 485(7397), 213–216.

Pasquali, A. et al. (2009). The rise and fall of galaxy activity in dark matter haloes. *Monthly Notices of the Royal Astronomical Society* 394(1), 38–50. ISSN: 0035-8711.

Peters W. L., I. (1975). Models for the inner regions of the Galaxy. I. *The Astrophysical Journal* 195, 617–629.

Petrosian, V. (1976). Surface Brightness and Evolution of Galaxies. *ApJL* 210, L53.

Pontzen, A. et al. (2016). How to quench a galaxy. *Monthly Notices of the Royal Astronomical Society* 465(1), 547–558. ISSN: 0035-8711.

Popesso, P. et al. (2019). The main sequence of star-forming galaxies - I. The local relation and its bending. *MNRAS* 483(3), 3213–3226.

Postman, M. et al. (2012). THE CLUSTER LENSING AND SUPERNOVA SURVEY WITH HUBBLE: AN OVERVIEW. *The Astrophysical Journal Supplement Series* 199(2), 25.

Quilis, V., Moore, B., and Bower, R. (2000). Gone with the Wind: The Origin of S0 Galaxies in Clusters. *Science* 288(5471), 1617–1620. ISSN: 0036-8075.

Ribas, I. et al. (2005). First Determination of the Distance and Fundamental Properties of an Eclipsing Binary in the Andromeda Galaxy. *The Astrophysical Journal* 635(1), L37–L40.

Roberts, I. D. et al. (2014). Mass-segregation trends in SDSS galaxy groups. *Monthly Notices of the Royal Astronomical Society: Letters* 448(1), L1–L5. ISSN: 1745-3925.

Rubin, V. C. and Ford W. Kent, J. (1970). Rotation of the Andromeda Nebula from a Spectroscopic Survey of Emission Regions. *ApJ* 159, 379.

Salim, S., Boquien, M., and Lee, J. C. (2018). Dust Attenuation Curves in the Local Universe: Demographics and New Laws for Star-forming Galaxies and High-redshift Analogs. *ApJ* 859(1) 11, 11.

Salim, S. et al. (2007). UV Star Formation Rates in the Local Universe. *ApJ Supp.* 173(2), 267–292.

Sánchez-Blázquez, P. et al. (2006). Medium-resolution Isaac Newton Telescope library of empirical spectra. *MNRAS* 371(2), 703–718.

Sánchez, S. F. et al. (2016a). Pipe3D, a pipeline to analyze Integral Field Spectroscopy Data: I. New fitting philosophy of FIT3D. *Revista Mexicana de Astronomia y Astrofisica* 52, 21–53.

Sánchez, S. F. et al. (2016b). Pipe3D, a pipeline to analyze Integral Field Spectroscopy Data: II. Analysis sequence and CALIFA dataproducts. *Revista Mexicana de Astronomia y Astrofisica* 52, 171–220.

Sancisi, R. et al. (2008). Cold gas accretion in galaxies. *Astron. & Astrophys. Rev.* 15(3), 189–223.

Schaefer, A. L. et al. (2016). The SAMI Galaxy Survey: spatially resolving the environmental quenching of star formation in GAMA galaxies. *Monthly Notices of the Royal Astronomical Society* 464(1), 121–142. ISSN: 0035-8711.

Schaefer, A. L. et al. (2019). The SAMI Galaxy Survey: observing the environmental quenching of star formation in GAMA groups. *MNRAS* 483(3), 2851–2870.

Schawinski, K. et al. (2006). Suppression of star formation in early-type galaxies by feedback from supermassive black holes. *Nature* 442(7105), 888–891.

Schawinski, K. et al. (2007). Observational evidence for AGN feedback in early-type galaxies. *MNRAS* 382(4), 1415–1431.

Schawinski, K. et al. (2014). The green valley is a red herring: Galaxy Zoo reveals two evolutionary pathways towards quenching of star formation in early- and late-type galaxies. *MNRAS* 440(1), 889–907.

Schaye, J. et al. (2015). The EAGLE project: simulating the evolution and assembly of galaxies and their environments. *MNRAS* 446(1), 521–554.

Schmidt, M. (1963). 3C 273 : A Star-Like Object with Large Red-Shift. *Nature* 197(4872), 1040.

Secchi, A. (1866). Nouvelles recherches sur l'analyse spectrale de la lumière des étoiles. *Comptes Rendus des Séances de l'Académie des Sciences* 63, 621–628.

Serlemitsos, P. J. et al. (1977). X-radiation from clusters of galaxies: spectral evidence for a hot evolved gas. *ApJL* 211, L63–L66.

Seyfert, C. K. (1943). Nuclear Emission in Spiral Nebulae. *ApJ* 97, 28.

Shakura, N. I. and Sunyaev, R. A. (1973). Reprint of 1973A&A....24..337S. Black holes in binary systems. Observational appearance. *Astron. & Astrophys.* 500, 33–51.

Shimizu, T. T. et al. (2015). Decreased specific star formation rates in AGN host galaxies. *Monthly Notices of the Royal Astronomical Society* 452(2), 1841–1860. ISSN: 0035-8711.

Sijacki, D. et al. (2007). A unified model for AGN feedback in cosmological simulations of structure formation. *MNRAS* 380(3), 877–900.

Silverman, J. D. et al. (2009). Ongoing and Co-Evolving Star Formation in zCOSMOS Galaxies Hosting Active Galactic Nuclei. *ApJ* 696(1), 396–410.

Simard, L. (1998). GIM2D: an IRAF package for the Quantitative Morphology Analysis of Distant Galaxies. In: *Astronomical Data Analysis Software and Systems VII*. Ed. by R. Albrecht, R. N. Hook, and H. A. Bushouse. Vol. 145. Astronomical Society of the Pacific Conference Series, 108.

Singh, A., Gulati, M., and Bagla, J. S. (2019). Ram pressure stripping: an analytical approach. *MNRAS* 489(4), 5582–5593.

Sivanandam, S. et al. (2018). Gemini infrared multi-object spectrograph: instrument overview. In: *Ground-based and Airborne Instrumentation for Astronomy VII*. Vol. 10702. Society of Photo-Optical Instrumentation Engineers (SPIE) Conference Series, 107021J.

Smee, S. A. et al. (2013). The Multi-object, Fiber-fed Spectrographs for the Sloan Digital Sky Survey and the Baryon Oscillation Spectroscopic Survey. *Astronomical Journal* 146(2) 32, 32.

Spindler, A. et al. (2018). SDSS-IV MaNGA: the spatial distribution of star formation and its dependence on mass, structure, and environment. *MNRAS* 476(1), 580–600.

Springel, V., Di Matteo, T., and Hernquist, L. (2005). Modelling feedback from stars and black holes in galaxy mergers. *MNRAS* 361(3), 776–794.

Springob, C. M. et al. (2005). A Digital Archive of H I 21 Centimeter Line Spectra of Optically Targeted Galaxies. *ApJ Supp.* 160(1), 149–162.

Strateva, I. et al. (2001). Color Separation of Galaxy Types in the Sloan Digital Sky Survey Imaging Data. *The Astronomical Journal* 122(4), 1861–1874.

Tonnesen, S. and Bryan, G. L. (2009). GAS STRIPPING IN SIMULATED GALAXIES WITH A MULTIPHASE INTERSTELLAR MEDIUM. *The Astrophysical Journal* 694(2), 789–804.

Toomre, A. and Toomre, J. (1972). Galactic Bridges and Tails. *ApJ* 178, 623–666.

Tully, R. B. et al. (2014). The Laniakea supercluster of galaxies. *Nature* 513(7516), 71–73.

Uson, J. M., Boughn, S. P., and Kuhn, J. R. (1990). The Central Galaxy in Abell 2029: An Old Supergiant. *Science* 250(4980), 539–540. ISSN: 0036-8075.

van den Bergh, S. (1979). The origin of lenticular galaxies. *Journal of the Royal Astronomical Society of Canada* 73, 198–202.

Varela, J. et al. (2004). Properties of isolated disk galaxies. *Astron. & Astrophys.* 420, 873–879.

Vazdekis, A. et al. (2010). Evolutionary stellar population synthesis with MILES - I. The base models and a new line index system. *MNRAS* 404(4), 1639–1671.

Vollmer, B. (2009). A holistic view on ram pressure stripping in the Virgo cluster. The first complete model-based time sequence. *Astron. & Astrophys.* 502(2), 427–435.

Vulcani, B. et al. (2014). FROM BLUE STAR-FORMING TO RED PASSIVE: GALAXIES IN TRANSITION IN DIFFERENT ENVIRONMENTS. *The Astrophysical Journal* 798(1), 52.

Wake, D. A. et al. (2017). The SDSS-IV MaNGA Sample: Design, Optimization, and Usage Considerations. *The Astronomical Journal* 154(3), 86.

Wang, E. et al. (2018). SDSS-IV MaNGA: Star Formation Cessation in Low-redshift Galaxies. I. Dependence on Stellar Mass and Structural Properties. *The Astrophysical Journal* 856(2), 137.

Wechsler, R. H. and Tinker, J. L. (2018). The Connection Between Galaxies and Their Dark Matter Halos. *Annual Review of Astronomy and Astrophysics* 56(1), 435–487.

Wel, A. van der (2008). The Dependence of Galaxy Morphology and Structure on Environment and Stellar Mass. *The Astrophysical Journal* 675(1), L13–L16.

Westfall, K. B. et al. (2019). The Data Analysis Pipeline for the SDSS-IV MaNGA IFU Galaxy Survey: Overview. *Astronomical Journal* 158(6) 231, 231.

Wetzel, A. R. et al. (2013). Galaxy evolution in groups and clusters: satellite star formation histories and quenching time-scales in a hierarchical Universe. *MNRAS* 432(1), 336–358.

White, S. D. M. and Rees, M. J. (1978). Core condensation in heavy halos: a two-stage theory for galaxy formation and clustering. *MNRAS* 183, 341–358.

Williams, R., The Hubble Deep Field Team, and NASA (1996). *Hubble Deep Field.*

Xiao, T. et al. (2012). Dust reddening in star-forming galaxies. *Monthly Notices of the Royal Astronomical Society* 421(1), 486–501. ISSN: 0035-8711.

Yan, R. et al. (2016). SDSS-IV MaNGA IFS galaxy survey—survey design, execution, and initial data quality. *The Astronomical Journal* 152, 197.

Yang, X. et al. (2007). Galaxy Groups in the SDSS DR4. I. The Catalog and Basic Properties. *ApJ* 671(1), 153–170.

Yasuda, N. et al. (2001). Galaxy Number Counts from the Sloan Digital Sky Survey Commissioning Data. *The Astronomical Journal* 122(3), 1104–1124.

Young, J. and Scoville, N. (1991). Molecular gas in galaxies. *Ann. Rev. Astron. Astrophys.* 29, 581–625.

Zhai, X. et al. (2014). THREE-DIMENSIONAL MHD SIMULATION OF THE CALTECH PLASMA JET EXPERIMENT: FIRST RESULTS. *The Astrophysical Journal* 791(1), 40.

Zwicky, F. (1933). Die Rotverschiebung von extragalaktischen Nebeln. *Helvetica Physica Acta* 6, 110–127.

Zwicky, F. (1937). Nebulae as Gravitational Lenses. *Phys. Rev.* 51 (4), 290–290.